Investigations on states of ^{20}Mg and spallation reaction effects for constraining nuclear physics inputs for X-ray bursts

by

Jaspreet Singh Randhawa

A Thesis Submitted to
Saint Mary's University, Halifax, Nova Scotia
in Partial Fulfillment of the Requirements for
the Degree of Doctor of Philosophy in Astronomy
(Department of Astronomy and Physics)

2017, Halifax, Nova Scotia

Approved: Dr. Rituparna Kanungo
(Supervisor)

Approved: Dr. David Guenther
(Examiner)

Approved: Dr. Adam Sarty
(Examiner)

Approved: Dr. Ian Short
(Examiner)

Approved: Dr. Chris Wrede
(External Examiner)

Date: July 21, 2017.

Abstract

Investigations on states of ^{20}Mg and spallation reaction effects for constraining nuclear physics inputs for X-ray bursts

by

Jaspreet Singh Randhawa

We present the first observation of a resonance state in the proton drip-line nucleus ^{20}Mg. The resonance state was populated via inelastic scattering of ^{20}Mg with a solid deuteron target using the IRIS facility stationed at TRIUMF, Canada. Together with the ground state and first excited state, a new resonance state is observed at excitation energy of 3.68±0.04 MeV. Based on a comparison of the measured angular distributions to distorted wave Born approximation calculations, the first excited state is consistent with L=2 excitation confirming its spin to be 2^+. Similar comparison for new resonance suggests a spin possibility of either (4^+) or (2^+). The new resonance state lies in the Gamow window and hence puts constraint on the ^{18}Ne$(2p,\gamma)^{20}$Mg reaction rate, a possible breakout reaction from hot CNO cycles in X-ray bursts. The new resonance state is higher in energy than expectations based on mirror symmetry to ^{20}O. The inferred reaction rate of ^{19}Na(p,γ)^{20}Mg is lower than the previous predictions. The net rate of the ^{18}Ne$(2p,\gamma)^{20}$Mg is found to be competitive to beta decay of ^{18}Ne only at high densities for it to be a viable breakout path. A comparison to theoretical predictions show that the calculations based on chiral interactions and NN+3N forces fails to explain the observed resonance state. The new data will therefore serve as guidance to benchmark the nuclear structure models and interactions at the drip-line.

In a related study of CNO cycles in X-ray bursts, the spallation of the accreted material in the atmosphere of a neutron star has been modelled considering a full cascading destruction process. The results show that the replenishment of CNO elements in a cascading process is minuscule and the CNO abundances are reduced to negligible values. The impact of reduced CNO metallicity on X-ray burst ignition conditions are discussed.

(July 21, 2017)

Acknowledgements

First, big thanks to my thesis supervisor Prof. Rituparna Kanungo, for her mentorship, constant support throughout my Ph.D. work. Thank you for making me more and more pragmatic and providing enthusiasm to tackle challenges by leading from the front. You are a true leader. Sincere gratitude to my thesis committee members Prof. David Guenther, Prof. Adam Sarty and Prof. Ian Short for their support during my research. Many thanks to Prof. Hendrik Schatz and Prof. Bradley Meyer for fruitful discussions on modeling part. Next, big thanks to Dr. Martin Alcorta, as a friend and as a research group member. Your insight during each and every discussion is incredible. Thanks to all the people at TRIUMF especially Dr. Alisher Sanetulleav, Dr. Matthias Holl, Dr. Greg Hackman, Dr. Barry Davids and Dr. Chris Ruiz. To Prof. Alan Shotter for all the lively discussions. Thanks to Prof. Sandeep Sahijpal, Prof. Vishwa Mittar, Prof. Luigi Gallo, Prof. Kuljeet Marhas and Dr. Daniel Majaess for their support.

A huge thanks to my west coast friends especially Gurpreet Badesha for his hospitality and whole Badesha family, to Sukhwant Didi, Jinder Bhaaji, Navjot and Gurshabad. To Harjot Chahal, I cannot thank enough. You have been with me through thick and thin. Thanks for making me laugh. Thanks to Kuljinder Kaur Chahal and Avtar Kaur Chahal (Biji) for their blessings. To Harinder Chahal, Harman Sandhu, Sukhamrit Ghatoura, Deepinder Sidhu and Navi Sandhu, I enjoyed every bit of time with you. To Jasmeet Brar, Amit Madaan, Amit Kumar, Amit Davis, Gurinder Sahota, Abhinav Soni, Jasmeen Kang, Maan Hani, Jenn Beanlands and Maggie Sharma for their friendship. Childhood friends from Dhunda especially Baldev Randhawa, Rajbir Randhawa, Baljinder Randhawa, Harjeet Randhawa and Satnam Randhawa, thanks for believing in me. It was not possible without the blessings of my grandmother (Late) Mata Pritam Kaur ji. Thanks to my little friends throughout this journey, Jasleen, Arunpreet, Sahejpreet, Vishal, Navkaran and Nimrat. My friends Binny and Rooney, how can I forget you. Thanks to Bhau Kartar Singh (Tange-wala) and Gurnamo (Taayi) for their blessings. Thanks to all the residents of village Dhunda, you always live in my heart.

Contents

List of Figures

List of Tables

Dedicated to my parents S. Bhag Singh Randhawa, S. Balwinder Kaur Randhawa and to my sisters Sukhbir Kaur, Rajbir Kaur, Rajwinder Kaur and Kulwinder Kaur.

Chapter 1

Introduction

The visible matter in the Universe we see around us is all made up of atoms, and these atoms are further made up of tiny cores called the nucleus and electrons around it. The question about our place and existence in the Universe brings up a long-standing question, where does all this matter come from? How were these atoms synthesized and where? The Universe we see today is mostly made up of hydrogen and helium, with all the heavier elements making up only a tiny fraction of the Universe. In astronomy, all the elements heavier than helium are collectively called metals. The last century has seen a tremendous change in our understanding of the origin of these elements. As per our understanding today, hydrogen and helium (along with a tiny fraction of lithium) were synthesized within a few minutes after the Big Bang and rest of the elements were (are) synthesized at later times in stars (Burbidge et al.,1957, also commonly known as B^2FH). During the Big Bang, the temperature and density were decreasing at a fast rate, hence there was only a small time window during which fusion of elements was possible (Cyburt et al., 2016). The non-existence of stable elements with mass number five and eight was another hindrance in the formation of elements heavier than lithium. In 1920, Sir Authur Eddington proposed the fusion of hydrogen to helium as a source of energy in the Sun. This served as an early link between astronomy and nuclear physics, and

the investigation of nucleosynthesis in nature started flourishing. Later in the historical series of events related to understanding the production of elements in the Universe, Hans Bethe proposed the CNO cycles as processes to burn hydrogen to helium inside the stars. However, fusion inside the stars still faced a problem: a fusion of three alpha particles was hindered due to the unbound intermediate nucleus ^{8}Be. To explain the amount of ^{12}C present in our Universe, Fred Hoyle proposed the presence of an excited state in ^{12}C which is a resonance just above the $^{8}\mathrm{Be} + \alpha$ threshold of ^{12}C, and this would accelerate the triple alpha process. Later, this state was confirmed experimentally at 7.654 MeV (Cook et al.,1957). The same year, B^{2}FH (Burbidge et al., 1957) outlined the various sites of nucleosynthesis in the universe especially the sites and processes for production of the elements heavier than the nickel. Elements up to nickel can be produced by the fusion of the elements but beyond nickel binding energy per nucleon starts decreasing and the Coulomb barrier for fusion is very high. Therefore B^{2}FH explained the synthesis of heavier elements via two major processes, s-process and r-process. Here s in s-process stands for slow neutron capture and r in r-process stands for rapid neutron capture. The major advantage of the neutron capture process over the fusion process for heavy element production is that neutrons are charge neutral and do not the feel Coulomb repulsion. In s-process, as the neutron is captured by a particle, beta decay always has time to occur before another neutron capture. This forces the s-process to follow a path either through stable nuclei or close to beta stability valley. The s-process produces sharp peaks at mass number 88(Sr), 138(Ba) and 208(Pb). The s-process is thought to occur in Asymptotic Giant Branch stars and helium cores of massive stars (Kappeler et al., 2011). The two primary sources of neutrons in the s-process are the $^{13}\mathrm{C}(\alpha, n)^{16}\mathrm{O}$ and $^{22}\mathrm{Ne}(\alpha, n)^{25}\mathrm{Mg}$ reactions active at quite different temperatures. The r-process results from many successive neutron captures which drives the nucleosynthesis path to very neutron-rich nuclei. The prerequisite for r-process sites is the high availability of free neutrons. The exact site(s) of r-process is/are still unknown and is an active area of research. Among the possible sites discussed are neutron star mergers, neutrino driven

winds and jets from supernovae (Arnould et al., 2007).

However, neither the s-process nor the r-process can explain the existence of many proton-rich elements, called p-nuclei (Arnould & Goriely, 2003). The type-1 X-ray bursts have been proposed as the site for synthesis of some of these p-nuclei (especially light p-nuclei such as $^{92-94}$Mo and ^{96,98}Ru) via the rp-process (Schatz et al.(1998, 2001)). The rp-process is a phenomenon similar to the r-process but on the proton-rich side of the valley of beta stability, where rp stands for rapid proton capture. The hydrogen and helium-rich envelope accreted onto the neutron star surface in a close binary system leads to thermonuclear explosions known as type-I X-ray bursts (Lewin et al., 1993). These bursts are powered by a number of reaction sequences including the triple alpha process, hot CNO cycles, αp-process, and rp-process (Schatz & Rehm, 2006). The rp-process is crucial for the synthesis of lighter p-nuclei. Besides being a potential site for lighter p-nuclei, the theoretical models of X-ray bursts are of paramount importance to interpret the observations and to decipher the physics of the underlying neutron star. The reliable X-ray burst models are sensitive to various input parameters. Out of the various parameters, nuclear data (i.e. nuclear reaction rates, beta decay rates, masses) and the composition of accreted material are vital (Schatz & Rehm, 2006; Jose et al., 2010). For nuclear physics input, the study of reactions to bypass the so called waiting points are key to the nucleosynthesis as well as burst energetics. Therefore, it is crucial to experimentally constrain the nuclear physics at key waiting points. The other vital input parameter is the composition of accreted material, especially the CNO abundances (Woosley et al., 2004; Jose et al., 2010). The CNO abundance dictates the burning rate of hydrogen to helium via hot CNO cycles. It determines for a given mass accretion rate, whether hydrogen will be present while helium ignition takes place or not, hence dictating whether the H & He mixed flashes or pure He flashes occur (Cumming & Bildsten, 2000). These ignition models will be discussed further in the last section of chapter 2. Therefore, by constraining the key nuclear physics at waiting points and composition of accreted material one can significantly constrain the X-ray burst light

curves and final composition of burst ashes.

1.1 Focus of the dissertation

The focus of this thesis is to constrain some of the above-discussed nuclear physics information for X-ray bursts, both via experiment as well as theoretically. The experimental part, which is the major focus of this thesis, aims at constraining the ^{18}Ne(2p,γ)^{20}Mg reaction rate, a possible breakout reaction to bypass a crucial waiting point nucleus ^{18}Ne during X-ray bursts (Görres et al., 1995). To constrain this reaction rate we have investigated the resonances in ^{20}Mg through ^{20}Mg(d,d')^{20}Mg inelastic scattering reaction using the IRIS facility at TRIUMF, Canada. In addition, theoretical model estimates were undertaken to examine the impact of spallation reactions in the atmospheres of accreting neutron stars on the composition of the accreted material. The details of the scientific motivation behind both the experimental and modelling parts will be discussed in Chapter 2.

The rest of this chapter explains the various aspects of X-ray bursts and related nuclear physics processes. The next section explains the journey of the accreted material as it is processed through various nuclear processes and the observational signatures of surface nuclear burning and deeper burning are also explained. Section 1.3 focuses on the type-I X-ray bursts alone and key nuclear physics inputs for these bursts. The general formalism to evaluate the reactions rates as well as the experimental determination of these rates is also outlined in the same section. Towards the end of this chapter, Section 1.4 outlines the content of subsequent chapters.

1.2 Astrophysics and nuclear physics relation of X-ray bursts and neutron star

Most of the stars we see in our universe comes in pairs. These stars are called binary systems and one particular type of binary stars are X-ray binaries. X-ray binaries (which undergo X-ray bursts) are among the brightest objects in the sky ($L > 10^{34}$ erg/s) outside our solar system. These objects also show most frequent explosions in nature and show variations in the brightness, with timescales ranging from milliseconds to years (Lewin et al., 1993). In X-ray binaries, one of the stars is a neutron star (a compact remnant of a massive star). The neutron star accretes material from its companion through Roche-lobe overflow. Depending upon the mass of the companion (or donor) these X-ray binaries are divided into two classes, Low Mass X-ray Binaries (LMXB, with donor mass $< 10M_{\odot}$) and High Mass X-ray Binaries (HMXB, with donor mass $> 10M_{\odot}$). Their primary source of power is the gravitational energy released by the infalling material from the companion star. Observationally, X-ray bursts are broadly classified into two broad categories, type-I X-ray bursts (which are mostly low mass LMXBs) which are thermonuclear flashes on the surface of the neutron star, and type-II X-ray bursts which are rapid bursters mainly due to accretion disk instabilities (Lewin et al.,1993). Here, the focus is on type-I X-ray bursts. These bursts are predominantly powered by the nuclear burning on the surface of an accreting neutron star. The accreted material continues its journey downward into the neutron star interior and undergoes a sequence of nuclear processes. The ashes of one nuclear process sets the stage for the next nuclear process and hence all the events, one following another, are interconnected. Section 1.2.1 discusses the nuclear processes at different depths in the neutron stars.

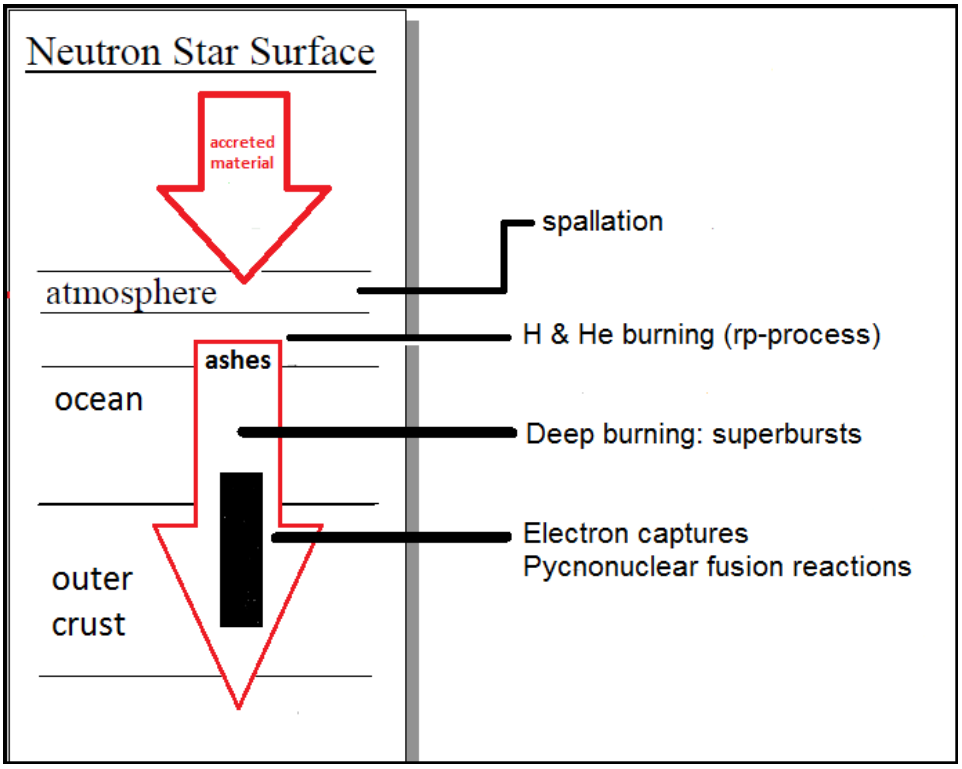

FIGURE 1.1: Journey of accreted fluid elements. Various nuclear processes take place at different density and temperature regimes.

1.2.1 Journey of the accreted material

As mentioned earlier, the fluid element of accreted material onto the surface of a neutron star are continuously compressed by the freshly accreted material from above. The surface nuclear burning via αp reactions and the rp-process gives rise to type-I X-ray bursts. The ashes of the surface nuclear burning sink deeper and decisively affect the nuclear process in the deeper layers. The journey of the accreted fluid element through various layers of neutron star is shown in Figure 1.1 where the nuclear processes during this journey are explained in four different steps.

- **Spallation in the atmospheres**

The journey of accreted elements first starts through the neutron star atmospheres. The accreted material could be stopped by Coulomb collisions with atmospheric electrons (Bildsten et al., 1992). As these collisions are dependent on the atomic number (Z) and mass number (A), the elements heavier than hydrogen and helium thermalize at higher altitudes in the neutron star atmospheres. As the heavier elements stop at shallower depths, their downward journey is then dictated by the diffusion process. However, the incoming protons still have high energy at those altitudes and can destroy these heavier elements through the nuclear spallation reactions. Therefore this spallation process in the neutron star atmospheres can significantly change the accreted composition before it settles down to deeper layers of the neutron star where X-ray bursts are triggered. In a previous study, destruction of only CNO elements through spallation has been studied (Bildsten et al.,1992). The full cascading destruction process was not considered due to lack of knowledge of spallation cross sections at that time. In a cascading destruction process, CNO elements could be replenished due to the destruction of relatively heavy elements. One part of this thesis has been dedicated to studying the change in accreted composition via spallation reactions considering a full cascading destruction process, and its impact on burst ignition conditions. Further details are discussed in the last section of Chapter 2 and in Chapter 6.

- **Hot CNO burning and rp-process**

  The accreted material, spallated or not, is continuously being pushed to the deeper layers of the neutron star. The mass fraction of CNO elements decides the fate of hydrogen through hot CNO burning. The burst is not triggered until the conditions are not conducive for the triple alpha process. Depending on the availability of hydrogen when helium ignites, the system could lead to pure helium flashes or

mixed (H & He) flashes (Cumming & Bildsten, 2000). As the triple alpha process starts, since it is extremely temperature sensitive, it leads to thin shell instability (Schatz and Rehm, 2006 and ref within) where nuclear energy generation rate is more than the cooling rate:

$$\frac{\mathrm{d}\epsilon_{nuc}}{\mathrm{d}T} > \frac{\mathrm{d}\epsilon_{cool}}{\mathrm{d}T} \tag{1.1}$$

This means that the nuclear energy generation can neither be compensated by the structural adjustment (due to the presence of degenerate electron gas) nor by the surface cooling. This leads to a thermonuclear runaway- that is, more rate of nuclear reactions leading to higher temperature, hence further increase of the burning rate. This thermonuclear energy release ($> 10^{38}$ ergs) can be observed as type-I X-ray bursts. The typical period for these bursts is from few seconds to few hundred seconds. The recurrence times for these bursts are from hours to days. These short timescales make these objects observationally suitable candidates for studying the underlying physics and neutron star properties (Ozel et al., 2016; Zamfir et al., 2012) as long sequences of the burst can be observed. Figure 1.2 shows the light curves for a sequence of X-ray bursts. These bursts are simulated using one zone X-ray burst code by A. Cumming (Heger et al., 2007) for accretion rate $0.5\dot{m}_{Edd}$. In the nuclear burning during X-ray bursts, the hydrogen is burned mainly via the rp-process. The detailed reaction pathways during X-ray bursts and waiting points will be discussed in Section 1.3.1. The rp-process burning leads to the synthesis of heavy proton-rich elements. The overall energy generated during the rp-process is around 7 MeV per nucleon (or 7 MeV/u). This energy is small compared to the gravitational energy released by infalling material. The gravitational energy release can be written as

$$E_{grav} = \frac{G \times M \times m_u}{R} \tag{1.2}$$

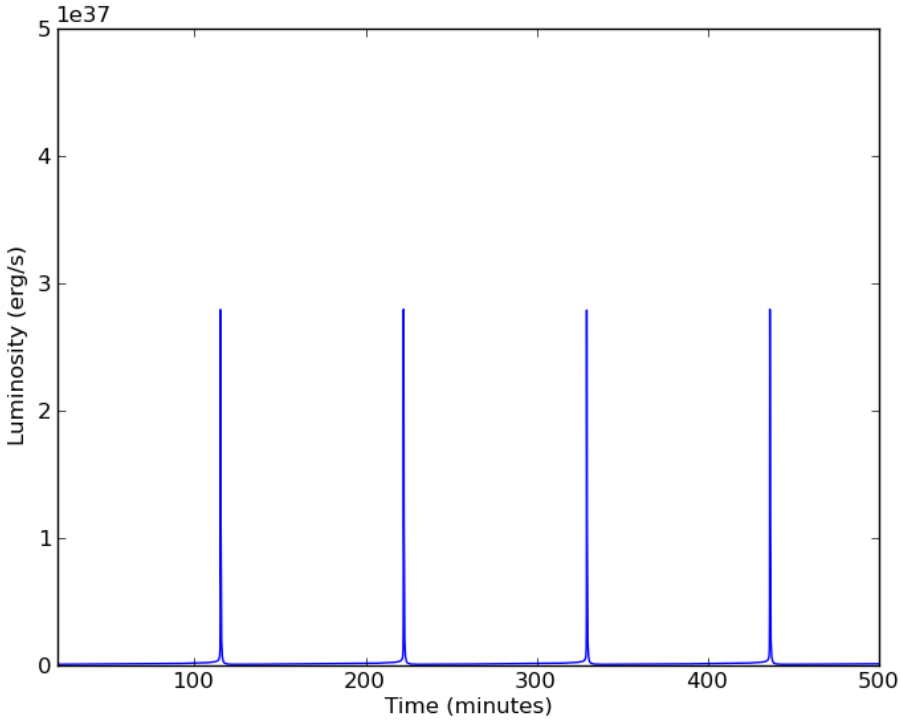

FIGURE 1.2: Simulated thermonuclear flashes using onezone (open source) code by A. Cumming (Heger et al.,2007)). The observed light curves have been seen to be both periodic and non periodic (Boirin et al., 2007).

Here G is the gravitational constant, M and R are mass and radius of a neutron star, and m_u is the mass of accreted element, respectively. For typical neutron star mass and radius $E_{grav} \approx 200$ MeV/u. However, due to unstable, explosive burning during the burst, the whole energy is released in a small interval of time and is observed as type-I X-ray bursts on the top of the persistent flux due to gravitational energy. As the energy available per nucleon from the burst is around 7 MeV, this energy is not sufficient to overcome the gravitational potential of the neutron star and hence the ashes cannot be ejected out. This means that X-ray burst ashes may never become the part of the interstellar medium. But this issue is still under debate as certain burst like PRE-bursts (Photospheric Radial Expansion bursts) have been proposed to eject the rp-process nucleosynthesis products into

the interstellar medium (in't Zand et al., 2014). For most of the cases, the burst ashes sink further deeper into the neutron star interior. The following two steps explain the further nuclear processes these ashes go through as they traverse further into the higher density regimes.

- **Carbon burning and superbursts**

  BeppoSAX and Rossi X-ray Timing explorers detected many large type-I X-ray bursts known as superbursts (Kuulkers et al., 2002). Superbursts are 1000 times more energetic and 1000 times longer in duration than typical type-I X-ray bursts (Schatz et al, 2003). The unstable carbon ignition in the deeper layers of the ocean of heavier elements has been proposed as the possible source of such bursts (Cumming & Bildsten, 2001). As the ashes of rp-process burning sink downwards, if enough carbon is present along with heavier elements from the ashes then the highly temperature sensitive carbon ignition sets in and this leads to superbursts. The burning of a pure carbon layer has been ruled out as the source of superbursts because a very high mass of carbon ($\approx 10^{27}g$) is required. The heavy elements play an important role in the thermal conductivity. For thermonuclear runaway, the nuclear energy generation rate has to win over the conductive cooling rate (see Equation 1.1). The heat transportation in the ocean of heavy ions is dominated by the electron conduction due to electron-ion scattering. The thermal conductivity can be written as (Cumming & Bildsten 2001)

$$K = 1.1 \times 10^{18} \frac{\rho_8^{1/3} T_8}{Z^{2/3} A^{1/3}} (ergscm^{-1}s^{-}K^{-1}) \tag{1.3}$$

  Here ρ_8 is the density in $10^8 gm/cm^3$, T_8 is the temperature in $10^8 K$, Z and A are the atomic number and atomic masses of the most abundant nucleus in the heavy ion ocean. This equation shows that for heavier elements (high Z and A) the thermal conductivity is small and hence less conductive cooling. This condition leads to thermonuclear runaway at lower column depths and ^{12}C burning as

a plausible source of superbursts. However, different models of rp-process nucleosynthesis show that not enough carbon required for superbursts ($X_C > 0.1$) is produced during type-1 X-ray bursts (Stevens et al., 2014). Thus, the source of required carbon and hence superbursts is still an active area of research.

- **Electron capture and pycnonuclear reactions**

  The processed material continues it's journey downwards and forms a rigid lattice known as the crust (Horowitz et al., 2009). At these higher densities, the nuclei are surrounded by the strongly degenerate electron gas. The rp-process ashes are proton-rich so that they could undergo beta decay. The β^+-decay i.e.

$$(Z, A) \rightarrow (Z - 1, A) + e^+ + \nu_e \tag{1.4}$$

  and electron capture i.e.

$$e^- + (Z, A) \rightarrow (Z - 1, A) + \nu_e \tag{1.5}$$

  are both operational to shift proton-rich nuclei to the neutron-rich nuclei. As nuclei move from proton-rich towards stable nuclei and with increasing depth, these ashes are transformed by capture of degenerate electrons into increasingly neutron-rich nuclei. The energy generated during this process is either taken away by the neutrinos or deposited in the crust. The neutron-rich material settles down to form the rigid lattice. The zero-point vibrations of these nuclei in the lattice helps them to overcome the Coulomb barrier and hence fusion takes place. Unlike thermonuclear reactions in the regular stars, these reactions due to zero-point vibrations in the lattice are known as pycnonuclear reactions. These reactions are almost temperature independent and even occurs at T = 0 K (Gasques et al., 2005) but

do depend on the lattice structure e.g. face-centered cubic (fcc) or body centered cubic (fcc) and the properties of neutron rich nuclei. These reactions along with the electron capture reactions are a primary source of heat for the crust. This heat later transports up (and down) and plays an important role in the surface phenomenon like ignition conditions for type-I X-ray bursts and superbursts.

The downward journey of the accreted elements into the neutron star's interior explores the density regimes ranging several orders of magnitude. The different nuclear processes convert the elements to very proton-rich (rp-process) and then to very neutron-rich elements (via electron capture). After various nuclear processes, they settle down in a rigid lattice to form a crust. Thus phenomenon on the surface dictates the crust composition, and crust process (heating and thermal conductivity) controls the surface phenomenon. Thus, accreting neutron stars serve as natural laboratories to study behaviour of very neutron-rich and proton-rich matter as well as matter as the extreme temperatures and densities. To study matter at it's extreme, it is important to connect these process to the observations. Observational constraints and link to the underlying physics are described in the next section.

1.2.2 Observations: X-ray bursts and crust composition

The question of whether ashes of the rp-process could be ejected during the burst (or ever) become part of the interstellar medium is still under debate (in 't Zand et al., 2014). However, irrespective of the alternate suggestion, the nuclear burning is of central importance as they influence the light curves of the bursts. From their observations, both during bursts and quiescent phase, a plethora of information can be extracted about nuclear burning, crust composition, neutron star mass and radius and hence an equation

of state of dense nuclear matter (Ozel et al., 2016).

Various works have emphasized the importance of type-I X-ray burst light curve models to interpret the observations (Heger et al.,2007; Zamfir et al., 2012). Reliable models are required to fit observed light curves and hence fix the overall luminosity scale in a source distance independent approach (Zamfir et al., 2012). This information can then be used to extract the surface redshift and hence neutron star compactness. However the shape of light curves depends on the nuclear burning. Uncertainties in nuclear reaction rates and beta-decay half-lives lead to uncertainties in light curve modeling (Cyburt et al., 2016). Therefore nuclear data are required to create a set of model templates for matching specific bursts to analyze observations.

The other direct observations are from crust cooling during the quiescent phase. In an accreting neutron star, the outer crust has a mass around $10^{-4} M_{\odot}$. For a typical mass accretion rate for LMXBs ($10^{-8} - 10^{-10} M_{\odot}$), the amount of material in the outer crust can be replaced in 10^4 to 10^6 years. These timescales are much shorter than the mass transfer phase in low-mass X-ray binaries. Therefore, one expects the neutron stars in LMXBs have accreted crust (Schatz & Rehm, 2006). During the quiescent phase after a prolonged burning, the surface emission is dominated by thermal flux from the crust. The crustal heating is directly mapped using cooling light curves in the quiescent phase. The models of thermal relaxation of neutron star crust depend sensitively on the thermal conductivity of the crust. This thermal conductivity is dominated by the impurity scattering (Schatz et al.,1999; Horowitz et al.,2009) which is strongly composition dependent. As discussed earlier, the composition of the crust is set by rp-process ashes which sinks deeper into the neutron star. In the crust, the electron-ion scattering frequency is strongly reduced for $T << T_p$, the plasma temperature and conductivity is no more given by equation 1.3 . At $T << T_p$, electrons predominantly scatters off from various irregularities (ion impurities) of the crystalline structure and this scattering is

called impurity scattering. When impurity scattering is the dominating process during the crust relaxation, the thermal conductivity is given by (Brown & Cumming, 2009):

$$K = \frac{\pi^2 n_e k_b^2 T}{3 m_e \nu_{eQ}} \tag{1.6}$$

Here, ν_{eQ} is the scattering frequency that depends directly on the impurity parameter Q_{imp}. The impurity parameter is defined as

$$Q_{imp} = n_{ion}^{-1} \sum_i n_i (Z_i - < Z >)^2 \tag{1.7}$$

This impurity parameter measures the distribution of nuclide charge number and depends directly on rp-process ashes. The impurity parameter depends the burst ashes and if composition of burst ashes are constrained, crustal cooling models can be used to to decipher the information about crust. Figure 1.3 shows the light curves of MXB 165929, fitted with the crustal cooling model (using A. Cumming's open source code) for different choices of the impurity parameter Q_{imp} in the crust (Brown & Cumming, 2009).

Therefore, crust composition depends on the surface processes (rp-process) and electron capture in the crust. Nuclear reaction rate and decay rate inputs to rp-process nucleosynthesis, electron capture processes, and pycnonuclear reactions, are all uncertain and the solid laboratory experimental efforts are required to constrain these inputs . The nuclear physics and experiments in the laboratories are explained in subsequent sections.

1.3 Nuclear burning networks of X-ray bursts

In this section, details of the nuclear burning processes that power type-I X-ray bursts will be discussed. The nuclear burning can be described in two major phases. The

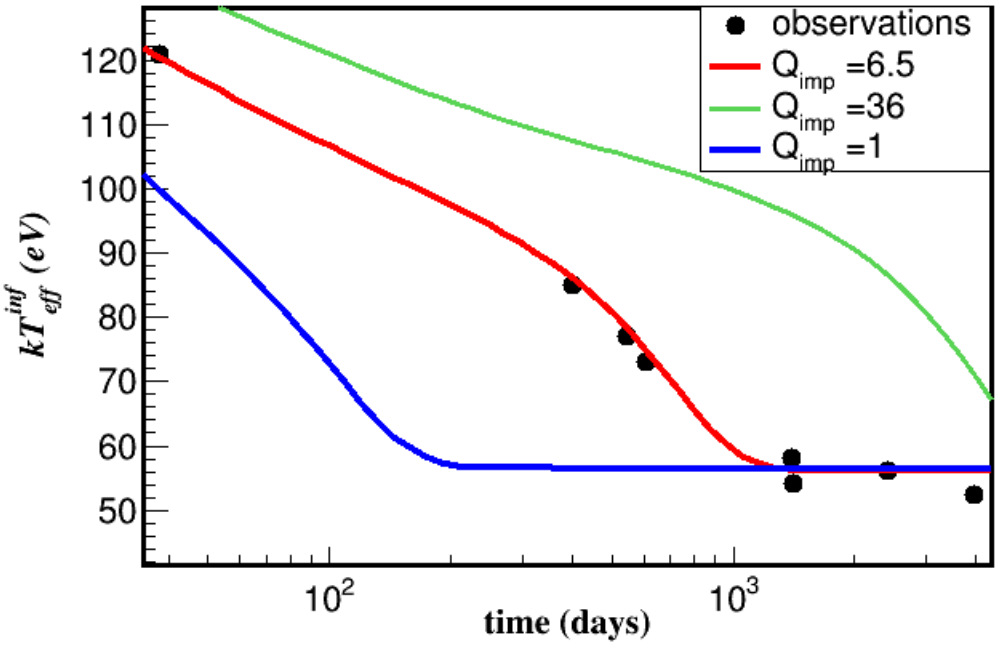

FIGURE 1.3: Light curves of MXB 165929, for different choices of the impurity parameter Q_{imp} in the crust using A. Cummings open source code crustpy (Brown & Cumming, 2009). The cooling curves are highly sensitive to impurity parameter

.

operation of hot CNO cycles before the burst. The onset of triple alpha reactions leading to the burst and as temperature rises break out reactions from hot CNO cycles lead to the αp process and rp-process. The operation of the rp-process is the primary source of energy generation and significantly shapes the X-ray burst light curves. The hot CNO cycles, break out reactions from these cycles, αp and rp-processes are described in the following sub-sections.

HCNO CYCLE 1	HCNO CYCLE 2	HCNO CYCLE 3
$^{12}C(p,\gamma)^{13}N$	$^{15}O(\beta^{+}\nu)^{15}N$	$^{15}O(\beta^{+}\nu)^{15}N$
$^{13}N(p,\gamma)^{14}O$	$^{15}N(p,\gamma)^{16}O$	$^{15}N(p,\gamma)^{16}O$
$^{14}O(\beta^{+}\nu)^{14}N$	$^{16}O(p,\gamma)^{17}F$	$^{16}O(p,\gamma)^{17}F$
$^{14}N(p,\gamma)^{15}O$	$^{17}F(\beta^{+}\nu)^{17}O$	$^{17}F(p,\gamma)18Ne$
$^{15}O(\beta^{+}\nu)^{15}N$	$^{17}O(p,\gamma)18F$	$^{18}Ne(\beta^{+}\nu)^{18}F$
$^{15}N(p,\alpha)^{12}C$	$^{18}F(p,\alpha)^{15}O$	$^{18}F(p,\alpha)^{15}O$

TABLE 1.1: hot CNO cycle paths (adapted from Iliadis, 2010)

1.3.1 Reaction pathways and waiting points

1.3.1.1 Hot CNO cycles

The hot CNO cycles (also known as beta-limited cycles) are sequences of nuclear reactions and beta decays in which hydrogen is burned to helium, and CNO elements act as a catalyst. The major difference between CNO cycles and HCNO cycles is that in the latter temperatures are high enough that proton capture can compete with beta decays of short-lived nuclei formed during the cycles. For example, in CNO cycles (or cold CNO cycles) once ^{13}N is produced via $^{12}C(p,\gamma)^{13}N$ reaction the further processing has to wait for ^{13}N beta decay i.e. $^{13}N(\beta^{+}\nu)^{13}C$ (Wiescher et al., 2010). However, at elevated temperatures (T = 0.1 -0.4 GK) a proton capture ($^{13}N(p,\gamma)^{14}O$) can be favoured over the beta decay of ^{13}N. Further, depending on the fate of ^{15}N and ^{17}F the HNCOs can be described with three different reaction paths, each dominating at a particular temperature and density conditions. Table 1.1 shows the reaction flows for these three *hot* CNO cycle paths. In HCNO1, $^{15}N(p,\alpha)^{12}C$ closes the cycles whereas in HCNO2 and HCNO3, $^{18}F(p,\alpha)^{15}O$ closes the cycles where ^{18}F is produced via two different sequences. The operation of *hot* CNO cycles thus converts four hydrogen atoms to a helium atom and CNO elements act as the catalyst.

1.3.1.2 Beak out from hot CNO cycles

The triple alpha reactions trigger the burst and as the temperature increases the reactions leading to the breakout from the *hot* CNO cycles become active. The reaction flow spends considerable time on the waiting points (i.e. the nuclei where further flow depends on their beta decay). Even though many different break-out reactions are possible, two main breakout reactions at two major waiting points in X-ray bursts are particularly important. These two major waiting points are ^{15}O and ^{18}Ne. The two main breakout reactions considered to bypass these two crucial waiting points are $^{15}O(\alpha,\gamma)^{19}Ne$ and $^{18}Ne(\alpha,p)^{21}Na$ respectively. The reaction $^{15}O(\alpha,\gamma)^{19}Ne$ can be followed by the reaction $^{19}Ne(p,\gamma)^{20}Na$, hence both break out sequences leads to the sodium isotopes. Both these reactions need availability of alpha particles. The other possibility to bypass these waiting points are two proton capture reactions: $^{15}O(2p,\gamma)^{17}Ne$ and $^{18}Ne(2p,\gamma)^{20}Mg$ (Görres et. al (1995)). If these two reactions are included the possible breakout reaction channels can be

$^{15}O(\alpha,\gamma)^{19}Ne(p,\gamma)^{20}Na$
$^{17}F(p,\gamma)^{18}Ne(2p,\gamma)^{20}Mg$
$^{15}O(2p,\gamma)^{17}F(p,\gamma)^{18}Ne(\alpha,p)^{21}Na$
$^{15}O(2p,\gamma)^{17}F(p,\gamma)^{18}Ne(2p,\gamma)^{20}Mg$

along with other possible combinations. Out of various possible breakout sequences, the reaction paths followed during burst depends on the reaction rates and beta decay rates. Figure 1.4 shows the prominent flow of the CNO cycles and possible breakout reactions.

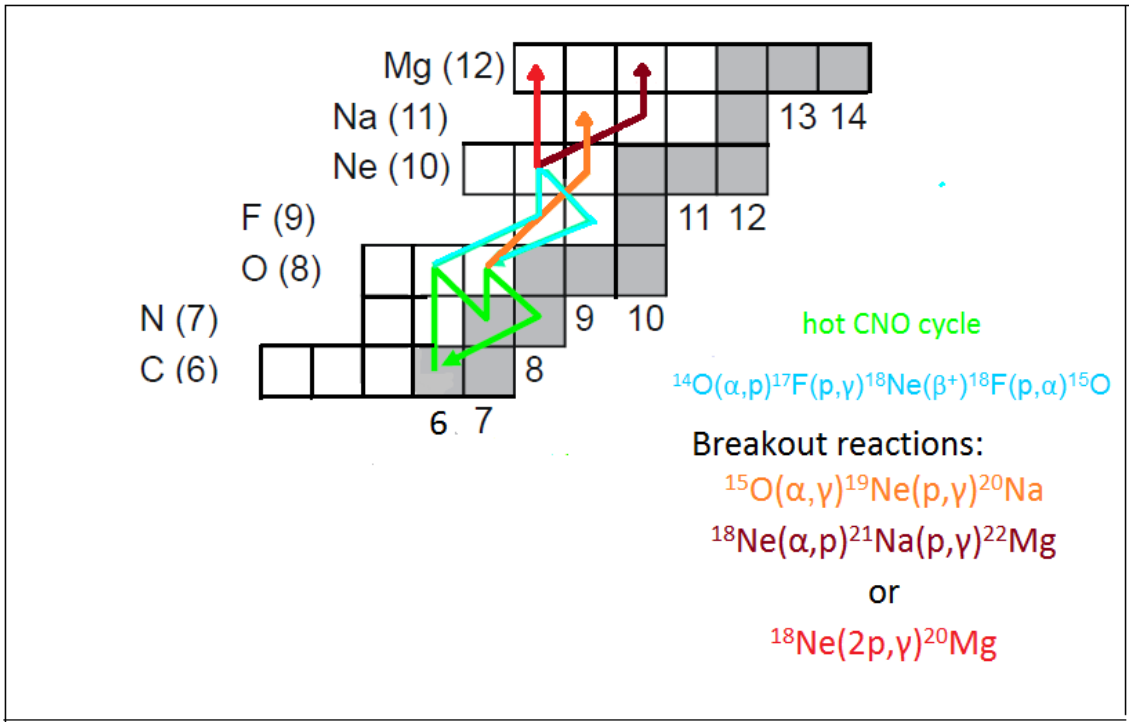

FIGURE 1.4: Break out from hot CNO cycles

1.3.1.3 αp and rp processes

The nucleosynthesis beyond the hot CNO cycle mass region flows via a sequence of αp reactions and rp-process. Most of the hydrogen is burned by the rp-process which a series of rapid proton captures, and slow beta decays close to the proton drip line (Wallace & Woosley 1981). However in the mid-mass nuclei αp-process can compete with the rp-process. In αp-process, (p,γ) reaction follows the (α,p) reaction. This process is pure helium burning since for the proton released in exit channel of the (α,p) a proton is captured in the (p,γ) reaction. Therefore in αp-process nuclei do not have to wait for beta decay. In most of the X-ray bursts environments αp process can be described as the following sequence of reactions (Schatz & Rehm, 2006)

$$^{14}O(\alpha,p)^{17}F(p,\gamma)^{18}Ne(\alpha,p)^{21}Na(p,\gamma)^{22}Mg(\alpha,p)^{25}Al(p,\gamma)^{26}Si(\alpha,p)^{29}P(p,\gamma)^{30}S$$

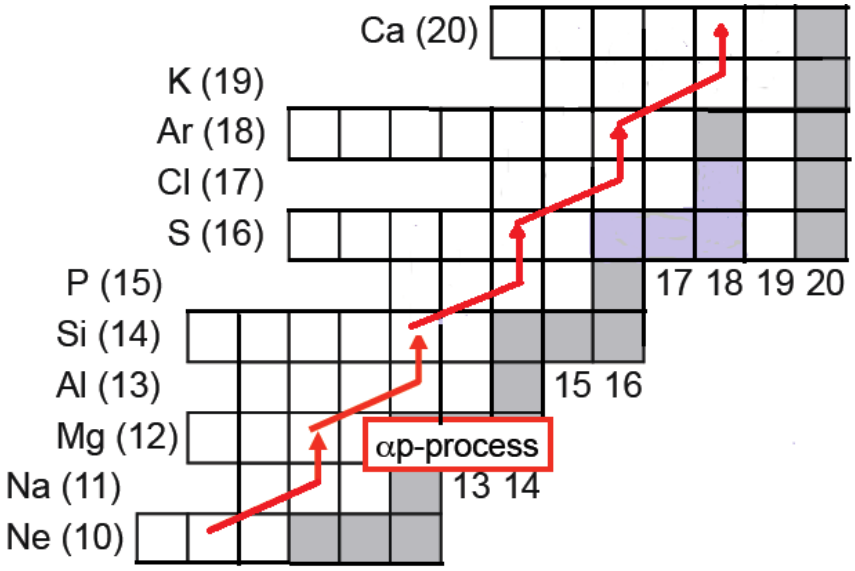

FIGURE 1.5: Flow of αp- process.

$(\alpha,p)^{33}Cl(p,\gamma)^{34}Ar(\alpha,p)^{37}K(p,\gamma)^{38}Ca(\alpha,p)^{41}Sc$

The αp-process does not extend beyond Sc because as atomic number increases, the Coulomb barrier increases and (α,p) reactions get lesser probable comparative to (p,γ) reactions. Beyond these points, heavier elements are synthesized through hydrogen burning via rp-process. Figure 1.5 shows the flow of αp-process in medium mass nuclei.

In the rp-process, major flow towards heavier mass region takes place through ^{56}Ni which is another waiting point. The reaction to bypass this waiting point is $^{56}Ni(p,\gamma)^{57}Cu$. The rate of this reaction has been investigated through various ways (Simon et al., 2013). The major waiting points beyond this part are ^{64}Ge,^{68}Se and ^{72}Kr. The case of ^{68}Se and ^{72}Kr reflects the importance of the pairing interaction along the proton dripline. Due to the pairing interaction even-Z nuclei are relatively stable (^{68}Se and ^{72}Kr have half-lives of 35.5 s and 17 s respectively) whereas the neighboring Z+1 nuclei are proton unbound. Therefore proton capture on ^{68}Se and ^{72}Kr leads to proton unbound nuclei. This means

that these nuclei either have to wait for beta decay or a sequential two proton capture reactions can bridge such waiting points.

1.3.1.4 End point of the rp-process

The end point of the rp-process has been discussed in detail by Schatz et al.(2001). The *rp* process ends in a closed SnSbTe cycle. Processing beyond Sn (through (p,γ)) can only take place if proton capture on Sn leads to an isotope of Sb which is sufficiently proton bound for the (γ,p) reaction to be small. This is possible only for ^{105}Sn as proton capture leads to ^{106}Sb. But further proton capture leads to ^{107}Te which is known to be an alpha emitter. This alpha emission brings the reaction flow back to Sn. There are some other weak branches of flow but $^{106-108}$Te are all alpha unbound, and hence alpha emission closes the cycle. The slow hydrogen burning beyond Ni via the rp-process is a key to long X-ray burst tail and hence gives characteristic shape to X-ray burst profile. The αp process (discussed before) shapes the X-ray light curves at earlier times and break out from hot CNO cycle is important during rise time of the burst. Understanding these nuclear processes in detail is a prerequisite for the interpretation of X-ray burst light curves.

The rapid capture process in the rp-process makes the nuclear burning during X-ray bursts flow along the proton drip line. Therefore, reaction rates and beta decay rates for highly unstable nuclei are needed. For this reason, to constrain nuclear physics inputs in the laboratory, radioactive ion beam (RIB) facilities are the best places for such study. The next section explains the reactions rates and their experimental evaluation using radioactive beams in nuclear physics laboratories.

1.3.2 Reaction rates and cross sections

In the stellar plasma, the energy available for nuclei to fuse together is due to the thermal motion. Even though temperatures in the core are of the order of a million Kelvins, this energy is still not sufficient to overcome the Coulomb barrier. Thus, these nuclei fuse together via a quantum tunneling process. The particles for the typical temperature and density conditions present in the stellar core follows the Maxwell-Boltzmann distribution. The reaction rate per pair particle for a particle induced reaction can be written as (Burbidge et al., 1957 ; Fowler et al., 1967)

$$N_A < \sigma v >= (\frac{8}{\pi\mu})^{1/2} \frac{N_A}{(kT)^{3/2}} \int_0^\infty E\sigma(E) e^{-E/kT} dE \tag{1.8}$$

where σ(E) is the energy dependent cross section and factor $e^{-E/kT}$ comes from the Maxwell-Boltzmann distribution, k is the Boltzmann constant, and μ is the reduced mass of the two nuclei fusing. The reaction rate is obtained by solving the above integral numerically. Here, it must be noted that most of the discussion on thermonuclear reaction rate formalism described in this thesis applies only to charged-particle reactants and not to neutron-induced reactions. To solve the above equation, knowledge about energy dependent cross sections ($\sigma(E)$) is required. The cross section can vary smoothly with the energy (direct/non-resonant cross sections) or if the reaction occurs at nuclear resonance the cross section spikes at these energies. However, if the energy dependence of the reaction rate is simple then the above integral can be solved analytically. For this purpose the reaction rate can be written as combination three terms explicitly:

$$< \sigma v >=< \sigma v >_{resonant} + < \sigma v >_{direct} + < \sigma v >_{tail} \tag{1.9}$$

where $< \sigma v >_{resonant}$ denotes the contribution from resonances, $< \sigma v >_{direct}$ is direct capture part (or non-resonant part) and $< \sigma v >_{tail}$ is the contribution from tails of resonances. The two major contributions to the reaction i.e. non-resonant and resonant

reaction rates are discussed below.

1.3.2.1 Non-resonant reaction rate

If the cross section varies smoothly with the energy, the reaction rate can be obtained analytically. This is done by introducing the astrophysical S-factor. The cross section can be defined as the following:

$$\sigma(E) = \frac{1}{E} e^{-2\pi\eta} S(E) \tag{1.10}$$

Here S(E) is the astrophysical S-factor, 1/E is the geometrical factor and $e^{-2\pi\eta}$ is the Gamow factor which takes into account the transmission probability through the Coulomb barrier and can be written as $2\pi\eta = b/E^{1/2}$ (here $b = 0.989534 * Z_1 * Z_2 * \mu^{1/2}$). Here S(E) is a very slowly varying function, and it contains the nuclear information for individual nuclei. Putting the equation (1.10) in equation (1.8) and assuming an energy independent astrophysical S-factor the reaction rate per pair particle can be written as

$$N_{A<\sigma v>} = (\frac{8}{\pi\mu})^{1/2} \frac{N_A}{(kT)^{3/2}} S \int_0^\infty e^{(-E/kT - b/E^{1/2})} dE \tag{1.11}$$

The above integrand exhibits a broad peak, known as the Gamow peak, which defines the most relevant energy range for a reaction.

1.3.2.2 Narrow resonant reaction rate

If the reaction A+ x→ C+γ proceeds via a narrow resonance then the cross section is given by a single-level Breit-Wigner formula:

$$\sigma_{BW}(E) = \frac{\lambda^2}{4\pi}\omega\frac{\Gamma_x\Gamma_\gamma}{(E-E_r)^2+\Gamma^2/4} \tag{1.12}$$

Using equation (1.12) in (1.8), we have

$$N_A < \sigma v >= (\frac{2\pi}{\mu kT})^{3/2}\frac{h^2}{4\pi}\omega\gamma e^{-E_r/kT} \tag{1.13}$$

Here E_r is the resonance energy and $\omega\gamma$ is the resonance strength defined as

$$\omega\gamma = \frac{2J_r+1}{(2j_A+1)(2j_x+1)}\frac{\Gamma_x\Gamma_\gamma}{\Gamma_{tot}} \tag{1.14}$$

Here J_r is the spin of the resonance in C, j_A is the spin of the heavy particle and j_x is the spin of the lighter particle, Γ_x and Γ_γ are the partial energy widths for decay by emission of particle 'x' and 'γ', respectively and Γ_{tot} is total width of the resonance state (Blatt & Weisskopf, 1952). From the equation (1.13) it is clear that to determine the resonant reaction rate, one needs to know the resonance energy as well as the resonance strength. There are various ways to determine the non-resonant and resonant reaction rate using radioactive ion beams and the next section explains various methods to extract this information.

1.3.3 Experiments with radioactive ion beams

The advances in the radioactive beam facilities in the past three decades have opened up a new window for laboratory astrophysics. Most of the elements beyond nickel are formed in the most explosive environments in the Universe. This explosive nucleosynthesis

proceeds either through very neutron-rich (r-process) or proton drip-line (rp-process) areas of the nuclear chart. These parts of the nuclear chart are still unexplored as these nuclei have very short half lives and are extremely difficult to be produced and studied in the laboratory. To improve the nuclear physics input for nucleosynthesis studies laboratory investigations with the radioactive nuclei are important. Hence lot of effort has gone into developing the radioactive beam facilities where nuclear reactions and other processes involving the radioactive nuclei can be studied. The world's radioactive beam facilities can be broadly divided into two categories based on their radioactive beam production mode: Isotope separation online (ISOL) technique, and in-flight technique (D'Auria, 1995). These two techniques are briefly discussed beow.

- **ISOL method**

  In ISOL facilities, the high-intensity primary beam of light particles from an accelerator impinges on a thick hot target. The fragmentation and fission process of the target produces many exotic nuclei during this process, and for extraction, these nuclei have to diffuse and effuse to an ion source for ionization. Since the primary beam is generally of very high intensity even nuclei with very low production cross sections are produced at the target. However many isotopes have too short of a lifetime to survive the diffusion process which is a limiting factor in the production of radioisotopes with extremely small lifetime. Since many exotic particles are produced in this process, it is necessary to separate out the isotope of interest using a mass separator. The examples of currently operating major ISOL isotope facilities are TRIUMF in Canada (Ball et al., 2011), and ISOLDE at CERN, in Switzerland. The experimental part of this thesis has been performed at TRIUMF, and this facility will be explained in Chapter 3.

- **In-flight (fragmentation) method**

  In this technique, the fragmentation of intense heavy ion beam targeted onto a

thin target is used to produce radioactive beams. The primary beam usually has high energies and fragments produced from it have high forward momentum. The fragments pass through a multi-stage fragment separator spectrometer and then subsequently used for further reactions. This method is independent of any target chemistry but to achieve beam with good ion optical qualities is challenging.

1.3.4 Experiments for reaction rate determination

1.3.4.1 Direct measurements

Most of the reactions in the stellar environments are capture reactions; reactions in which a particle is captured, and photon (gamma) is emitted in the exit channel (for example A(x,γ)B). The best way to determine the reaction rate is to measure the reaction cross sections directly at the energies relevant to stellar environments. In relatively stable nuclear burning, the particle captures takes place on the stable nucleus; $a + X \rightarrow Y + \gamma$ where a is the lighter particle (p,n,α), X is stable nucleus. To measure such cross sections, it is relatively easy to make a target of the heavier nucleus (X) in the laboratory and bombard it with an intense beam of stable lighter particles. The products of the reactions are measured, and their counts relative to beam counts (along with other normalizing factors) gives us the probability of interaction. The cross sections need to be measured in the Gamow window of a particular reaction, and for most of the stellar environments, this energy is very small. The detection of gamma rays as a product of reactions at these small energies is extremely difficult as this is masked by inherently large gamma rays background. To measure reactions directly inside the Gamow window, underground laboratories provide the best place to suppress gamma ray background. Further, the heavy particle in the reaction products can also be detected in coincidence with the gamma rays. To separate heavier beam-like particles from the

beam particles generally, mass separators are employed.

To determine the reaction rates for reactions in explosive environments, the targets of heavy particles in the laboratory cannot be deployed anymore as these nuclei are radioactive. Therefore these reactions studies have to be performed in inverse kinematics in which target of light particles are deployed and irradiated with a radioactive beam of heavy particles. For example $X + a \rightarrow Y + \gamma$, here a is the target (e.g. proton), and X is the radioactive heavy particle. To directly measure the reaction cross sections, the ratio of the total number of nuclear reactions occurred to the total number of the incident beam particles is determined. The ratio of these two numbers is called the yield (Y) of the reaction i.e.

$$Y = \frac{total\ number\ of\ nuclear\ reactions}{total\ number\ of\ incident\ beam\ particles} \tag{1.15}$$

The total yield can be written as (Illiadis, 2010)

$$Y(E_0) = \int_{E_0 - \Delta E}^{E_0} \frac{\sigma(E)}{\epsilon(E)} dE \tag{1.16}$$

here E_0 is the incident energy, ΔE is the total energy loss in the target , $\sigma(E_0)$ is the energy dependent cross section, $\epsilon(E_0)$ is stopping power (eV cm^2/atom) defined as

$$\epsilon(E) = -\frac{1}{N}\frac{dE}{dx} \tag{1.17}$$

and N in above equation is defined as $N = \frac{N_t}{Ad}$ where N_t and N denotes a total number of target nuclei and number density of target nuclei respectively and d is target thickness. In equation 1.16, if the yield is measured through the experiment then $\sigma(E)$ can be determined by solving the equation numerically. However, the capture cross sections are so small that yields are too low to extract information on reaction cross section. The production of radioactive beams far away from stability valley is tough, and intensities

of the beam particle are too small (especially for nuclei at neutron or proton drip line) to directly measure the reaction cross section. For this reason, many indirect methods are used to extract relevant nuclear information required to evaluate the reaction rate.

1.3.4.2 Indirect methods

The reaction rate, as mentioned earlier, is mainly divided into two major contributions i.e. direct capture and resonant capture. Here, I have focused on the indirect methods to get resonant reaction rate for charged particle induced reactions. As described in Equation 1.13, the resonant reaction rates can be estimated if we know the resonance energies and respective resonance strengths in the energy range relevant to the stellar environment. The knowledge of resonance energies is of critical importance as the reaction rate varies exponentially with the resonance energy (see Equation 1.13). In a resonant capture, the reactions proceed via a compound nucleus, and if the reaction is (p, γ) type then the resonant reaction can be written as:

$$p + X \rightarrow Y^*(exc) \rightarrow Y + \gamma \tag{1.18}$$

Here Y^* is compound nucleus (here, a heavier end product in the excited state). The excited state in the nucleus Y above the particle emission threshold (i.e., above p+X threshold) is known as a resonance state. This means that these states are particle unbound states and decay via particle emission. However, there is also a probability that these states can undergo gamma ray emission and the nucleus de-excites to the particle-bound state. This probability of de-excitation via gamma emission leads to the resonant part of the capture reaction. The particle or gamma emission probabilities are defined through partial energy widths Γ_x and Γ_γ (i.e. particle width and gamma width respectively, as discussed in equation 1.14). Therefore, to determine resonance strength, one needs to estimate the partial widths and spin of the resonance (Equation 1.14).

The resonance energies can be determined through various ways and missing mass technique is one of the important methods. Since this technique has been used in this thesis work, it is explained later in detail in Chapter 3. To measure partial widths for resonance strength, many methods are used. If the particle decay widths are large compared to gamma widths, then in Equation 1.14, $\Gamma_{tot}(= \Gamma_x + \Gamma_\gamma)$ can be written as $\Gamma_{tot} \approx \Gamma_x$. Therefore equation (1.13) becomes

$$\omega\gamma = \frac{2J_r + 1}{(2j_A + 1)(2j_x + 1)}\Gamma_\gamma \tag{1.19}$$

In this situation, resonance strength is determined by gamma width only, and it becomes utterly crucial to measure this width. The widths can be determined by measuring the lifetime. Lifetimes can be measured through various methods (e.g. Doppler shift attenuation Method) and hence can help in constraining resonance strength.

1.4 Organization of Dissertation

The rest of the thesis is divided into five more chapters, and the content of each chapter is explained below.

- Chapter 2

  This next chapter explains the scientific motivation for the experimental part, as well as for spallation modelling part in detail.

- Chapter 3

  This chapter explains the method to extract the experimental information, and provides details of the experimental facility IRIS, used for this thesis work, in detail. In includes the details of missing mass technique, discussion of various

detectors, followed by details of electronics and data acquisition components required.

- Chapter 4

  Chapter four discusses the simulations and data analysis for the experiment. It includes the Monte Carlo simulations for experimental setup optimization and background analysis, detector calibrations, target thickness monitoring, particle identification, excitation spectrum and angular distribution analysis.

- Chapter 5

  Here, the results obtained and their implications for X-ray bursts, as well as for nuclear structure studies and interactions, are overviewed and explained.

- Chapter 6

  This chapter explains the proton induced spallation of accreted material in the atmospheres of an accreting neutron star and survival of CNO elements.

Chapter 2

Scientific Motivation

The scientific motivation for this thesis work has been explained briefly in Chapter 1. In this chapter, we present a detailed discussion on the scientific background of ^{20}Mg(d, d′) investigation, as well as on spallation of accreted material in the atmospheres of accreting neutron stars. The experimental focus is to constrain the ^{18}Ne(2p, γ)^{20}Mg reaction rate by investigating the resonant state(s) in ^{20}Mg, which also will provide new structure information at the proton drip-line . We have also made calculations to investigate the spallation of accreted material in the atmospheres of accreting neutron stars and its possible impact on the burst properties has been considered. Section 2.1 outlines the background that motivates the experimental part. The importance of ^{18}Ne as a waiting point and possible breakout reactions to bypass this waiting point are discussed in Section 2.1.1 . The formalism to evaluate the sequential two proton capture reactions, i.e. (2p,γ), and physical quantities required to assess these rates will be explained in Section 2.1.2 . Section 2.1.3 explains the current information on excited states in ^{20}Mg based on various theoretical predictions. Section 2.2 explains the importance of CNO elements and compositional change due to spallation reactions in the collisional stopping of accreted elements. It highlights the need for cascading destruction process which has

been considered in this study.

2.1 Background of the $^{20}\mathrm{Mg}(\mathrm{d},\mathrm{d}')$ experiment

The major waiting points in the thermonuclear burning on the surface of neutron stars have been explained in the section 1.2.1 of the chapter 1. Out of these various waiting points, our focus here is on ^{18}Ne.

2.1.1 ^{18}Ne as waiting point and break out reactions

During hydrogen burning via hot CNO cycles, ^{18}Ne is formed mainly through the proton capture on ^{17}F; i.e. $^{17}\mathrm{F}(\mathrm{p},\gamma)^{18}\mathrm{Ne}$ (Wiescher et al., 2010). However, this flow cannot continue as proton capture on ^{18}Ne leads to proton unbound ^{19}Na. This means as soon as ^{19}Na is formed via $^{18}\mathrm{Ne}(\mathrm{p},\gamma)^{19}\mathrm{Na}$, it immediately decays back to ^{18}Ne through proton emission. Therefore, ^{18}Ne has to wait for beta decay to ^{18}F i.e. $^{18}\mathrm{Ne}(\beta^{+}\nu)^{18}\mathrm{F}$. However, due to extreme temperature and density conditions during X-ray bursts, this waiting point could be bypassed. The reactions that have been proposed to bypass this waiting point are $^{18}\mathrm{Ne}(\alpha,\mathrm{p})^{21}\mathrm{Na}$ (Weischer et al., 1999) or $^{18}\mathrm{Ne}(2\mathrm{p},\gamma)^{20}\mathrm{Mg}$ (Görres et al., 1995). The fate of ^{18}Ne depends on the rate of these reactions as well as the beta decay rate of ^{18}Ne at temperature and densities relevant to the burst conditions. Both these reactions mentioned above take nuclear flow to the next mass regions and are hence called the breakout from hot CNO cycles. There have been experimental efforts to constrain the $^{18}\mathrm{Ne}(\alpha,\mathrm{p})^{21}\mathrm{Na}$ reaction rate and some experimental information exists for it (Salter et al., 2012). However, on the other hand, there is no experimental information on $^{18}\mathrm{Ne}(2\mathrm{p},\gamma)^{20}\mathrm{Mg}$ reaction rate and current estimates are based on theoretical models (Görres et al.,1995). To understand the ingredients required to evaluate two proton capture reaction rate let's look at the 2p-capture reaction rate formalism.

2.1.2 Two proton capture reaction rate formalism

The sequential two proton capture reaction rates proceed through a two-step mechanism (Nomoto et al.,1985). The proton capture on ^{18}Ne leads to the formation of ^{19}Na which is proton unbound and decays back to ^{18}Ne via proton emission. For the formation of ^{20}Mg, ^{19}Na has to capture another proton before its decay. The rate of formation of ^{20}Mg can be written as

$$\dot{N}_{(^{20}Mg)} = N_{(^{19}Na)} N_p \langle \sigma v \rangle_{^{19}Na(p,\gamma)} \tag{2.1}$$

Here $N_{(^{19}Na)}$ and N_p are number densities of Na and protons respectively and $\langle \sigma v \rangle_{^{19}Na(p,\gamma)}$ is the reaction rate per pair particle. In Equation (2.1), the number density of ^{19}Na i.e. $N_{(^{19}Na)}$ is unknown as it is proton unbound and decays back to p+^{18}Ne. To estimate $N_{(^{19}Na)}$ in Equation (2.1), first let's look at the rate of change of ^{19}Na abundance. This can be written as

$$\dot{N}_{(^{19}Na)} = N_p N_{(^{18}Ne)} \langle \sigma v \rangle_{^{18}Ne(p,p)} - \frac{\Gamma}{\hbar} N_{(^{19}Na)} \tag{2.2}$$

Here, first term in Equation (2.2) is the rate of formation of ^{19}Na and second term is rate of destruction of ^{19}Na by proton emission. In Equation (2.2), the N_p and $N_{(^{18}Ne)}$ are proton and ^{18}Ne number densities and $\langle \sigma v \rangle_{^{18}Ne(p,p)}$ is the reaction rate per particle pair. Γ is the proton decay width for ^{19}Na. In equilibrium, the rate of formation for ^{19}Na is equal to rate of destruction i.e. $\dot{N_{(^{19}Na)}} = 0$. Therefore, from Equation (2.2) we get,

$$N_{(^{19}Na)} = N_p N_{(^{18}Ne)} \langle \sigma v \rangle_{^{18}Ne(p,p)} \frac{\hbar}{\Gamma} \tag{2.3}$$

Using Equation (2.3) in Equation (2.1), we get following expression for reaction rate

$$\dot{N}_{(^{20}Mg)} = \frac{2\hbar}{\Gamma} N_p^2 N_{(^{18}Ne)} \langle \sigma v \rangle_{^{18}Ne(p,p)} \langle \sigma v \rangle_{19Na(p,\gamma)} \tag{2.4}$$

Therefore by comparing Equation (2.1) and (2.4), the two proton capture reaction rate (per particle pair) is

$$N_A^2 \langle \sigma v \rangle_{^{18}Ne(2p,\gamma)^{20}Mg} = N_A^2 \frac{2\hbar}{\Gamma} \langle \sigma v \rangle_{^{18}Ne(p,p)} \langle \sigma v \rangle_{^{19}Na(p,\gamma)} \tag{2.5}$$

or in case of more than one resonance involved :

$$N_A^2 \langle \sigma v \rangle_{^{18}Ne(2p,\gamma)^{20}Mg} = N_A^2 \sum_i \frac{2\hbar}{\Gamma_i} \langle \sigma v \rangle_{^{18}Ne(p,p)_i} \langle \sigma v \rangle_{^{19}Na(E_i)(p,\gamma)} \tag{2.6}$$

Here Γ_i is the proton decay width (only decay channel) for each resonance at energy E_i in ^{19}Na. Here, the ground state and maybe several excited states are populated by $^{18}\mathrm{Ne(p,p)_i}$ reaction. The $\langle \sigma v \rangle_{^{19}Na(E_i)(p,\gamma)}$ part represents the reaction rate for second proton capture via each relevant resonance in ^{19}Na leading to ^{20}Mg i.e. $^{19}Na(E_i)(p,\gamma)^{20}Mg$. Therefore to evaluate the two proton capture rate on ^{18}Ne , we need to evaluate two rates in Equation (2.6). The first part is to evaluate $\sum_i \frac{2\hbar}{\Gamma_i} \langle \sigma v \rangle_{^{18}Ne(p,p)_i}$ which depends on the resonance energies (E_i) in ^{19}Na and their respective decay widths. The experimental information on the energy states in ^{19}Na exists (Skorodumov et al.,2006) therefore this part is constrained. The second part is proton capture on ^{19}Na, i.e. $\langle \sigma v \rangle_{^{19}Na(E_i)(p,\gamma)}$. This resonant reaction is given by:

$$\langle \sigma v \rangle_{^{19}Na(E_i)(p,\gamma)^{20}Mg(E_j)} = (\frac{2\pi}{\mu kT})^{3/2} \hbar^2 \sum_j \omega \gamma_{j,i} exp\left[-\frac{E_{j,i}}{kT}\right] \tag{2.7}$$

here $E_{j,i}$ are resonance energies of states in ^{20}Mg with respect to resonance state in ^{19}Na. i.e

$$E_{j,i} = E_j - (Q + E_i) \tag{2.8}$$

where Q is the Q value for second proton capture reaction. The rates from all the resonances in ^{19}Na to each resonance in ^{20}Mg is summed up. To calculate resonant reaction rate for $^{19}\mathrm{Na(p,}\gamma)^{20}$Mg from equation (2.7), therefore one needs to know the resonant

states in ^{20}Mg and the resonance strengths. The current knowledge of resonant states in ^{20}Mg is based on the theoretical predictions, and these theoretical frameworks are explained in Section 2.1.3.

2.1.3 Theoretical predictions for states in ^{20}Mg

The first predictions of resonant states in ^{20}Mg were provided by Görres et al.(1995) that were derived based on mirror symmetry to the states of mirror nucleus ^{20}O. A nucleus X is said to be the mirror nucleus of Y if the number of protons in X equals to neutrons in Y and number of neutrons in X is equal to the number of protons in Y. Here ^{20}Mg has 12 protons, and eight neutrons while ^{20}O has 8 protons and 12 neutrons. The mirror partner of proton drip-line nuclei are often easier to access experimentally because they are closer to the stable nuclei. In this case, the mirror nuclei to ^{20}Mg, i.e. ^{20}O, is only two neutrons away from stable ^{18}O . Therefore, the excited states in ^{20}O were investigated by Pilt et al.(1979) via $^{18}\mathrm{O(t,p)}^{20}\mathrm{O}$. Using isospin symmetry i.e. the strong force is invariant to protons and neutrons, one expects same binding energies in the mirror nuclei. However, the Coulomb interaction between the protons leads to change in excitation spectrum of mirror nuclei. The shifts from analog states in a mirror nucleus can be calculated using Thomas-Ehrman shifts (Thomas, 1952). Therefore by following the procedure for the Thomas-Ehrman shifts, the energy of excited states in ^{20}Mg were estimated using the experimentally known excited states in mirror nucleus ^{20}O (Görres et al., 1995; Langanke et al.,1986; Pilt et al., 1979). Table (2.1) shows the energies of analog states in ^{20}O, calculated excitation energies for ^{20}Mg and their respective spin and parities.

Predicted E_x (^{20}Mg) MeV	E_x (^{20}O) MeV	Adopted (J^π)
3.45	3.57	4^+
3.85	4.03	2^+
4.31	4.45	0^+
4.69	4.85	2^+
4.97	5.23	4^+

TABLE 2.1: Excited states predicted from mirror symmetry states (Gorres et al.,1995)

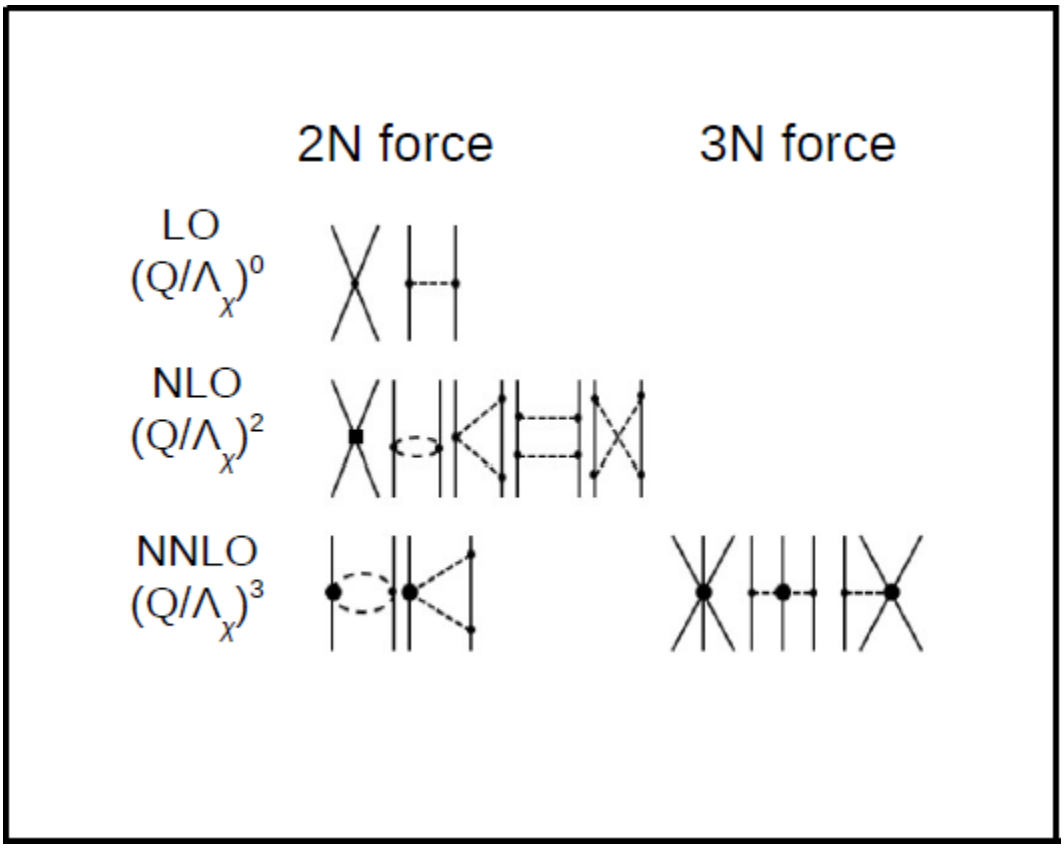

FIGURE 2.1: Hierarchy of the nuclear forces in Chiral perturbation theory (adapted from R. Machleidt & D. R. Entem, 2011). These diagrams represent the Feynman diagrams and depict the nuclear force as exchange of pions between nucleons. Here solid lines and dashed lines represent the nucleon and the pion, respectively.

However, nuclei such as ^{20}Mg either at proton or neutron drip-lines show new features that deviate from known rules. It is therefore unclear if the assumption of isospin symmetry and relation to the mirror states in ^{20}O will be applicable to ^{20}Mg. In more recent times, predictions of energy levels in such drip-line nuclei have been attempted from a description of nuclear forces based on chiral effective field theory, which is described below. A long-standing problem in nuclear physics is to understand the strong nuclear forces from first principles. As per our current understanding, the nuclear force (i.e. force between nucleons inside a nucleus) is a residual effect of more basic strong force which is responsible for holding together the quarks inside the nucleon (Machleidt & Entem, 2011). The fundamental strong force is described by quantum chromodynamics (QCD), but this theory is non-perturbative at length scales relevant to the nuclear physics. Therefore, it is highly challenging to develop a complete theory of the nuclear interactions, that governs many-body nuclei, from the fundamental constituent quarks and gluons. Currently, many phenomenological models exist for nucleon-nucleon potential. In the last few decades, there has been strong experimental evidence that the potentials based on two-nucleon forces only are not sufficient to explain systems with three or more nucleons (Navratil, 2007). Therefore the inclusion of three-nucleon forces is important and crucial to developing a potential for the multi-nucleon system. The phenomenological potentials have successfully explained various properties of light nuclei. However, these potentials have a large number of the adjustable parameters and therefore its predictive power approaching the drip-line is not firm. The other drawback is that the phenomenological potentials lack any relation to fundamental underlying QCD theory. An ultimate goal of nuclear physics is to develop a model with strong predictive power and a firm connection to the quantum chromodynamics. The chiral effective field theory provides such a link between nuclear forces and underlying strong forces. The chiral effective field theory is linked to the QCD via its symmetries and offers a natural explanation of observed hierarchy of nuclear forces $V_{2N} > V_{3N} > V_{4N}$. In effective field theory, the Lagrangian is written in terms of relevant degrees of freedom (nucleons and

pions), and symmetries of underlying QCD are respected. However, these Lagrangians give unlimited number of interaction diagrams for calculating the force. The remedy was provided by Weinberg (1990, 1991) who showed a systematic way of expansion in terms of $(Q/\lambda_\chi)^\nu$. Here $\lambda_\chi \approx$1 GeV is chiral symmetry breaking scale, Q is pion mass, and ν is the order of the expansion. In this approximation, for a given order ν the number of contributing terms are finite. The desired accuracy depends on the higher order terms taken into account in the theory. Figure 2.1 shows the hierarchy of the nuclear forces. Apart from the NN potential playing a dominating role, the three-nucleon forces (3N) appear at order $\nu = 3$. Recently Holt et al.(2013) provided a theoretical prediction of energy levels including 3N forces for proton-rich nuclei above mass region $A > 10$. In their study, they considered the shell model description of $N = 8$ isotones i.e. nuclei having eight neutrons (N=8). For ^{20}Mg the interactions among the valence protons on the top of ^{16}O core were determined, based on the nuclear forces from the chiral effective field theory. The 3N forces were included at N^{2}LO (next to next leading order) which consisted of the long-range two-pion-exchange part, one-pion-exchange as well as short-range contact terms. The general form of potential for effective field theory can be written as

$$V_{eff} = V_L + \delta V_{c.t} \tag{2.9}$$

Here V_L part is for long range interactions and $V_{c.t}$ is for contact terms which define the short range part. In the work of Holt et al. (2013), the shorter-range 3N couplings were determined by fits to the ^{3}H binding energy and the ^{4}He radius. The predicted excited states in ^{20}Mg in their study shows strong sensitivity to the 3N forces. The 3N forces provide the repulsive contributions, and their inclusion makes the state less bound compared to the case when only NN forces were considered.

Figure 2.2 shows a comparison of the predicted excited states in ^{20}Mg by Holt et al. (2013) based on chiral effective field theory and by Görres et al. (1995) based on mirror

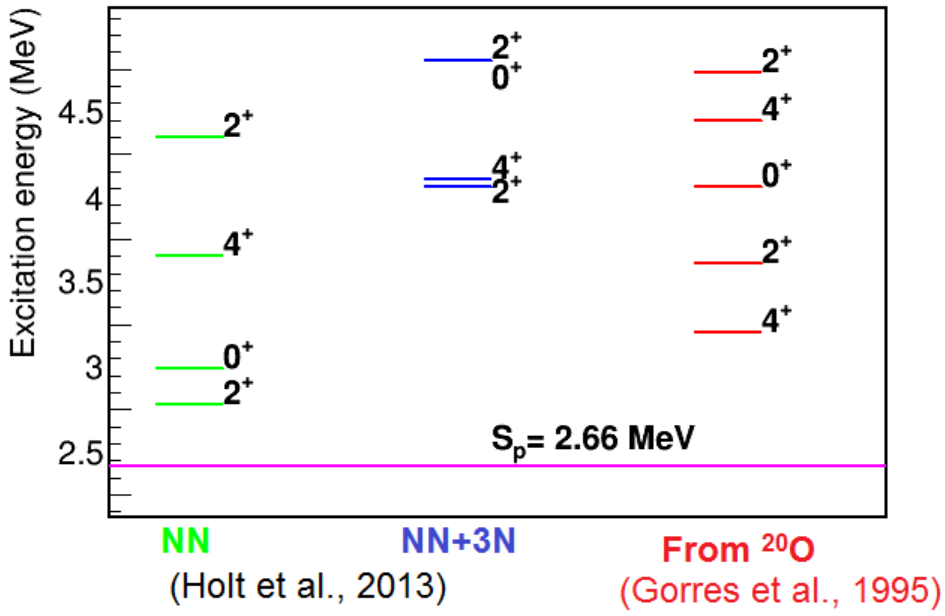

FIGURE 2.2: Excitation energy levels in ^{20}Mg from different theoretical predictions.

symmetry states in ^{20}O. This figure clearly demonstrates the remarkable difference in all the predictions. As outlined in Chapter 1 and in Section 2.1.2 of this section, the resonant reaction rate varies exponentially with the resonance energy. Therefore, various theoretical predictions of excited states provide very different estimates of ^{18}Ne(2p,γ)^{20}Mg reaction rates, shown in Figure 2.3. The reaction rate based on different predictions for excited states differ by several orders of magnitude. In fact ^{18}Ne(2p,γ)^{20}Mg can compete with the ^{18}Ne(α, p)^{21}Na if there are more than two resonances within the Gamow window. To constrain this reaction rate, it is utterly important to experimentally investigate the excited states in ^{20}Mg. Experimental determination of excited state states of ^{20}Mg will therefore also help in constraining the nuclear theory.

In this dissertation, we report the first experimental investigation of the excited states in ^{20}Mg above the proton emission threshold. The resonance states in ^{20}Mg have been probed through ^{20}Mg(d,d')^{20}Mg* inelastic scattering reaction using the experimental

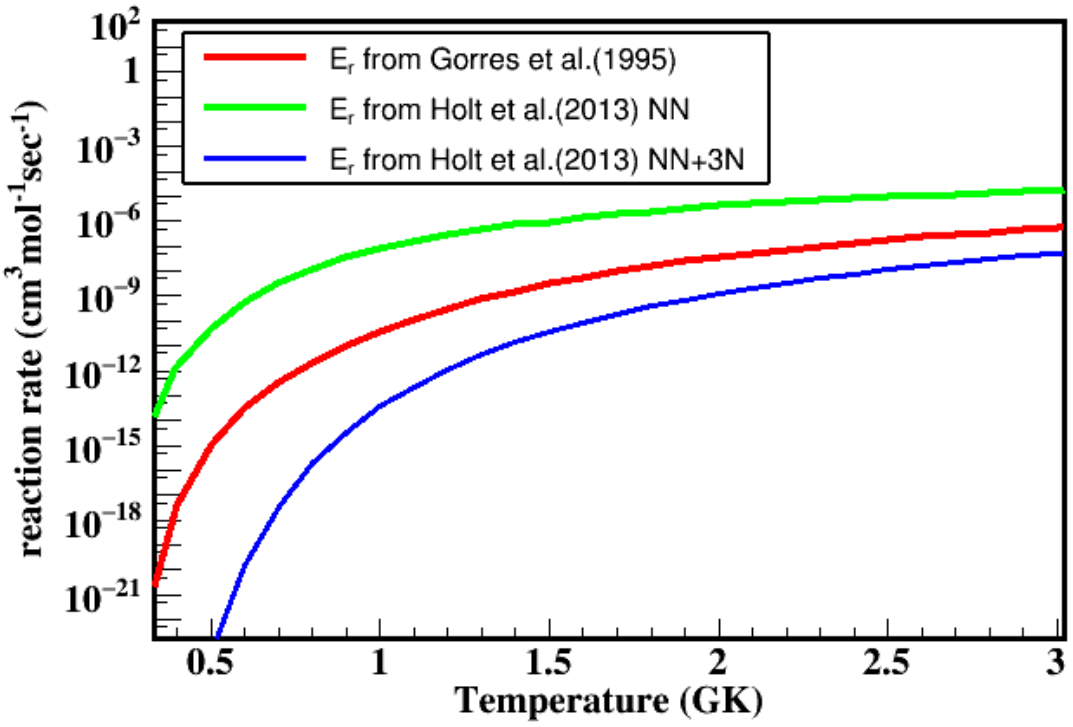

FIGURE 2.3: ^{18}Ne(2p, γ)^{20}Mg resonant reaction rate based on excitation levels shown in Figure 2.2

facility IRIS at TRIUMF, Canada. The deuteron target was used instead of proton target because deuteron emission threshold is much higher than proton emission threshold. The results of this experiment and its impact on the ^{18}Ne(2p,γ)^{20}Mg reaction rates, as well as on nuclear theory, will be discussed in detail in the Chapter 5.

2.2 Modelling spallation in neutron star atmospheres

The theoretical models for type-I X-ray bursts depend on a range of input parameters and initial abundance is one such major parameter (Woosley et al., 2004). In most of the X-ray burst models (multizone or single zone), initial abundances are based on the choice of a companion star and reflects the envelope composition of the companion. The metallicity of the companion star can vary depending on which population the donor belongs to. The impact of metallicity on the burst properties have been investigated in various studies (Woosley et al.,2004; Jose et al.,2010). These studies emphasized the importance of the abundances of CNO elements in particular. The CNO metallicity (Z_{CNO}) plays a vital role in deciding the ignition conditions for a given mass accretion rate (Cumming & Bildsten, 2000). The hydrogen is burned via hot CNO cycles, and the time needed to burn all hydrogen depends on initial hydrogen abundance and CNO metallicity. The X-ray burst is triggered when helium ignites unstably at the base of an accumulated layer. The composition at the time of ignition depends on how much hydrogen has burned during accumulation, which is determined by local accretion rate (Fujimoto et al.,1981). Helium ignites in the hydrogen-rich environment if mass accretion rate is greater than $m_{critical}$, where $m_{critical}$ is a function of Z_{CNO} and can be written as (Bildsten, 1997)

$$\dot{m}_{\rm critical} \approx \frac{4.2 \times 10^3 \text{ g cm}^{-2}\text{s}^{-1}}{g_{14}^{2/9} X} \left(\frac{0.04 \text{ cm}^2\text{g}^{-1}}{\kappa}\right)^{7/18} \times \left(\frac{Z_{CNO}}{0.01}\right)^{13/18}. \qquad (2.10)$$

Here X is the hydrogen mass fraction, κ is the opacity and $g = g_{14}10^{14}\ cm\ s^{-1}$. For accretion rates below this value, the hydrogen burns steadily and a pure layer of helium is accumulated.

It has been discussed previously that proton induced spallation of CNO elements in neutron star atmospheres can substantially change the accreted composition before it

settles down to the deeper layers of the neutron star (Bildsten et al.,1992). In their work it was shown that accreted material is stopped due to Coulomb collisions with atmospheric electrons, elements heavier than helium and hydrogen thermalize at higher altitudes in atmospheres. At those altitudes, incoming protons still have high enough energies to destroy these heavier elements through spallation reactions. The heavier ions are exposed to high energy protons in between their point of thermalization to proton stopping points in the atmosphere. Bildsten et al.(1992) investigated the destruction of CNO elements and showed that a tiny amount of CNO elements survive the spallation reactions. The change in accreted composition due to spallation can have a two-fold impact. Firstly, as discussed above the critical accretion rate (for mixed flashes or pure He flashes) depends on the CNO metallicity, and any alteration in CNO mass fraction changes ignition conditions and hence burst properties. Secondly, the change in the hydrogen and helium mass fraction through operation of hot CNO cycles prior to the burst could change the burst ashes.

In Bildsten et al.(1992), it was explicitly mentioned that the spallation of thermalized ions by protons lead to nuclear fragments which can further undergo fragmentation, hence resulting in a cascading destruction process. Due to a lack of knowledge of the relevant cross sections at that time, this full cascading fragmentation was not considered, and only isolated destruction of ^{12}C, ^{14}N and ^{16}O was taken into account. To get the final composition of material which settles down to the deeper layers of the neutron star, full cascading destruction process should be considered. Due to a cascading process, the replenishment of CNO elements due to destruction and fragmentation of elements heavier than CNO elements is possible.

In this work, we considered the full cascading destruction scenario, from iron to hydrogen, to get the final composition of accreted material after the spallation process.

The major focus of the present study is to see the effect of replenishment due to the destruction of heavier elements into the CNO elements. We have used the open source NucNet[1] tools to simulate the nuclear spallation reactions in the atmospheres of the accreting neutron stars. During spallation, both proton and neutron-rich fragments are produced, and these isotopes undergo beta decay. We have therefore considered beta decays along with the spallation reactions. The details of nuclear spallation modelling and results will be discussed in Chapter 6.

[1] https://sourceforge.net/projects/nucnet-tools/

Chapter 3

Description of the experiment

This chapter explains the experimental method used to measure the excited states in ^{20}Mg. Section 3.1 explains the missing mass technique used to find the excited states in ^{20}Mg, and the sections following that are dedicated to explaining the research facility IRIS used for this experiment.

3.1 Missing Mass Technique

The focus of this study is to find the excited states in ^{20}Mg above the proton emission threshold. There are various methods prevalent in nuclear physics to extract the information about excited states in a nucleus. We have used the missing mass technique to find the excited states in ^{20}Mg. The Q value of a reaction is defined as the difference in total masses of the nuclei before and after the reaction. For a given reaction, e.g. $A + B \rightarrow C + D$, the Q value can be written as (c=1, in natural units, therefore mc^2 is written as m here):

$$Q = m_A + m_B - m_C - m_D \tag{3.1}$$

If any of the particles in the exit channel (i.e. particle C or D) is in an excited state, from mass-energy equivalence the mass of excited particle will be different from its rest mass. In that case, Q value is unknown and cannot be calculated from the particle identification alone. However, Q value can be measured using the energy and momentum conservation. In Equation 3.1, let's assume that particle 'D' is in an excited state. Using energy and momentum conservation, the mass of particle 'D' can be written in terms of kinetic energies and scattering angles of other scattered particle (i.e. particle 'C') through the following relation:

$$\mathrm{m_D} = \sqrt{\mathrm{m_A^2} - \mathrm{m_B^2} + \mathrm{m_C^2} + 2\mathrm{m_B}(\mathrm{T_A} + \mathrm{m_A}) - 2(\mathrm{T_A} + \mathrm{m_A} + \mathrm{m_B})(\mathrm{T_C} + \mathrm{m_C}) + 2\mathrm{P_A}\mathrm{P_C} \times \cos(\theta_\mathrm{C})} \tag{3.2}$$

Here T_A and T_C are the kinetic energy of the species A and C, P_A and P_C is the relativistic momentum of the species A and C, respectively which can again be calculated from T_A and T_C. θ_C is laboratory angle of scattered particle C. Now the Q value can be obtained using Equation 3.1, once the kinetic energy and scattering angle of one of the scattered particles is measured and using Equation 3.2 in equation 3.1. To measure the excited states in ^{20}Mg, we have used deuteron inelastic scattering on ^{20}Mg, where an accelerated ^{20}Mg beam impinged on a stationary deuteron target. In relevance to discussion above, the reaction channel of interest is $^{20}\mathrm{Mg} + \mathrm{d} \rightarrow \mathrm{d}' + ^{20}\mathrm{Mg}^*$. The mass of $^{20}\mathrm{Mg}^*$ can be written as $m_{20Mg} + E_{exc}$, where E_{exc} is the energy of state to which ^{20}Mg is excited. From equation 3.1, the Q value for the above reaction is (taking c=1) :

$$Q = m_{^{20}Mg} + m_d - m_{d'} - (m_{^{20}Mg} + E_{exc}). \tag{3.3}$$

Here $m_d = m_{d'}$ because the ground state is the only bound state in the deuteron. Therefore, the above equation gives:

$$Q = -E_{exc} \tag{3.4}$$

hence measuring the Q value directly provides the excitation energy of ^{20}Mg.

3.2 Radioactive Ion Beam production at TRIUMF

Since ^{20}Mg is a short lived nucleus at the drip-line, it needs to be produced in the laboratory using RIB production methods discussed in Chapter 1. At TRIUMF, RIBs are produced using the Isotope separation on-line (ISOL) method. A primary proton beam is accelerated to 500 MeV using a cyclotron. This proton beam impinges on a SiC (silicon carbide) target. The interaction of the proton beam with the target produces a variety of fragments out of which many are radioactive nuclei which then effuse into an ion source. The rest frame half-life of ^{20}Mg is 90.8 milliseconds which poses a challenge to produce high intensity ^{20}Mg beam. A mass separator is used for selecting the desired isotope of interest. The mass separator separates elements based on mass-to-charge ratio and depending on the resolving power of a given mass separator sometimes contaminant isobar nuclei (i.e. having same mass) cannot be separated in the beam. In fact, this was the case for the present experiment where the beam had ^{20}Na as an isobaric contaminant. The identification of this contaminant in our experiment is described in the next chapter. The beam was accelerated to 8.5A MeV using a superconducting linear accelerator. This re-accelerated radioactive beam with a total energy of 170 MeV was then delivered to the experimental facility IRIS. The beam at these energies is still sub-relativistic (v/c $\sim$ 0.1). A schematic of various stages of beam production and acceleration is shown in Figure 3.1.

3.3 IRIS : A charged particle reaction spectroscopy station

The IRIS (ISAC Charged Particle Spectroscopy Station) facility is stationed in the ISAC-II experimental area at TRIUMF. The IRIS facility is designed to study the direct

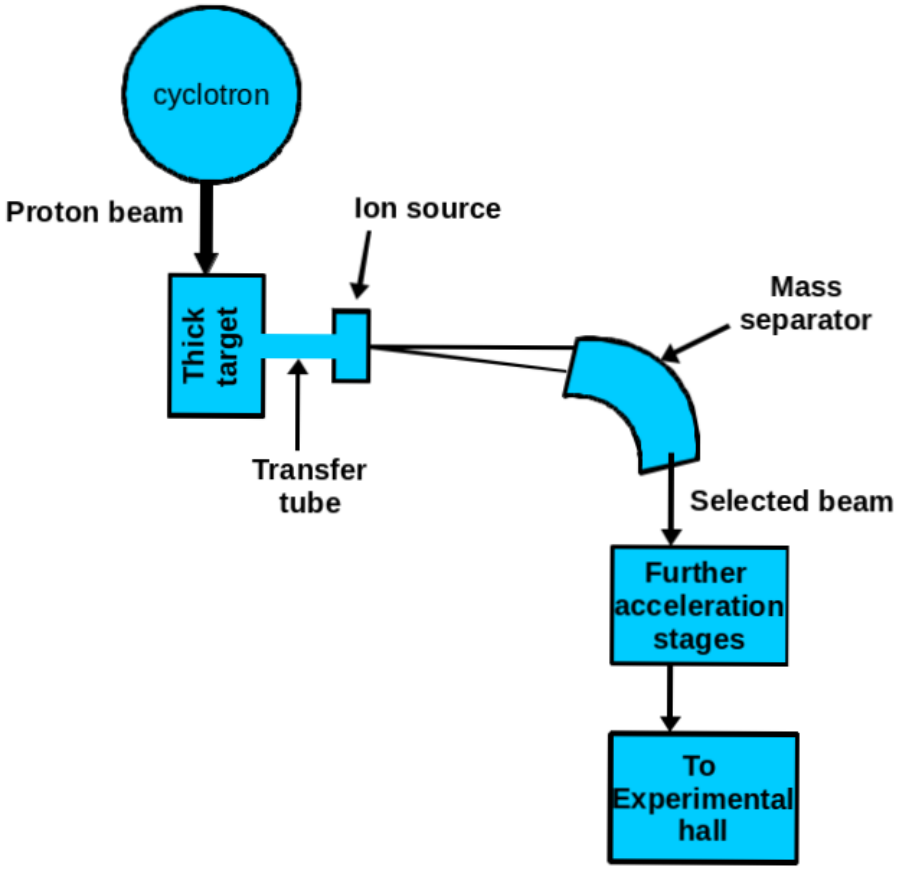

FIGURE 3.1: Schematic of the various stages production and re-acceleration of the ^{20}Mg radioactive beam to IRIS in the ISAC II experimental hall.

reactions such as inelastic scattering and transfer reactions in inverse kinematics using RIBs. The major focus of the IRIS facility is to detect the charged particle reaction products following the reactions of rare isotope beams with isotopes of hydrogen (H_2/D_2) as a target. The novel feature of IRIS is the use of a thin windowless solid H_2/D_2 target. The schematic of IRIS is shown in Figure 3.2. The major components of the IRIS facility are the Ionization Chamber (IC), the solid H_2/D_2 target, charged particle detectors for detecting reaction products and end detectors for detecting the unreacted beam. These components are discussed one by one in the subsequent sections.

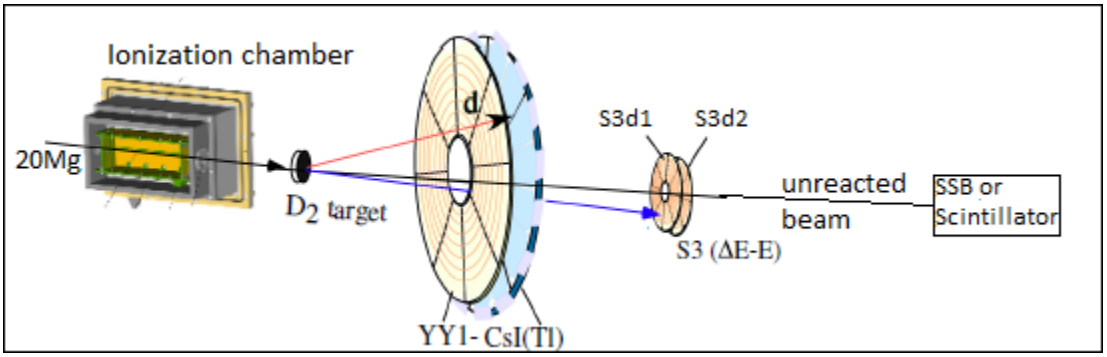

FIGURE 3.2: IRIS layout.

3.3.1 Ionization Chamber

The low-pressure ionization chamber (IC) at the IRIS facility is of paramount importance for identifying the isobaric contamination as well as for beam counting. It is placed upstream of the reaction target. The chamber is filled with isobutane gas at 5 to 20 Torr. The challenge in operating the ionization chamber at low pressure is to allow beam identification with minimal energy loss. The windows (which keeps gas volume separate from the vacuum) are made up of 50 nm Si_3N4 (silicon nitride) foils with dimensions of 10mm $\times$ 10mm (Kanungo, 2013). These thin windows, along with the low-pressure gas minimize the energy loss and straggling effects before the beam hits the target. The low pressure operation of IC allows minimal energy loss for an ion passing through it, however, it needs to have a signal to noise ratio high enough to determine individual events. The IRIS ionization chamber employs the field cage along with the co-planar anode. The field cage (FC), is a negatively charged cage made up of metal strips that run around the perimeter of the chamber. It creates an electric field gradient in the Ionization Chamber that drifts the electrons in the direction of the anode strip. The field cage uses eleven segmented metallic strips which run from the cathode to the coplanar anode. The cathode is at a negative potential with respect to the anode. This voltage is fed through each subsequent level of the field cage through a series of resistors. This creates an electric field gradient with decreasing negative potential approaching the

anode. The field cage helps in the transverse drift of electrons. The co-planar anodes create a local electric field that concentrates electrons on to the central anode strip (Fortier, 2013). The co-planar anodes are at less negative potential with respect to cathode. Figure 3.3a shows the rendering of the IC along with its diagnostic box flange. Figure 3.3b shows the cross-sectional diagram of the co-planar anodes surrounding the anode strip and the conceptual direction of the electric field lines.

3.3.2 Windowless solid H_2/D_2 target

The specialty of IRIS is the use of novel thin windowless solid H_2/D_2 target which makes the reactions with low-intensity beams of exotic nuclei possible. The use of a solid H_2/D_2 target is of paramount importance and has an advantage over other targets like liquid or gas H_2 targets or polyethylene foils. Firstly, the solid deuteron target will have a higher density of target atoms available for reactions compared of polyethylene foils of the same thickness. Therefore, solid H_2/D_2 can increase the reaction yield without compromising on the resolution. Secondly, the background scattering from carbon nuclei in polyethylene foils will not be present in the case of solid H_2/D_2 target.

The assembly of the solid H_2/D_2 target at IRIS is shown in Figure 3.4. The copper target cell has a hole of 5 mm in diameter. The cell is lined with a silver (Ag) foil of 5.4 μm thickness. This target cell is cooled to $\sim$ 4 K using a cryo-cooler with a helium compressor. This target cell has a cylindrical copper heat shield around it to minimize the radiative heating of the target. This shield is made of the oxygen free copper and is also cooled down to $\sim$ 24 - 27 K. Details of the heat shield geometry and geometric efficiency will be discussed in Chapter 4. Once the target cell and heat shield have reached their stable low temperatures, H_2/D_2 gas is sprayed using a diffuser on the surface of the Ag foil, which is used as a backing material. The diffuser has a diameter of 16 mm and gas flows through the fine porous surface of the diffuser which regulates the smooth flow allowing the hydrogen deposition diameter to be similar to

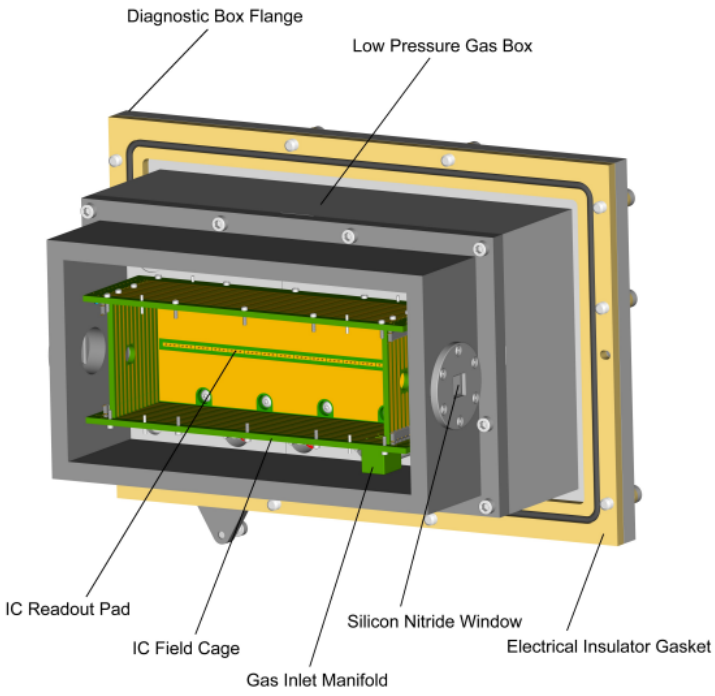

(a)

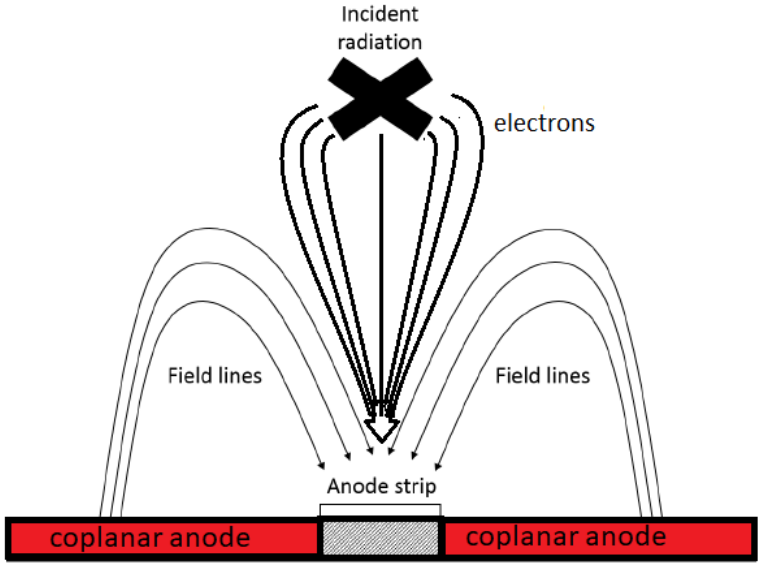

(b)

FIGURE 3.3: Ionization Chamber design and working (a) A layout of the IC attached to its diagnostic box flange (Sheffer, 2013) (b)cross-sectional diagram of the coplanar anode surrounding the anode strip shows the direction of the electric field lines (adapted from Fortier, 2013).

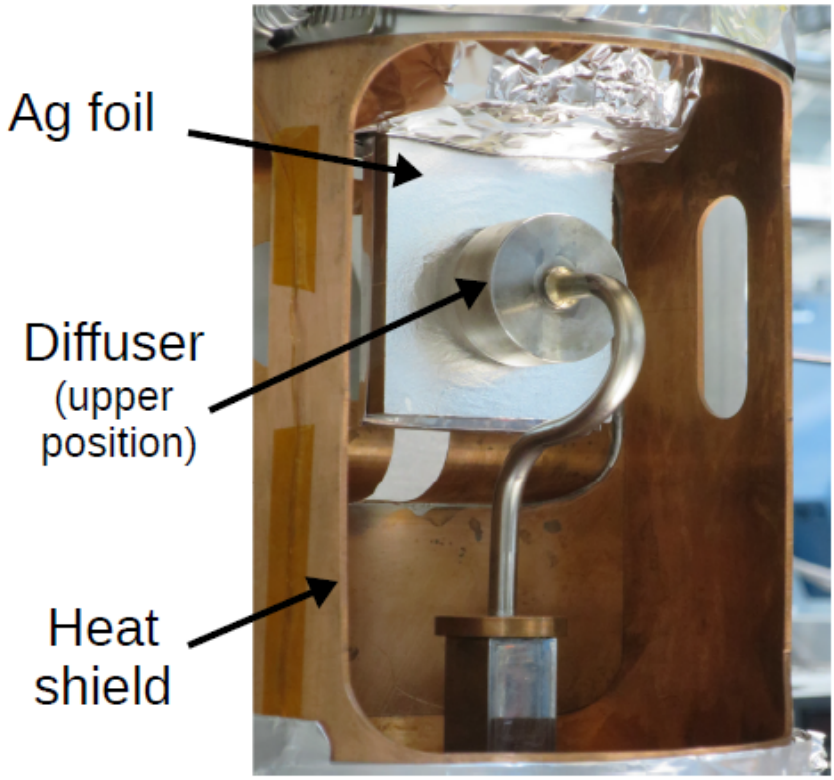

FIGURE 3.4: IRIS target assembly

the diffuser diameter. Using estimates of diffuser diameter along with other information and Boyle's law, the amount of H_2/D_2 gas needed to be supplied to form a target of particular thickness can be estimated. The diffuser is retracted from the beam line after the target formation.

The incoming ^{20}Mg beam hits the target, first interacting with the Ag foil and then enters the solid H_2/D_2 target where reactions of interest take place at any random point within the thickness of the D_2 target. The reaction products go through the remaining effective thickness of the target after the interaction point. The contribution from the background reactions due to the interaction of the beam with the Ag foil (e.g. fusion-evaporation reactions) can be separately measured using no D_2 data (i.e. beam hitting Ag foil only) and this leads to background subtraction during data analysis.

3.3.3 Charged particle detectors

The IRIS facility is well suited for detection of charged particle reaction products. The lighter target-like particles are detected through a set of thin and thick detectors serving as a $\Delta E - E$ telescope. The lighter particles pass through an array of 100 μm thick silicon strip detector, referred to here as YY1, which measures energy loss and the scattering angles of these particles. The array consists of eight azimuthal sectors, with each sector being segmented into sixteen rings (Figure 3.5). Depending on the position of the YY1 detector from the target center, each ring subtends a range of angles from θ_1 to θ_2. Scattering angles of all the particles (θ_C of equation 3.2) recorded within a ring is taken as the midpoint angle value of that ring, given by $\theta = \theta_1 + \theta_2$. Each ring subtends an angle less than 1.6 degrees in the laboratory frame. The angle bin used for angular distribution (see Chapter 4) is $\approx$2 degrees which is greater than this angle resolution . The YY1 detector is annular in shape with an inner and outer radius of 5.0 cm and 12.9 cm respectively. For the current experiment, the YY1 array was placed at a distance of 8.6 cm from the center of the target. Hence, it subtends laboratory angles from 30.1^o to 56.2^o. The coverage of angular ranges smaller then the detected angles (i.e. placing detector closer to the target) could lead to higher accumulated statistics based on theoretical differential cross sections alone, but the minimum detector distance from target is limited by heat shield around the target. The geometric efficiency also goes down target to detector distance decreases. Angular range in the current experiment was chosen to optimize the number of counts expected in these detectors. Each ring in each sector acts an independent detector, so total 8$\times$16 signals are read out from the YY1 detector array. The lighter particles that do not stop in the YY1 array and deposit their remaining energy in a detector array of 12 mm thick CsI(Tl) scintillator (Figure 3.6) detector placed directly behind the YY1 detector array. The 16 crystals of the CsI(Tl) detector array are arranged in the same azimuthal configuration as the YY1 array, and each of the YY1 sectors matches with two crystals of CsI(Tl) placed behind it. This

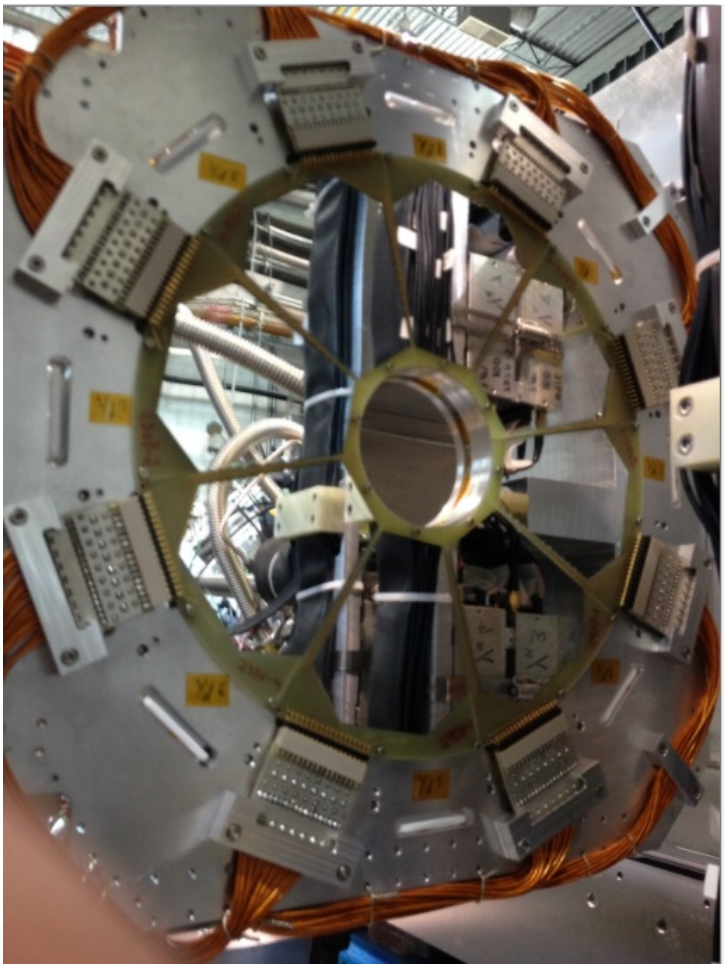

FIGURE 3.5: YY1 detector, a silicon strip detector for light target like particles.

combination of YY1 and CsI(Tl) detector therefore enables ΔE-E particle identification and is shown in Chapter 4. The energy and angular information of the scattered particles enable us to reconstruct the missing mass spectrum for obtaining the excitation energies of ^{20}Mg.

The heavier beam like particles scattered at very small angles pass through the annular aperture of the YY1 detector array and are detected further downstream in a pair of silicon detectors of S3-type. The first detector in the path of the particle is 60 μm thick and is referred to here as S3d1. This is followed by a thicker (500 μm) referred to here as S3d2. The combination of S3 detectors act as a ΔE-E telescope for heavier particles.

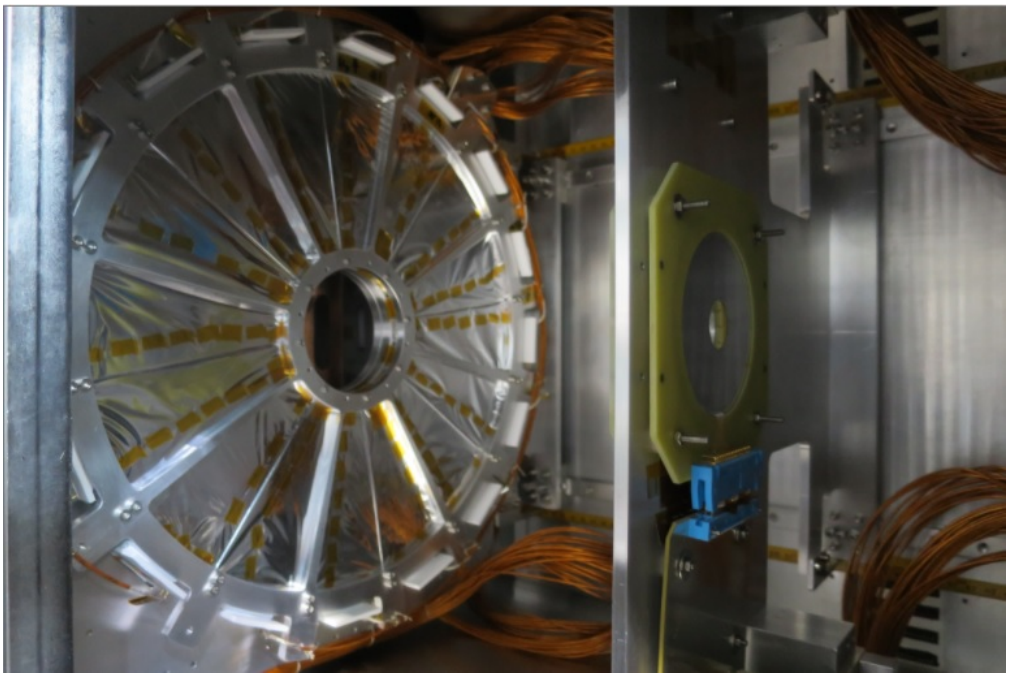

FIGURE 3.6: CsI(Tl) detector viewed from downstream.

Both the S3d1 and S3d2 detectors are double-sided strip detectors segmented in 24 rings on one side and in 32 sectors on the other side. The image of S3 detector viewed from downstream is shown in Fig 3.7. The S3 detectors have an annular configuration with inner and outer radii being 1.1 cm and 3.5 cm, respectively. For the current experiment, these detectors were placed at 33 cm from the center of the target covering laboratory angles from 1.9 degree to 6.1 degree.

3.3.4 End detectors for unreacted beam

Both sets of detectors discussed above are annular in shape therefore the unreacted beam passes through the hole in the center of these detectors. The beam is eventually stopped in a radiation hard YAP:Ce inorganic scintillator, read out by a photomultiplier tube. The ratio of beam counts in the ionization chamber, before the IRIS target, to the counts in beam-stopping scintillator in the last chamber helps to monitor the transmission ratio of the beam continuously during the experiment. This last vacuum chamber is also

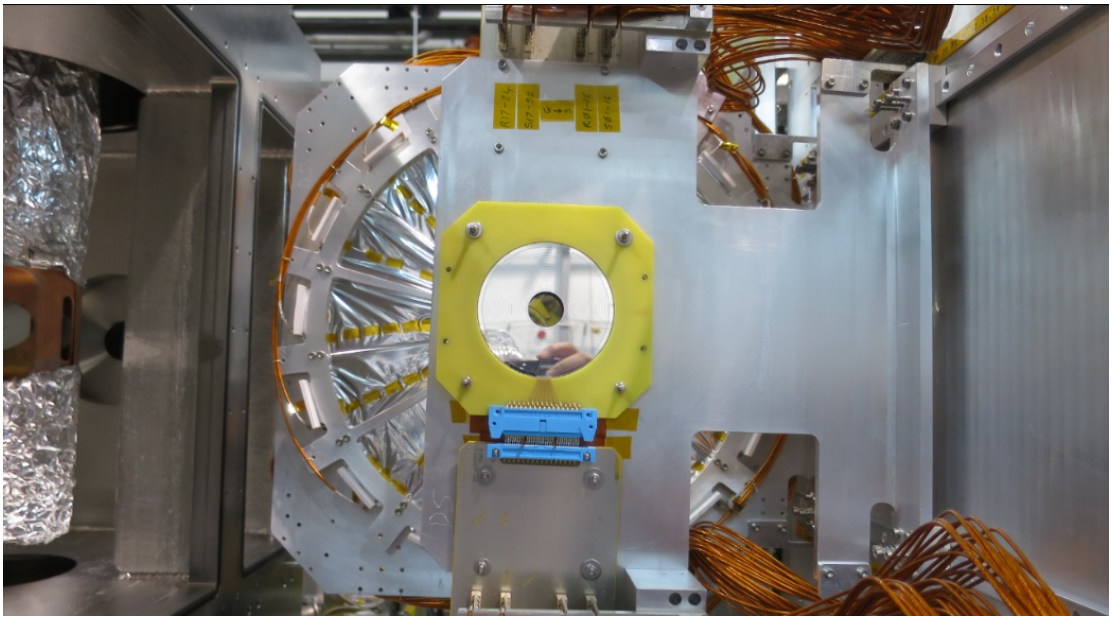

FIGURE 3.7: S3 detector as seen from downstream.

equipped with another zero degree silicon surface barrier (SSB) detector. Figure 3.8 shows an image of the SSB detector. This detector is inserted only intermittently just before the scintillator detector. The SSB detector measures the energy of the un-reacted beam. This beam energy measured after the D_2 target allows us to determine the target thickness from its difference compared to the energy measured without D_2. While this is only done intermittently, there is a continuous measurement of the target thickness from the energy measured using the S3 detectors, as described in chapter 4.

3.4 Signal processing

In this section, an overview of the electronic circuit and data acquisition used during this experiment is provided. The interaction of scattered charged particles inside the detector generates pairs of charge carriers (electron-hole pairs or electron-ion pairs depending on the type of detector). This charge is collected by applying an appropriate electric field in the detector volume and is converted into a voltage pulse. The amplitude of this signal

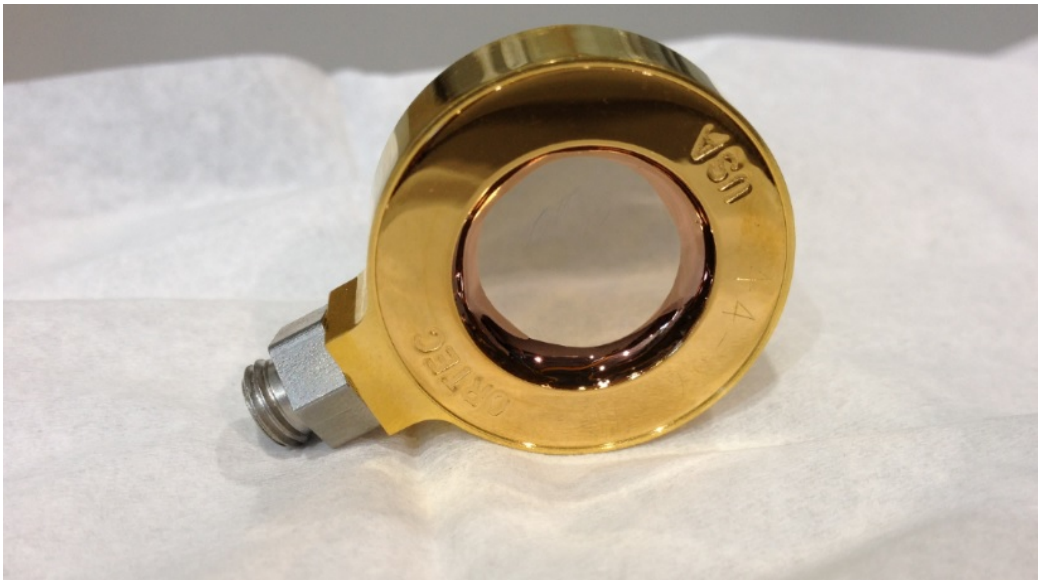

FIGURE 3.8: SSB detector.

pulse is proportional to the corresponding charge generated which in turn is proportional to the energy deposit of particle in the detector. Thus, the interaction of each quantum of radiation in the detector volume leads to a signal pulse. These pulses are processed and recorded by subsequent pulse processing electronic circuits. The individual pulse provides the energy information based on the amplitude of the voltage pulse. Therefore various elements are required at various stages to generate a meaningful signal out of the charge collected by the detectors. The first elements in the signal processing unit are preamplifiers. The aim of the preamplifier is to extract a voltage pulse from the charge collected in the detector. Most of the times, the amount of charge collected is minuscule and it not practical to deal with the signal pulses without intermediate amplification step provided by the preamplifiers. Preamplifiers used in our experiment are the charge sensitive type. In these preamplifiers, the output voltage is proportional to the total integrated charge in the input pulse. The shape of output voltage pulse from the preamplifier is shown in Figure 3.9 (using pulser input). The output pulse has sharp rise time and a slow decay time is dictated by the time constant of the RC circuit. The output of the preamplifier is sent to the shaping amplifiers for further amplification

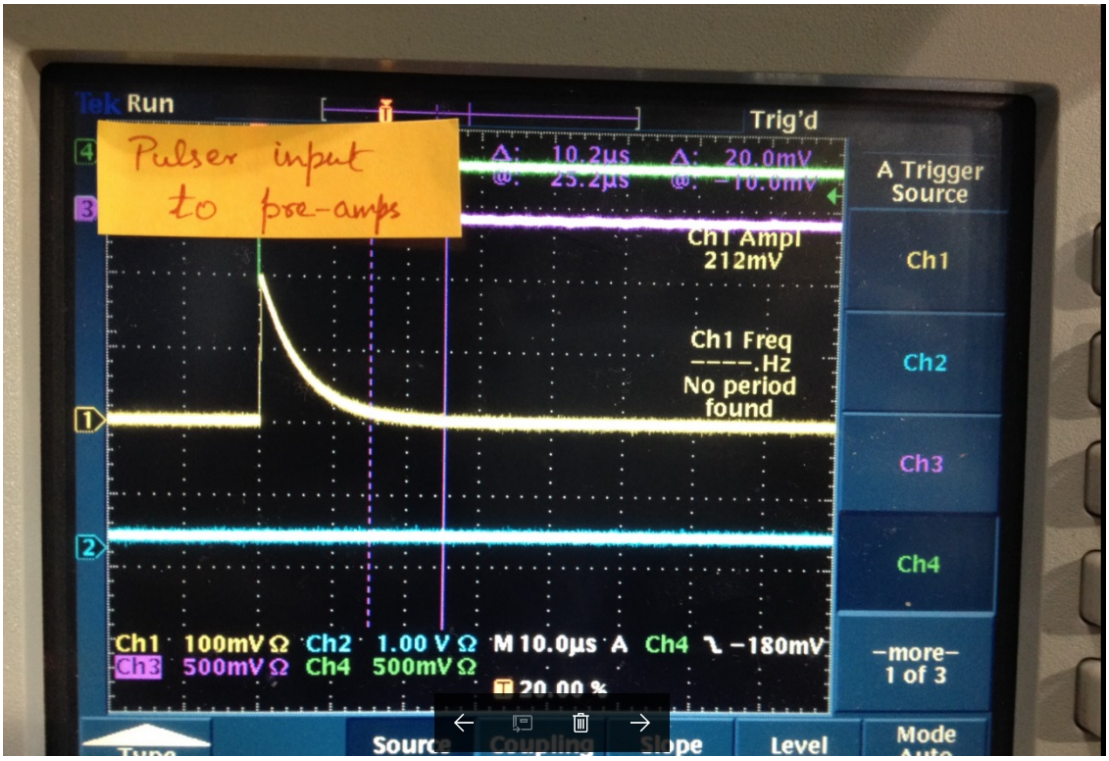

FIGURE 3.9: Preamplifier output using a pulser input.

and pulse shaping.

At IRIS, we use an MSCF-16 model which is a 16 channel shaping and timing amplifier as well as a leading edge discriminator. The MSCF-16 has a CR-RC^5 network which amplifies the signal and produces a Gaussian shaped output pulse. The pulse height of the Gaussian waveform provides energy information, therefore, this output is also referred to as energy output. The shaped pulse is then recorded by a peak sensing analog to digital converter (ADC). This unit converts the voltage amplitude of the shaping amplifier output into a digitized number which can be stored by the data acquisition computer. IRIS uses MADC-32 model for ADCs which are peak sensing ADCs. The ADCs were used with a resolution of 12 bits, which digitizes the voltage spectrum into 4096 channels. Each channel of the ADC therefore corresponds to a specific voltage and hence a specific energy. The function of the discriminator in the MSCF-16 unit is to

generate a logic pulse only if the input signal is above a specified voltage threshold. This logic pulse is used to generate the trigger and thresholds are specified in a way so as to reject the electronic noise. Figure 3.10 shows the noise levels for one channel of the each of YY1 detector and S3d1 detector. The thresholds were set to cut off this noise. The threshold levels should not be set too high because cutting off meaningful signal is highly undesirable. Therefore, the energy equivalent to thresholds was also obtained to have information on minimum accepted energy and thresholds were set to an optimized value. The average energy equivalent for YY1 threshold was around $\sim$ 180 keV. The major focus of this experiment is to detect the scattered particles. Therefore, the master trigger for the experiment was a logic-OR signal from all the 240 channels of the YY1 and S3 silicon detector arrays. This is called the free trigger. The data acquisition system (DAQ) takes a finite amount of time to process a signal. The free trigger, as well as information on the DAQ time, is used to generate a gate of a specific width and this gate signal is fed to ADCs enabling the ADCs to know when to start taking data and for how long. The ADC gate widths used for YY1 and IC were 3 μs and 2 μs, respectively. The detailed circuitry is shown in Figure 3.11.

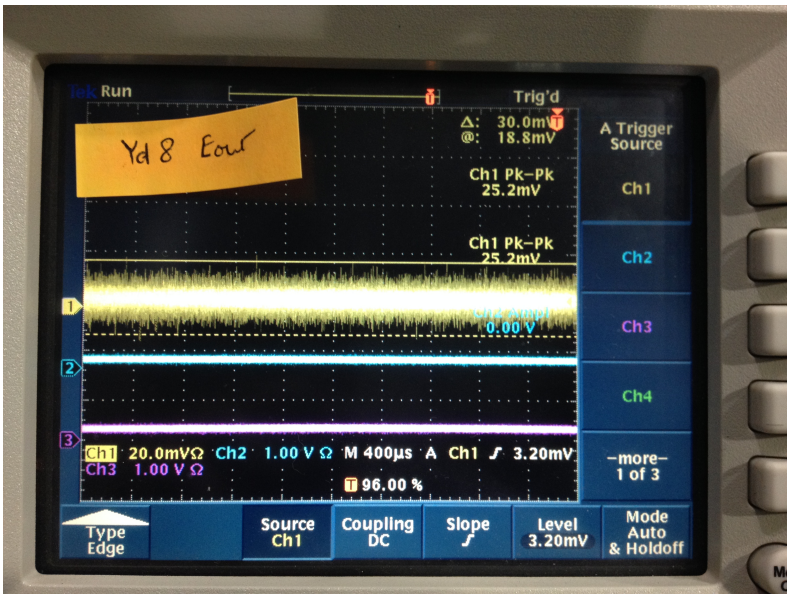

a

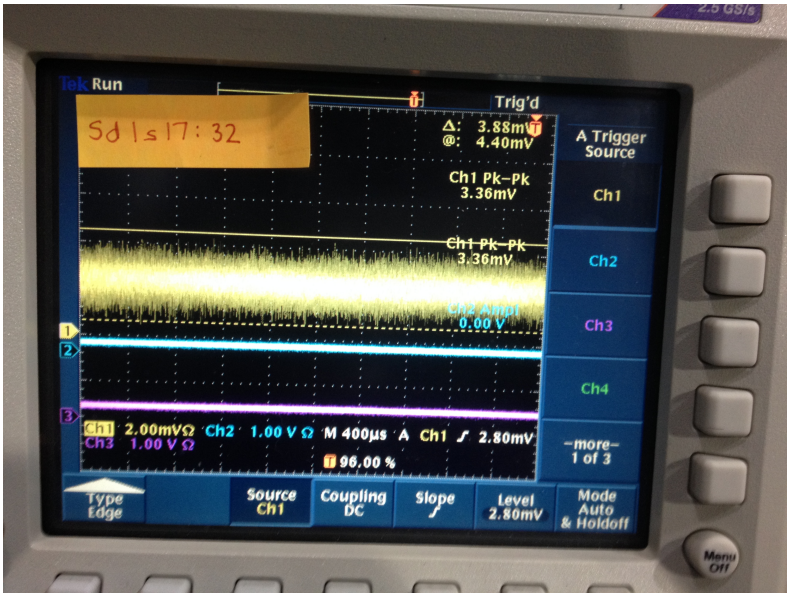

b

FIGURE 3.10: Electronic noise from (a) YY1 detector's channel (b) S3d1 detector's channel.

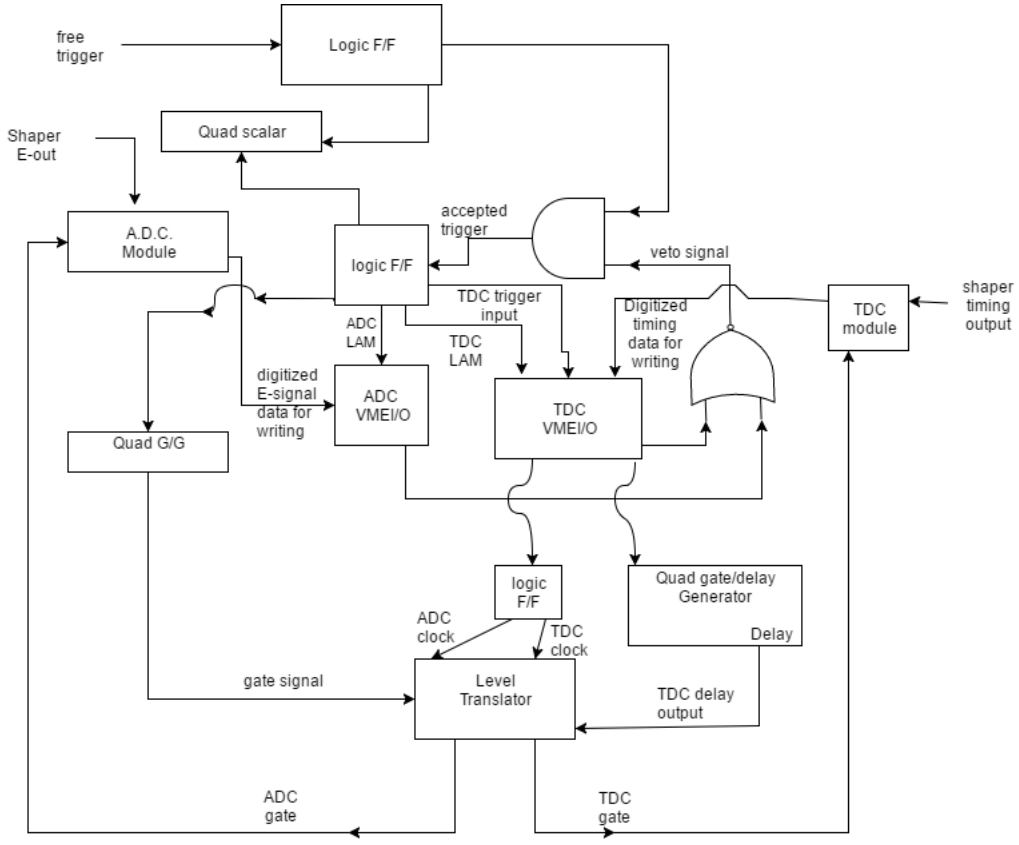

FIGURE 3.11: Circuit diagram.

Chapter 4

Data Analysis

This chapter describes the details of data analysis, as well as the details of the Monte Carlo simulations. Section 4.1 discuss the Monte Carlo simulations, and its application in optimizing the experimental setup, calculating detection efficiencies, and most importantly the estimation of background contribution due to the $^{20}\mathrm{Mg} + \mathrm{d} \rightarrow ^{18}\mathrm{Ne} + \mathrm{p} + \mathrm{p} + \mathrm{d}$ four body phase space. Section 4.2 describes the tagging of different isobars in the beam and incident beam counting. Section 4.3 describes the basic process of calibration and provides details of energy calibration of the detectors and determination of solid D_2 target thickness. Section 4.4 deals with particle identification. Section 4.5 provides details of construction of excitation spectrum for ^{20}Mg, estimation and subtraction of background contributions. It also discusses the determination of differential cross sections for the ground state and excited states.

4.1 Monte Carlo Simulations

The Monte Carlo simulation is an essential part of this dissertation as it played a vital role during various stages. Our aim is to simulate the experimental conditions.

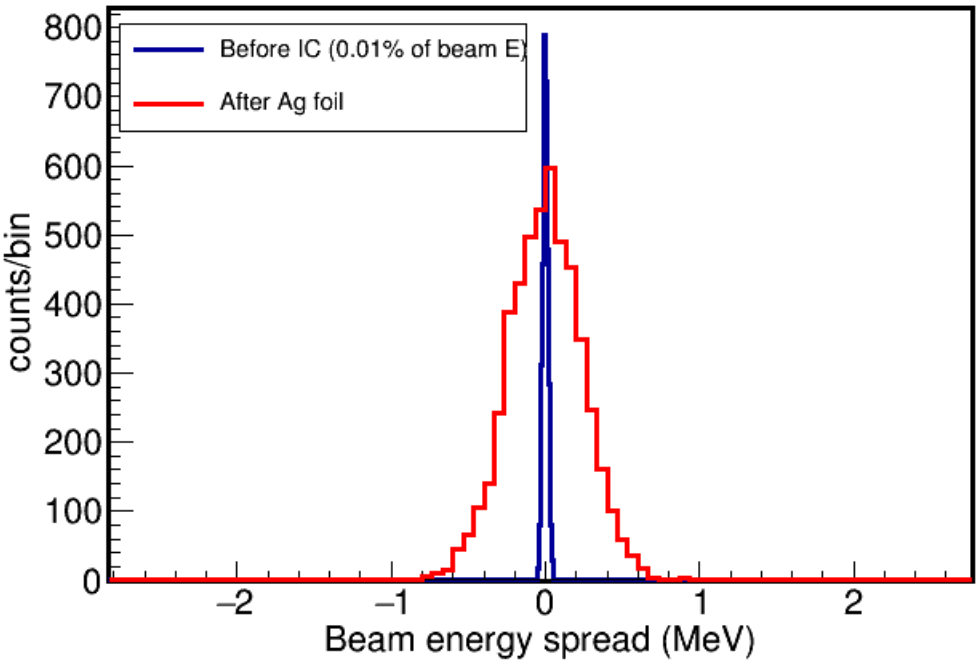

FIGURE 4.1: Spread in beam energy before the ionization chamber (blue) which was taken to be 0.01 % of the beam energy and after the Ag foil (red) due to energy straggling effects.

4.1.1 Simulating the beam particles and passage through IC

The simulation considers the beam on target with a Gaussian profile (in X and Y) with a standard deviation width of 2 mm. The beam events generated pass through the ionization chamber and subsequently through a 5.4 μm thick Ag foil where they undergo energy-loss, energy straggling and multiple Coulomb scattering. The energy broadening of the beam after the Ag foil has been shown in Figure 4.1, assuming an initial beam energy spread of 0.01% of the beam energy. Overall contribution of these effects to total excitation energy resolution is small (around sigma $\sim$ 70 keV) while major contributions to excitation energy resolution come from the target thickness effects.

4.1.2 Target thickness impact on resolution

As the beam particle enters the solid deuteron target, it can interact randomly at any location inside the target. Therefore, the interaction point for each beam particle inside the target was selected by sampling a uniform random distribution. The impact of target thickness on the resolution of excitation spectrum needs to be discussed in conjunction with the angular resolution. The reason being that the angles of scattered particles is measured based on the average value of the angle subtended by a given strip(ring) of the silicon detector. However, it is possible that two scattered particles have same scattering angle but depending on their point of interaction inside the target they might hit two different rings and hence the measured scattering angle will be different. This leads to a spread in energy for a given angle and hence contributes to the final resolution. This discussion explains that, to analyze the impact of target thickness on the excitation spectrum, we need to have a proper implementation of detector's energy and angular resolution in our simulation. The energy resolution of the YY1 detector was 0.23 % (σ) at 5.7 MeV, as obtained from triple-alpha source data. The energy resolution of the CsI(Tl) scintillator was 3.1 %(σ) at 14 MeV, determined from elastic scattering data. The angular resolution comes from the finite strip width for each ring. To determine the target thickness effect on the excitation spectrum resolution, the first contribution comes from random interaction point inside the target; leading to a different interaction energy for each beam particle and different kinematics for each event. Depending on the interaction point, the reactant products have to traverse different path lengths inside the remaining target, again leading to different energy losses. Finally, two scattered particles scattering at the same angle but different positions inside the target could deposit energy at two separate angles as the measurement of the angle is based on finite strip size. The excitation spectrum resolution, for three different target thicknesses, is shown in Figure 4.2.

This figure shows that the excitation resolution is better for the higher laboratory angles.

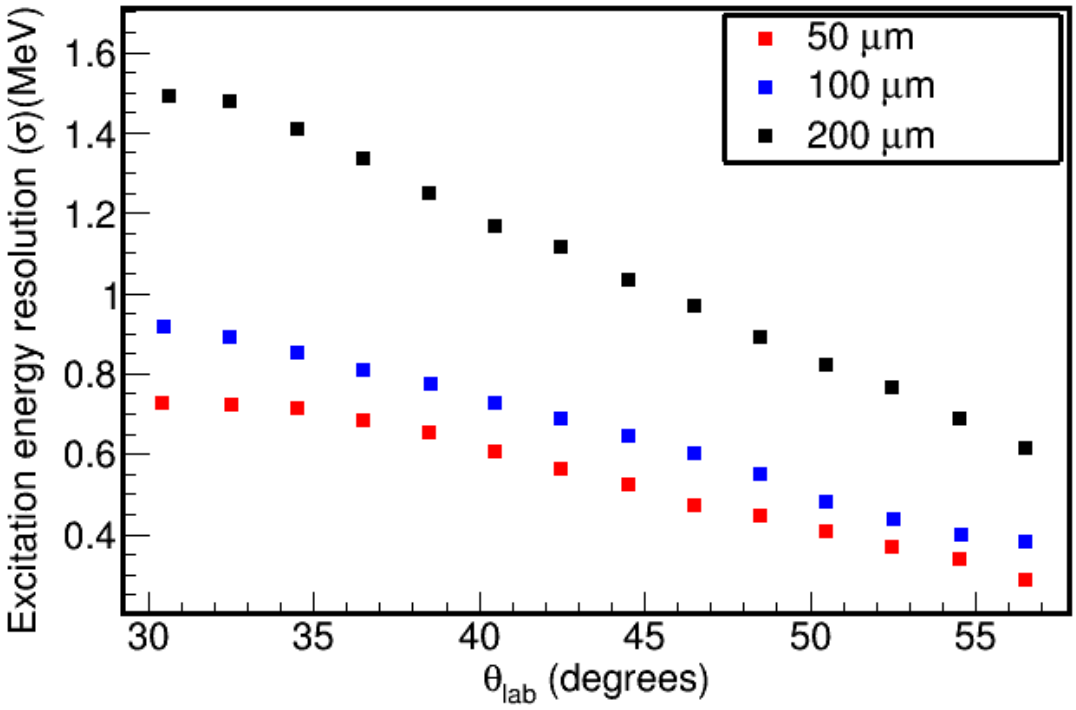

FIGURE 4.2: Resolution (σ) of excitation spectrum as function of laboratory angle, calculated for three different target thicknesses.

For smaller laboratory angles the difference in excitation energy resolution between 200 μm and 100 μm thick targets is around 500 keV(σ). In our experiment, we adopted a D_2 target with average thickness 60 μm. This was an optimal choice based on the measurable statistics and necessary resolution.

4.1.3 Detectors and heat shield

The geometries and specifications of various detectors are explained in Chapter 3. Depending on the detector geometries and distance from the target, the hit pattern on the YY1 detector was simulated. Figure 4.3a (blue events) shows the simulated hit pattern for the entire YY1 detector. We also need to take into account the geometric efficiency.

Depending on the distance from the target, a part of the YY1 detector is masked by the heat shield. The heat shield is curved into a cylindrical form with the y-symmetry axis around the target cell. It has an outer diameter of 129 mm and a total length of 502.5 mm. This heat shield has a vertical opening of 50 mm above the center of the target cell and 111.7 mm below the center of the target cell. This gives opening angles of +39 degrees and - 60 degrees in the vertical direction. The horizontal opening angle is $\pm 60^0$. The simulated hit pattern for the YY1 detector, taking into account the masking effect due to heat shield, is shown in Figure 4.3 a (black). The overall detection efficiency from the geometric acceptance for each ring is shown in Figure 4.3b. The efficiency decreases as we move towards higher ring number (i.e. larger laboratory angles) because of the combined effect of smaller areas of the strips, as well as masking by the heat shield for some sectors.

4.1.4 Four Body Phase space

The reaction of interest for the current study is ^{20}Mg(d, d$'$)^{20}Mg*. The other reaction channels that are open at this energy are ^{20}Mg(d,p)^{21}Mg, ^{20}Mg(d,^{3}He)^{19}Na and ^{20}Mg(d,^{4}He)^{18}Ne. The detectors for the lighter particles will register various types of lighter elements, e.g. p, d, ^{3}He, ^{4}He. Therefore we need to separate deuterons from other lighter particles to study the ^{20}Mg(d, d$'$)^{20}Mg* channel. The particle identification is made using the ΔE-E telescope (YY1-CsI(Tl) detectors) and will be illustrated in detail in Section 4.4. However, even when deuterons are identified, the ^{20}Mg(d,d')^{20}Mg* is not the only source of deuterons. The other plausible sources of deuterons are reactions of ^{20}Mg on the Ag foil (e.g. fusion-evaporation reactions) and non-resonant background from four body phase space of ^{20}Mg+d $\rightarrow ^{18}$Ne +d +p+p. The background from Ag foil can be measured by collecting data with no D_2 present (i.e. ^{20}Mg impinging on Ag foil only). The estimation of background from the reactions on Ag-foil will be discussed in Section 4.5.

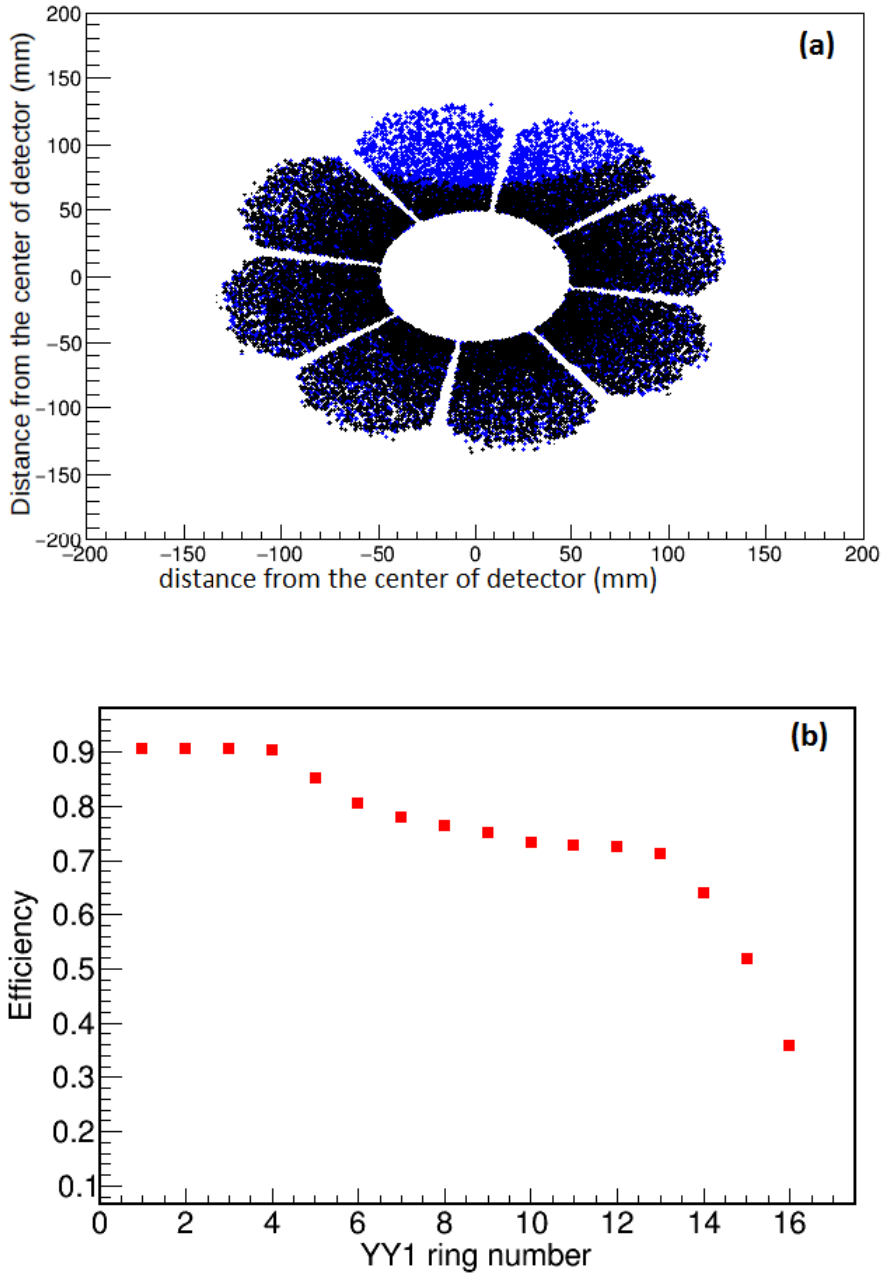

FIGURE 4.3: (a) Simulated YY1 hit pattern with (black) and without (blue) accounting for masking by the heat shield. (b) Geometric efficiency of the YY1 detector array.

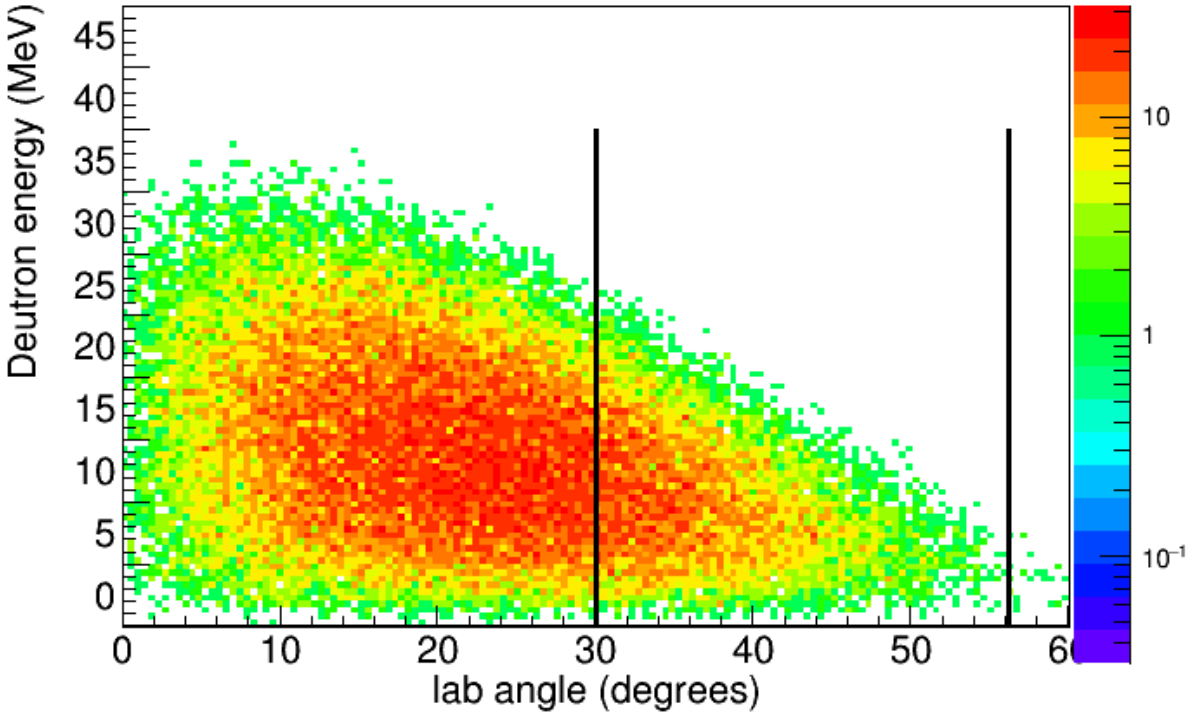

FIGURE 4.4: Simulated phasespace for deuteron from ^{20}Mg+d $\rightarrow$^{18}Ne +d +p+p. The vertical black lines show the laboratory angle coverage for this experiment.

The contribution from the four body phase space was evaluated from the simulation. We simulated the non-resonant background from the four body phase space of ^{20}Mg+d $\rightarrow$d+^{18}Ne+p+p considering isotropic emission of the products in the center-of-mass (CM) frame. There are four products in the exit channel, and all these products can share the available phase space in different ways. The kinematics of the process was simulated using 'TGenPhasespace', a utility class in ROOT (data analysis framework by CERN), which allows the user to generate an n-body event. The decay of a particle defined as a Lorentz four-momentum into n-bodies can be simulated. Here our initial four-vector is the sum of four-momentum for beam and target:

$$P_{\text{initial}} = P_{\text{beam}} + P_{\text{target}} \rightarrow p_{^{18}\text{Ne}} + p_{\text{d}} + p_{\text{p}} + p_{\text{p}} \tag{4.1}$$

where P_{beam} and P_{target} are four-momenta for the beam and the target, respectively, and $p_{^{18}Ne}$, p_d, p_p are four vectors representing ^{18}Ne, deuteron and proton respectively. The simulated phase space for deuterons in this channel is shown in Figure 4.4. For proper subtraction of phase space contribution from the total excitation energy spectrum, proper normalization of this simulated background channel spectrum is required. The contribution of phase space to the excitation spectrum with the normalization will be presented in Section 4.5.

4.2 Beam identification and counting

The ionization chamber (IC) is placed upstream of the IRIS target system, and it serves two purposes. First, it helps identify the beam particles based on their atomic number (through energy loss). Second, it serves in counting the number of incident beam particles which is required to measure the cross sections as well as for other normalization purposes.

4.2.1 Beam identification

In this experiment, the ^{20}Mg beam contains ^{20}Na as an impurity, and it is important to identify the contaminant. The beam at 170 MeV energy loses energy in the IC which contains isobutane gas operated at 19.5 Torr pressure. The stopping power of a charged particle passing through matter, which is defined as energy loss per unit length, can be written as

$$-\frac{dE}{dx} \propto \frac{Z^2}{v^2} \tag{4.2}$$

where v and Z are velocity and atomic number of the charged particle, respectively. ^{20}Mg has higher atomic number than ^{20}Na and hence loses more energy in the ionization chamber. The ADC spectrum of the ionization chamber is shown in Figure 4.5. The

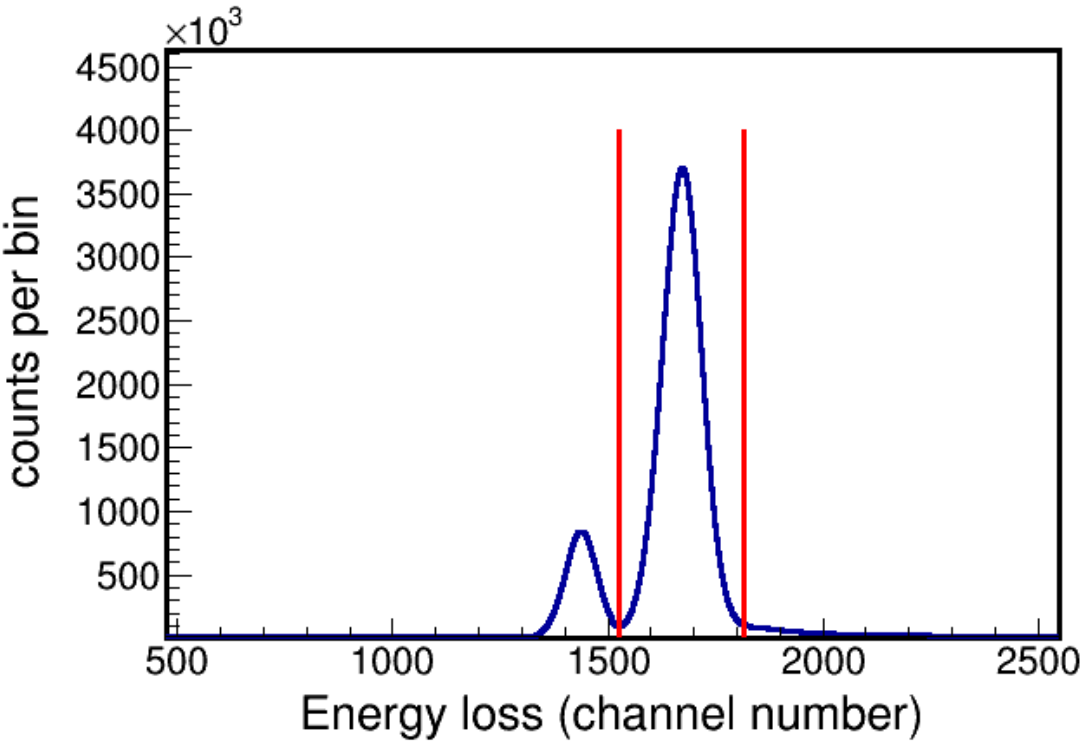

FIGURE 4.5: ADC spectrum of ionization chamber. Red vertical lines represent the 3σ selection region for ^{20}Mg.

spectrum shows two peaks corresponding to ^{20}Mg and ^{20}Na. As ^{20}Mg loses more energy, it appears at a higher channel number compared to ^{20}Na. From this spectrum, we have selected the events corresponding to ^{20}Mg. Vertical lines in Figure 4.5 shows the 3σ selection region for ^{20}Mg. The selected events have less than 1.3% contamination of ^{20}Na, as only tail region outside the 2.5σ region of ^{20}Na lies under the selected 3σ region for ^{20}Mg beam.

4.2.2 Incident beam counting

Once the beam particles are identified, it is important to count the number of incident ^{20}Mg beam particles. For this, the information recorded in the IC scalar was used. As

defined in the previous section, the beam contains isobaric contamination. Therefore, the total scalar counts represent both ^{20}Mg and ^{20}Na beam particles. Therefore, we estimated the ratio of ^{20}Mg beam particles to total beam particles - i.e. the ratio of the integral under the 3σ region (shown in Figure 4.5) to the total beam counts in the IC ADC spectrum. This ratio was determined continuously during the experiment and the respective scalar counts were scaled with this ratio. The other factor to be included to get the proper beam count is the data acquisition (DAQ) live time (τ_{live}). As described in Chapter 3, the trigger was an OR of all the silicon detectors. The DAQ system cannot record all the events because of the finite time required to process and store the events. Therefore, the scalar counts should be corrected for DAQ live-time, which is the ratio of the accepted trigger to the free trigger. Based on this discussion, for the ith data recording period (run number) the effective number of incident ^{20}Mg beam particles can be written as

$$\mathrm{N_i}^{^{20}\mathrm{Mg}} = \mathrm{N_i^{scalar}} \times (\tau_{\mathrm{live}})_{\mathrm{i}} \times \frac{\mathrm{N_i^{ADC(^{20}Mg)}}}{\mathrm{N_i^{ADC(total)}}} \tag{4.3}$$

where $\mathrm{N_i^{scalar}}$ is the IC scalar counts, $\mathrm{N_i^{ADC(^{20}Mg)}}$ is the integral counts under the ^{20}Mg peak in IC ADC spectrum and $\mathrm{N_i^{ADC(total)}}$ is the total counts from IC ADC spectrum. Figure 4.6a, b & c show the IC scalar counts, DAQ live-time and ratio of ^{20}Mg to total counts in IC ADC spectrum respectively, for each data recording period over the entire duration.

4.3 Calibration of detectors and target thickness determination

This section describes the process of the energy calibration of the various detectors at IRIS. The process of calibration involves converting the channels of Analog to Digital Converters (ADCs) into a physical quantity, i.e. energy. The channel number is related

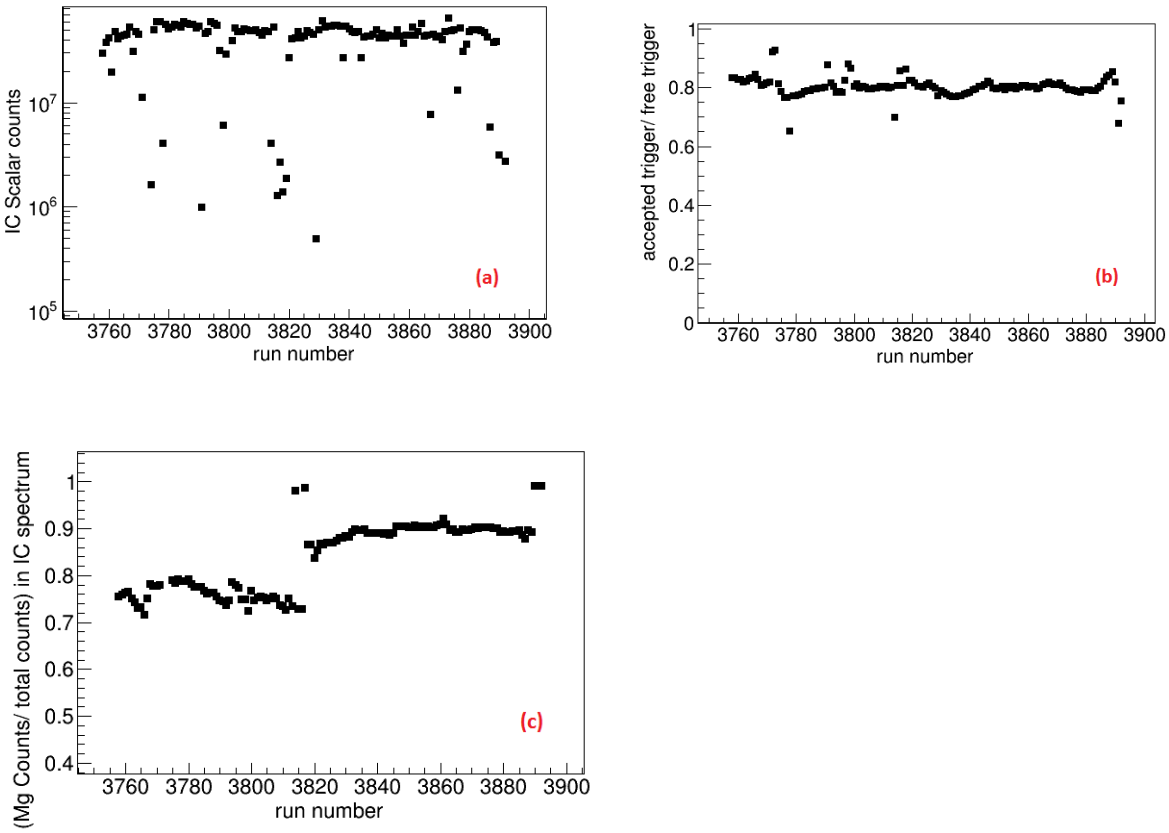

FIGURE 4.6: (a) IC scalar counts. (b) DAQ live time. (c) Ratio of ^{20}Mg to total counts in IC ADC spectrum. In all these figures x-axis represents the data recording period (run number).

to energy by the following linear relationship

$$E = g \times (c - p) \tag{4.4}$$

where E is the energy deposited by the incident ion, c is channel number of the ADC which records the event, g is the gain (i.e. conversion factor from channel number to energy), and p is the pedestal which is the channel offset corresponding to zero energy. The pedestal is measured by collecting data without an incident ion. The gain (MeV/channel) is determined by collecting data with an ion of known energy. In the

following, we first describe the process of calibrating the YY1 detector. The calibration of the S3 detector is required to determine the target thickness. We calibrated the S3 detector and explained the target thickness determination. At the end of this section, CsI(Tl) detector's calibration process is shown which requires the information on target thickness.

4.3.1 Energy calibration of the YY1 silicon detector

To calibrate the YY1 detector, we use a standard triple-alpha source placed in front of the YY1 detector. The alpha source used in the experiment contained the radioactive isotopes of ^{239}Pu, ^{241}Am and ^{244}Cm which emits alpha particles of 5.155 MeV, 5.486 MeV and 5.805 respectively, corresponding to the highest branching ratio. The alpha particles traverse through the dead layers of YY1 where they lose a small amount of energy, and the rest of the energy is deposited in the active silicon.

The thickness of dead layers is known, and total energy deposited in the active silicon was calculated using energy loss tables for three energies with highest branching ratios. The spectrum of the triple alpha source for one detector out of 128 detectors is shown in Figure 4.7. The three highest peaks were found using the peak finding algorithm in ROOT. Each peak was fitted by a Gaussian function and the mean value of the fitting function was used as the peak position. The peak position for three peaks gives us the channel number. Since the energies corresponding to each of these channel numbers are known, we found the gain by performing the least square linear fit using the standard calibration Equation 4.4. Figure 4.8 shows the least square fitting to three data points for one detector. Energy lose by deuterons in YY1 detector from ^{20}Mg(d, d$'$) reaction ranges from 0.2 MeV to $\sim$ 5 MeV. A similar procedure was repeated for all the 128 detectors.

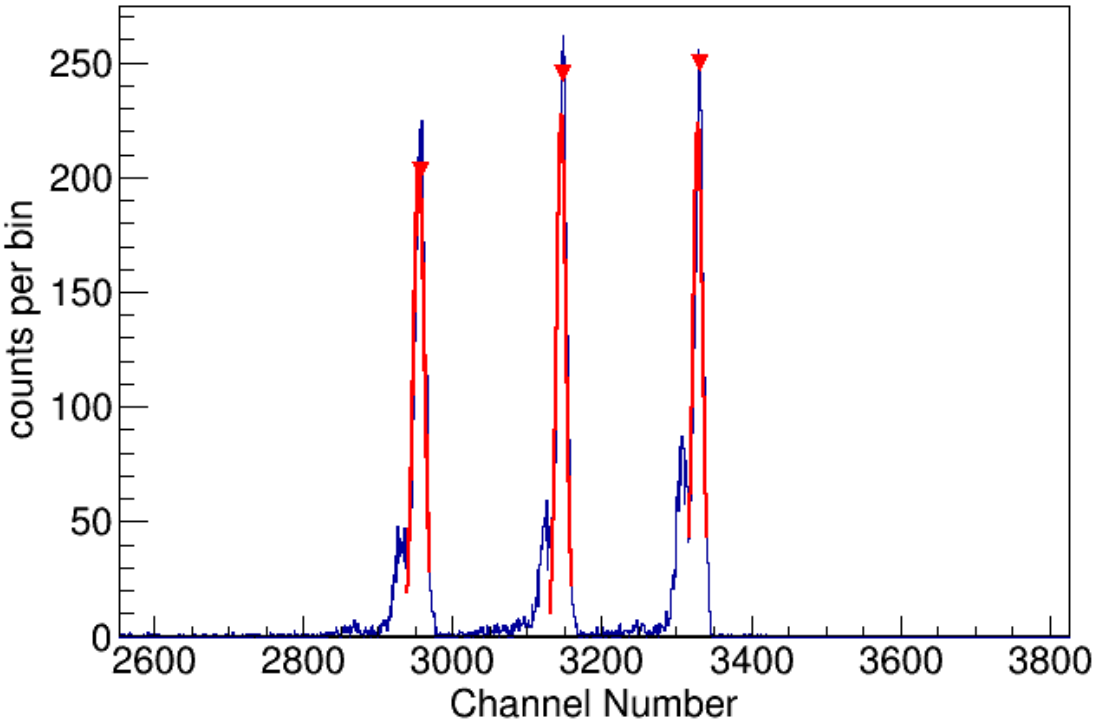

FIGURE 4.7: YY1 spectrum for triple alpha source for one detector out of 128 detectors.

4.3.2 Energy calibration of S3 detector

In this section, the energy calibration of the S3d1 and S3d2 detectors is described. For the purposes of this detector calibration (and for DAQ setup), a stable beam of ^{20}Ne was used. To calibrate the S3 detectors, we used the scattering of ^{20}Ne from Ag foil in the absence of solid D_2 target. The scattered ^{20}Ne deposits part of its energy in the S3d1 detector and the remaining energy in the S3d2 detector. The beam loses energy also in the dead layers on both sides of each S3 detector. For each of these detectors, the ADC spectrum shows the peak corresponding to the scattered ^{20}Ne (see Figure 4.9) for the first and last ring. The Gaussian fitting of the peak provided the channel number corresponding to the peak position. The peak energy was obtained for each ring using kinematic calculations and taking into account energy loss in dead-layers. The pedestal

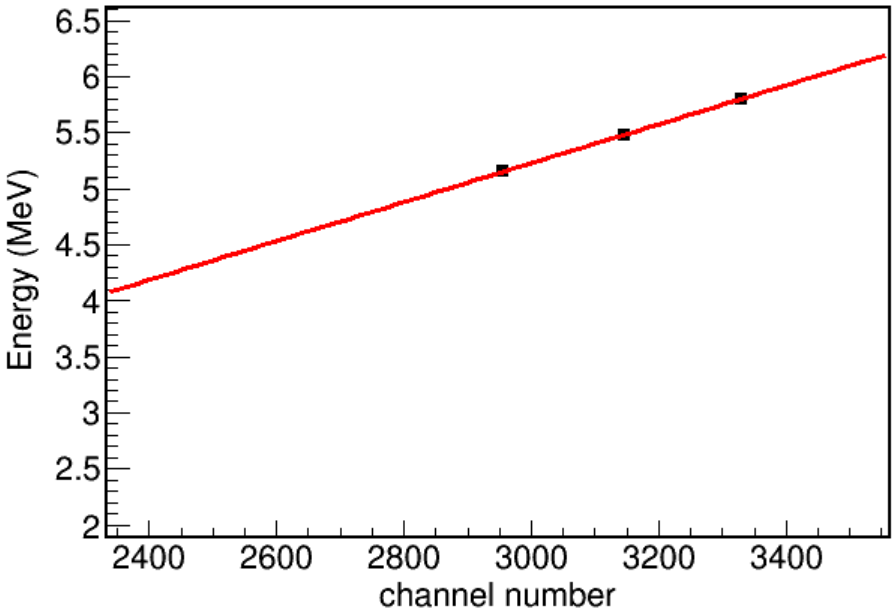

FIGURE 4.8: Least square fit using the calibration equation, for YY1 detector.

peak was recorded with data collected without ^{20}Ne beam. The gain was then obtained using Equation 4.4 .

The calibrated energy versus scattering angle plots for ^{20}Ne scattering from the Ag foil for the Sd31 and S3d2 detectors are plotted, and the calculated kinematic curves are compared to the calibrated data (Figure 4.10a, b). The calibrated data and calculated kinematic curves show good agreement over the range of detected laboratory angles.

4.3.3 Determining the target thickness

In Section 3.3.2, we discussed the formation of solid D_2 target. Information on target thickness is required for calibration of the CsI(Tl) detector for reasons that will become clear in the next section. Here I present the process of determining the target thickness using ^{20}Ne data, as this data will also be used to calibrate the CsI(Tl) detector. A

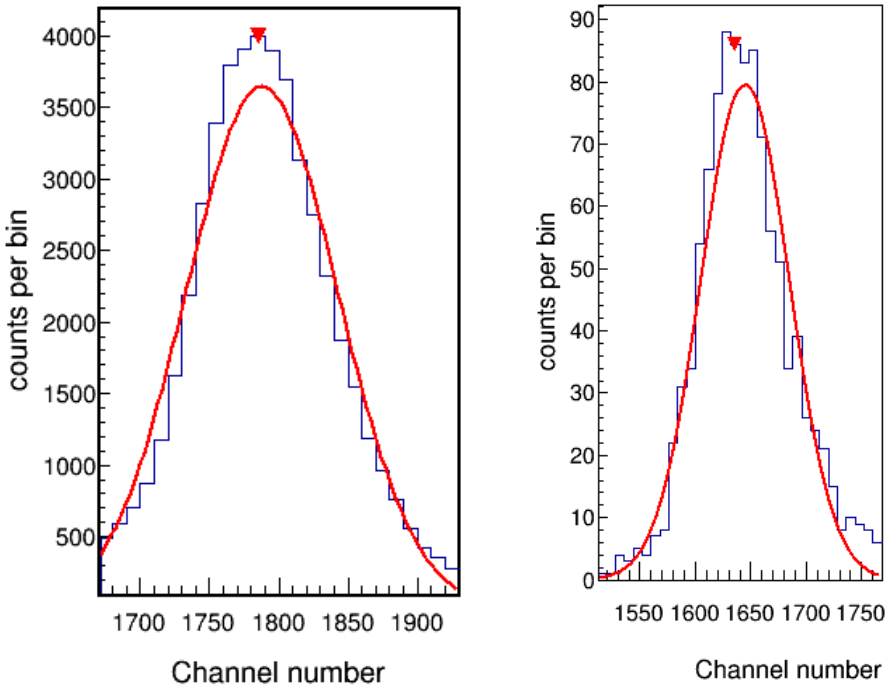

FIGURE 4.9: Energy spectrum for S3 detector, fitted with Gaussian function.

similar process was used to extract the target thickness for the ^{20}Mg data too.

To evaluate the target thickness, we have used the elastic scattering of ^{20}Ne from the Ag foil, i.e. ^{20}Ne(^{109}Ag,^{109}Ag)^{20}Ne with and without the solid D_2 target. The energy of ^{20}Ne measured after the D_2 target allows us to determine the target thickness from its difference compared to the energy of ^{20}Ne measured without D_2. The solid D_2 target thickness can be found using the stopping power calculation if the ^{20}Ne energy before and after the target is known. Let us denote the ^{20}Ne energy without the D_2 target by E_i and energy measured after the D_2 target by E_f. Target thickness can then be determined using following relation:

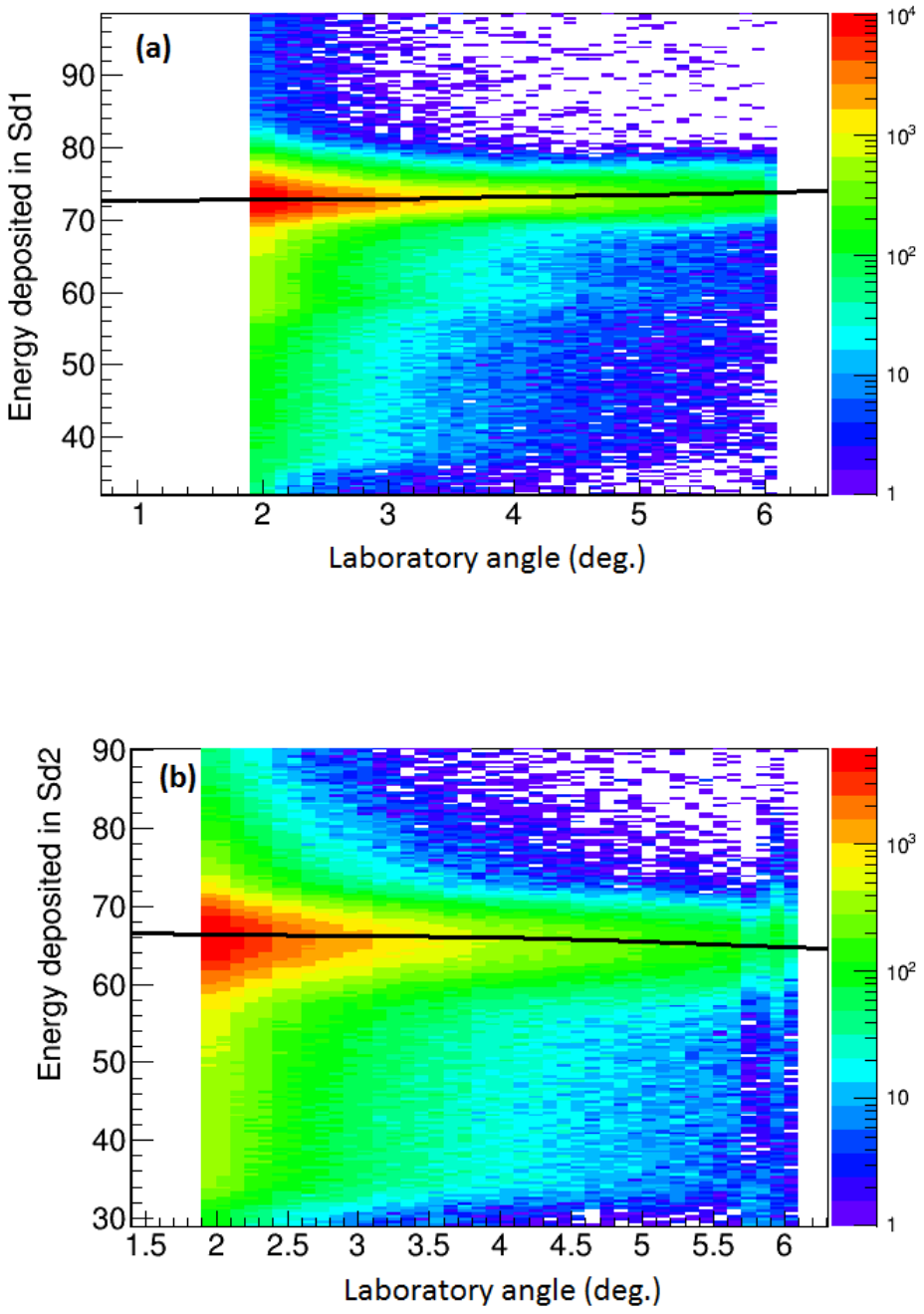

FIGURE 4.10: (a) Calibrated S3d1 (rings) energy versus θ_{lab}, black line is the calculated kinematic curve. (b) Calibrated S3d2 (rings) energy versus θ_{lab}, black line is the calculated kinematic curve.

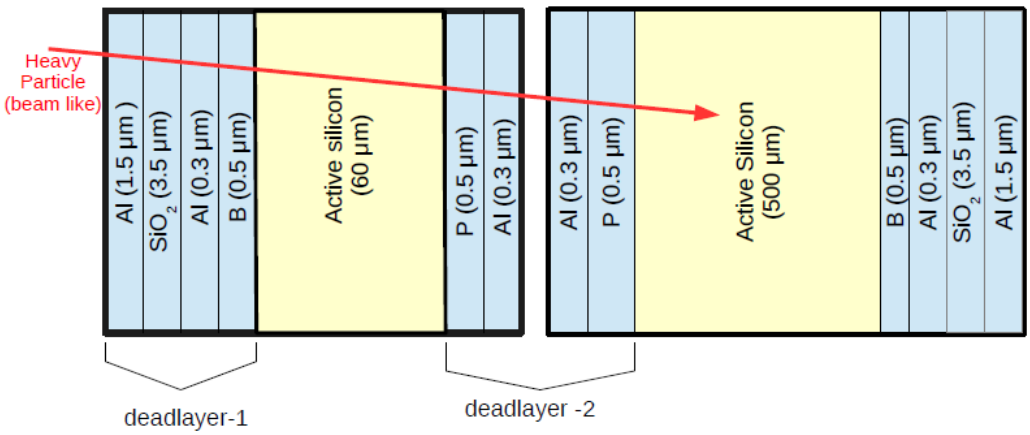

FIGURE 4.11: S3 detector and deadlayers used for target thickness determination.

$$t = \int_{E_i}^{E_f} \frac{1}{S(E)} dE \tag{4.5}$$

Where t is the target thickness, $S(E)$ is the stopping power of beam particle passing through solid D_2 target given by $-dE/dx$. E_i and E_f can be obtained by reconstructing the energy of ^{20}Ne (from the measured total energy in S3) before it enters the S3 detector, from the data without and with D_2 target respectively. The scattered ^{20}Ne passes through the ring-side dead layers of S3d1, loses energy in the active silicon of S3d1 detector, then passes through the sector side deadlayers of S3d1 and S3d2 and deposits the remaining energy in the active silicon of the S3d2 detectors. The trajectory of a scattered particle through various parts of the S3 detector is shown in the Figure 4.11.

The energy E_i (i.e. reconstructed energy before the particle enters the S3 detector) can be written as:

$$E_i = E_{S3d2} + E_{deadlayer2} + E_{S3d1} + E_{deadlayer1} \tag{4.6}$$

here E_{S3d2} is energy deposited in active silicon of S3d2, $E_{deadlayer2}$, E_{S3d1} and $E_{deadlayer2}$ denotes energy losses in deadlayer-2, active silicon of S3d1 and dead layer-1 respectively.

Similarly, E_f can also be obtained from data when the D_2 target is present. Once energy E_i and E_f are known, target thickness is found using relation 4.5. The reconstructed energies for ^{20}Ne from the S3 detector are shown in Figure 4.14. The mean values of the Gaussian fits to these peaks in Figure 4.12 represent energy before and after the D_2 target, hence gives energy loss inside the target which is used to calculate the target thickness. The target thickness obtained through this method for ^{20}Ne data is shown in Figure 4.13. A similar process was repeated for ^{20}Mg data, where the energy of ^{20}Mg scattering from the Ag foil with and without D_2 target was used. Figure 4.14 shows the run by run target thickness for ^{20}Mg data. The sinusoidal variation in target thickness arises from the temperature variation during day and night. The variation in temperature causes a change in the density of gas in the IC which leads to a change in energy loss. The variation of ambient temperature recorded using thermocouples has been observed to be consistent with this behaviour. In both target thickness plots, for ^{20}Ne and ^{20}Mg, the error bars represent a 5% uncertainty assigned from the variations in different energy loss tables.

4.3.4 Calibration of CsI(Tl) detector

The ^{20}Ne beam passes through the ionization chamber, Ag foil, and enters the solid D_2 target where scattering takes place at a random interaction point within the target. The scattered deuterons lose energy in the remaining target thickness after the interaction point, in the YY1 detector, in the mylar foil wraping layer of the CsI(Tl) detector and finally deposits remaining energy in the CsI(Tl) detector. Prior to the calibration of CsI(Tl) detector, the plot of ADC channel number versus laboratory scattering angle (i.e. kinematic plots) can be obtained for a given excited state in ^{20}Ne and for each sector of the CsI(Tl) detector.

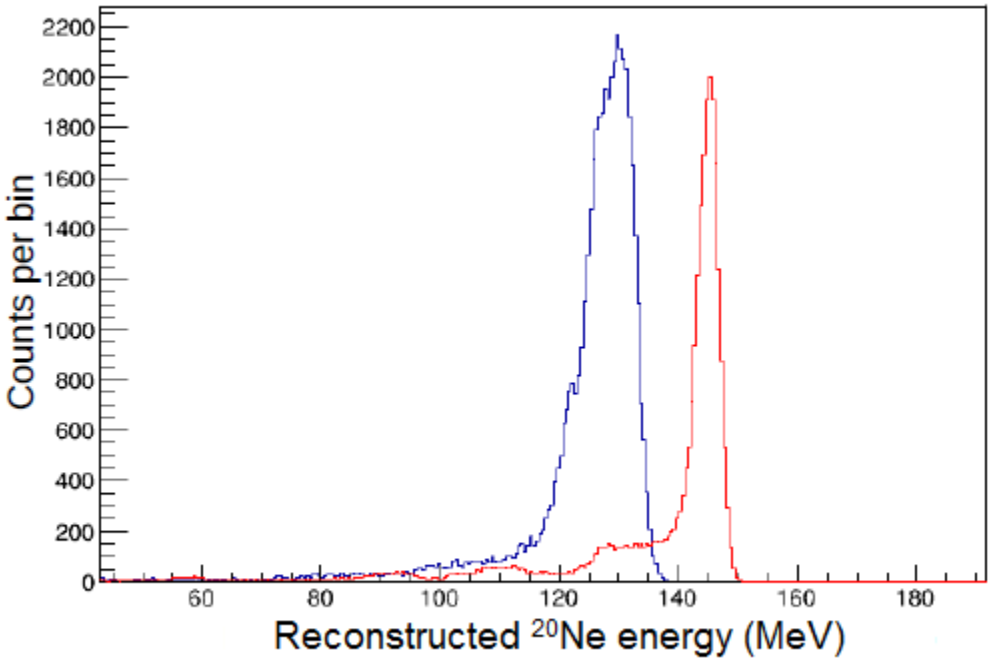

FIGURE 4.12: Reconstructed ^{20}Ne energy with (blue) and without (red) D_2 target.

The energy loss by deuterons in the remaining target thickness, YY1 detector and aluminized mylar foil wrapping can be calculated. By subtracting these energy losses from the energy at interaction point, the energy deposited in the CsI(Tl) detector can be calculated. For a given sector, once the calculated and measured (uncalibrated) kinematic plots are obtained, the two plots can be matched by minimizing the χ^2 value. The calculated energy and channel number are related through the relationship first defined in equation 4.4. Here gain is given by

$$g = g0 + g1 \times \theta \tag{4.7}$$

where *g0* and *g1* are free parameters extracted from the best fit to the data and θ is the laboratory scattering angle in degrees. Figure 4.15 shows the best fit kinematic curve compared to the data for one sector of CsI(Tl) detector.

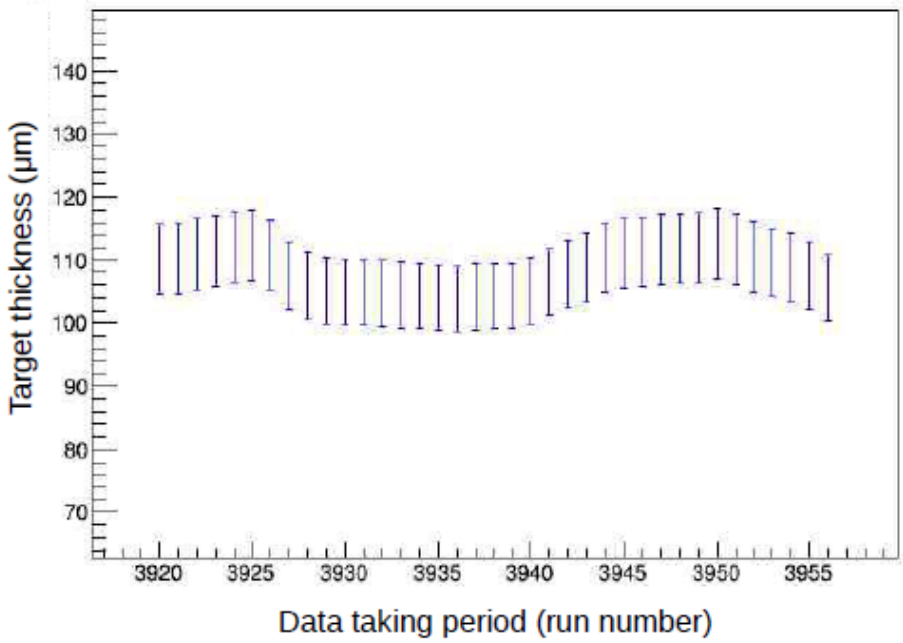

FIGURE 4.13: Target thickness during each run for ^{20}Ne data.

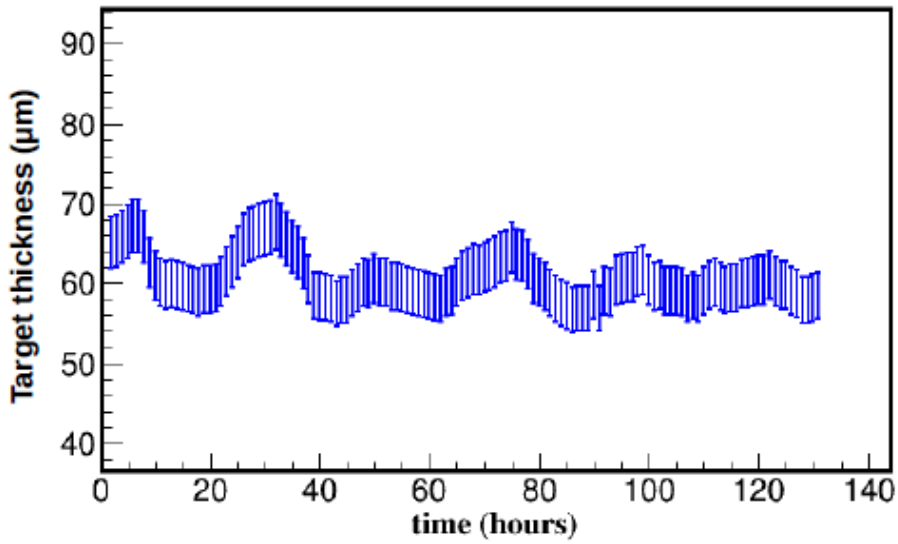

FIGURE 4.14: Target thickness as a function of time for ^{20}Mg data.

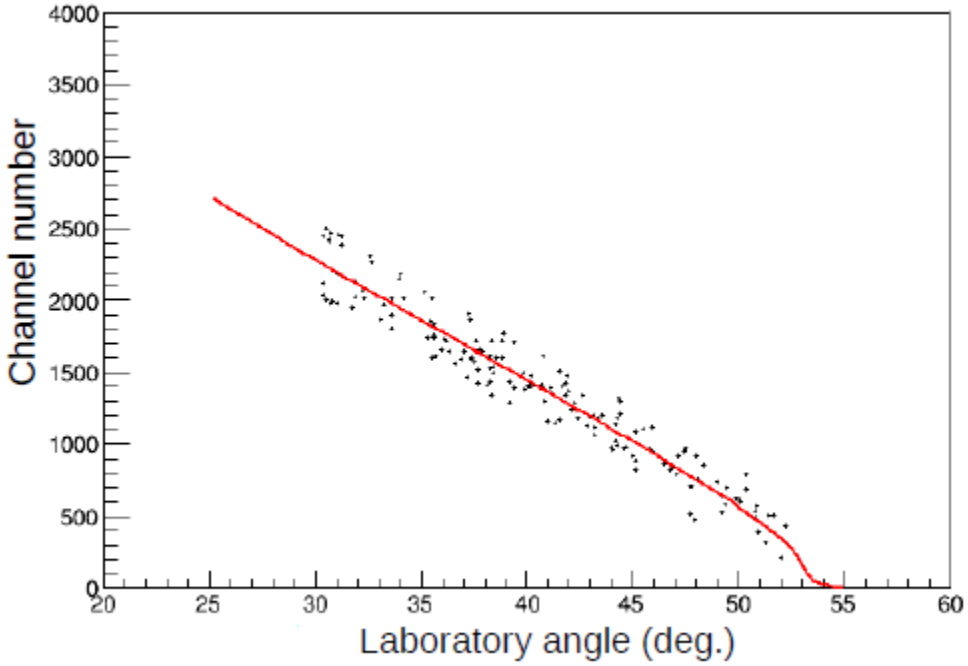

FIGURE 4.15: Measured kinematic locus for ^{20}Ne(d, d′)^{20}Ne*(E$_x$ = 4.24 MeV) (black points). The red curve is the calculated kinematic locus with the calibration parameters that give minimum chi-square value fitted to the data.

Once *g0* and *g1* are known, an angle dependent gain can be obtained using equation 4.7. Since angles corresponding to the rings of the YY1 are known, the gain was obtained for each YY1 ring coincident with each of the sixteen sectors of the CsI(Tl) detector. The CsI(Tl) detector is not segmented so angle information is taken from the YY1 detector. For calibration purposes, the second excited state of ^{20}Ne was used. The calculated kinematic loci for energy deposited in CsI(Tl) were plotted for all the observed states and (see Figure 4.16) which shows good agreement over all the laboratory angles.

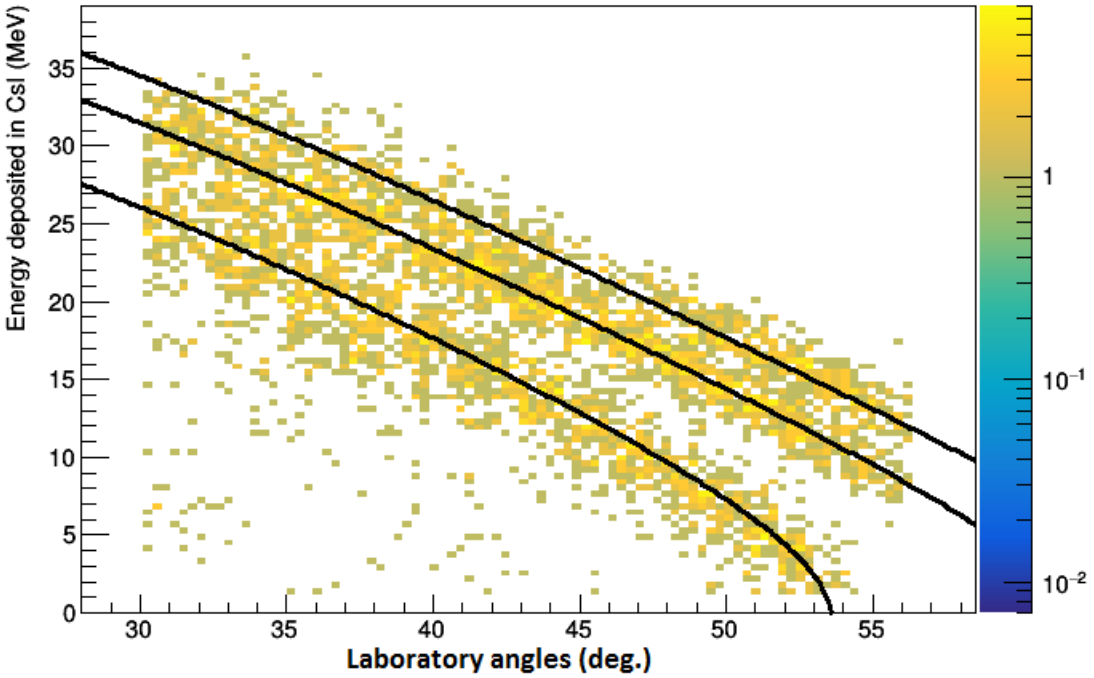

FIGURE 4.16: Kinematic loci for ^{20}Ne(d,d') using calibrated CsI(Tl). Black lines are calculated kinematic curves for elastic scattering, and inelastic scattering to first excited state in ^{20}Ne at 1.63 MeV and second excited state in ^{20}Ne at 4.24 MeV.

4.4 Particle identification and kinematics of deuterons

4.4.1 Particle identification

The reaction channel of our interest is inelastic scattering of deuterons from ^{20}Mg. However, as pointed out earlier, there are other reaction channels open at this energy. Along with deuterons, protons, ^{3}He and ^{4}He are lighter, target like reaction products coming predominantly from ^{20}Mg(d,p)^{21}Mg, ^{20}Mg(d,^{3}He)^{19}Na and ^{20}Mg(d,^{4}He)^{18}Ne respectively. These target-like lighter particles can be detected using thin silicon detector (YY1) and thick CsI(Tl) detector. The ejectiles pass through the thin YY1 detector, losing energy ΔE, and stop in the CsI(Tl) detector depositing the remaining energy (E). The energy loss (ΔE) in YY1 depends on the atomic number of the particle, and the

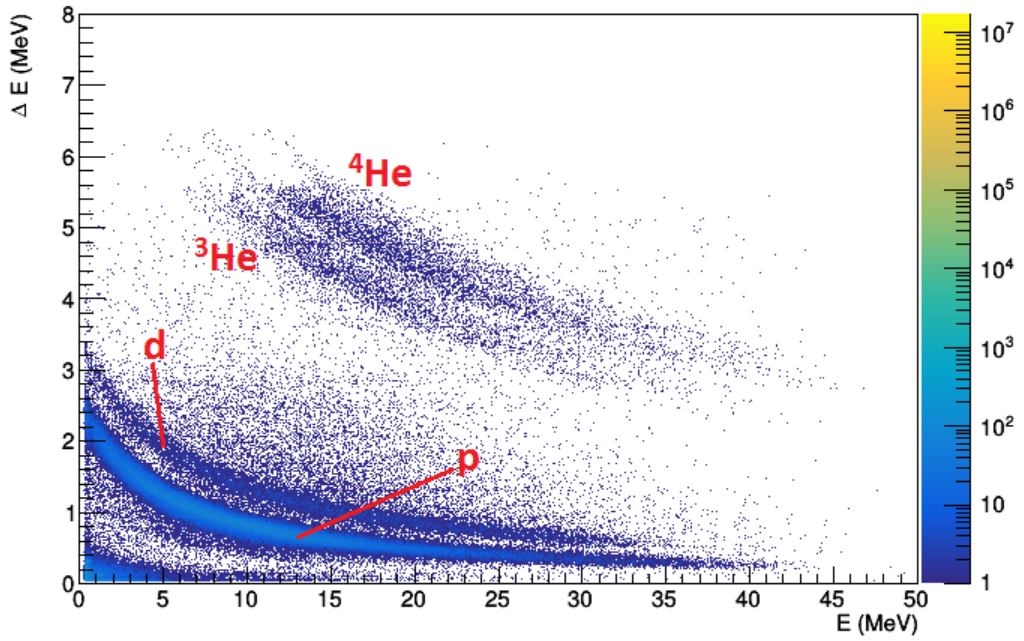

FIGURE 4.17: Particle identification spectrum with ^{20}Mg beam.

remaining energy deposited in CsI (Tl)) depends on the mass number of the impinging particle. The correlation of the signals from YY1 and CsI(Tl) helps to identify particles, thus serving as a ΔE-E telescope. Particle identification plots for ^{20}Mg impinging on solid D_2 is shown in Figure 4.17.

The particle identification plot shows bands for protons, deuterons, ^{3}He and ^{4}He. The deuterons can be selected from these particle identification plots, and the subsequent data analysis with this selection condition therefore will only be due to channels having a deuteron in the exit channel.

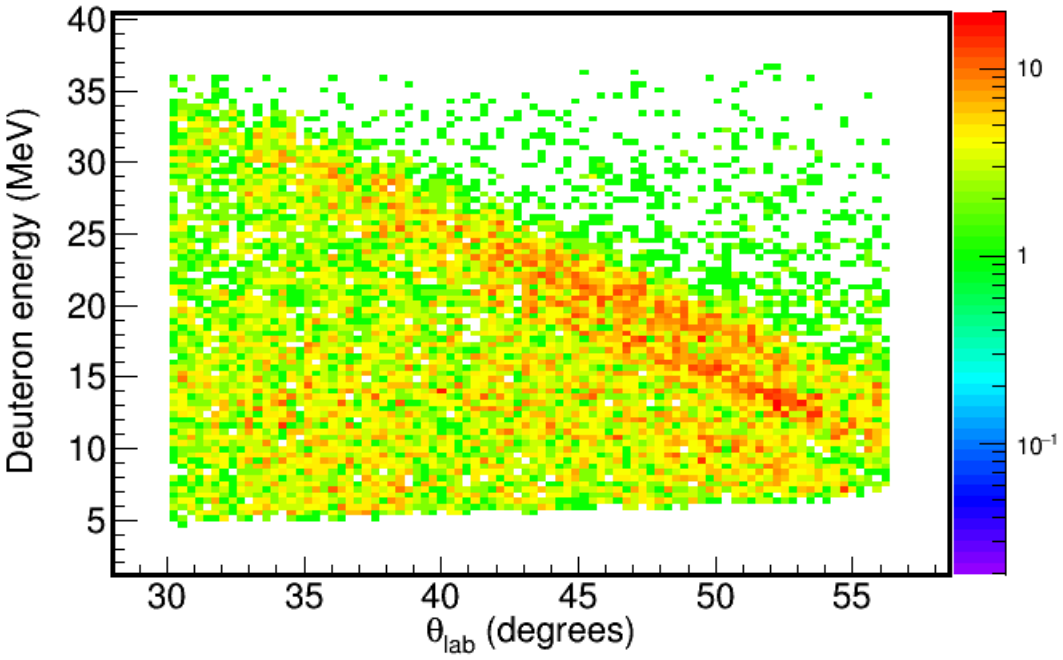

FIGURE 4.18: Kinematics of deuterons for ^{20}Mg+ d interaction.

4.4.2 Kinematics of deuterons

The kinematic locus of elastically and inelastically scattered deuterons can be obtained from the measured energy and angle information. The concentric rings of YY1 detector provide angle information whereas energy information is extracted from the measured energy in YY1 and CsI(Tl) detector. The energy of scattered deuterons at the middle of solid D_2 target was reconstructed from this measured energy information. The reconstructed energy versus the scattering angle is shown in Figure 4.18 for ^{20}Mg. This energy and angle information is required to construct the excitation spectrum using the missing mass technique.

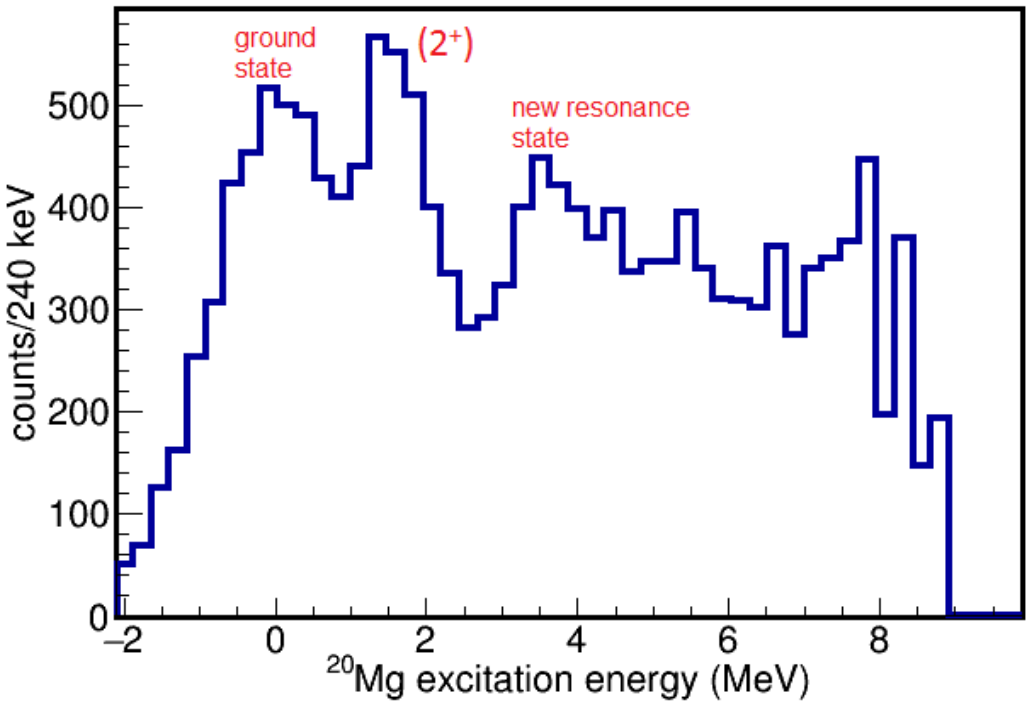

FIGURE 4.19: Excitation spectrum of ^{20}Mg.

4.5 Excitation spectrum and Angular distribution

4.5.1 Excitation energy spectrum

In Section 3.1, we discussed the missing mass technique to extract information on excited states. We demonstrated that if energy and angle of one of the scattered particles are measured, one can construct the Q value spectrum. Section 4.4.2 shows the kinematic locus for deuterons. Once this energy and angle information (along with beam energy) is known, it can be used to calculate Q value. The excitation energy spectrum can be obtained from Q value of scattering (Q = -E_{exc}).

Figure 4.19 shows the measured excitation energy spectrum for deuterons with the data

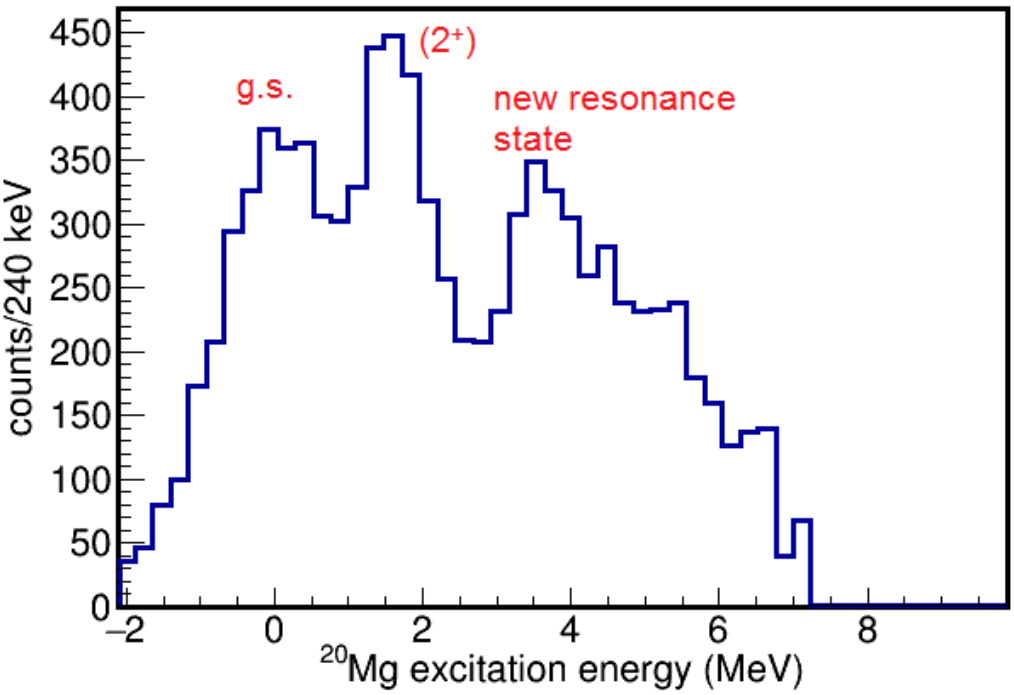

FIGURE 4.20: Excitation spectrum of ^{20}Mg for $\theta_{lab} > 40$ degrees.

integrated over the measured range of angles. However, better excitation energy resolution at higher laboratory angles allows the excited states to be better separated. Figure 4.20 shows the excitation energy spectrum for laboratory angles greater than 40 degrees. The excitation spectrum shows three clear peaks; the ground state of ^{20}Mg, a peak around 1.6 MeV which corresponds to first excited state, considered to be 2^+(Gade et al., 2007). The highlighting feature of this excitation spectrum is a prominent newly observed state in this work around 3.6 MeV. To find the peak positions of these states and to establish whether the newly observed peak around 3.6 MeV is a resonant state, we need to estimate the background contribution from reactions on Ag foil and from the four body phase space to this excitation spectrum.

4.5.1.1 Background from Ag foil

The ^{20}Mg beam passes through the Ag foil before it enters the solid deuteron target. The reactions on the Ag foil could lead to different lighter particles as reaction products (mainly from fusion-evaporation reactions). However, the non-target contributions can be measured using data from ^{20}Mg impinging on the Ag foil when no solid D_2 target is present. Figure 4.21 shows the excitation spectrum for no D_2 target data (red histogram) along with the measured excitation spectrum (blue histogram). To estimate the contribution coming from reactions on Ag foil, the excitation spectrum was normalized to the ratio of incident beam particles with D_2 target to incident beam particles without D_2 target i.e.

$$normalization\ factor = \frac{number\ of\ incident\ beam\ particles\ for\ D_2\ target}{number\ of\ incident\ beam\ particles\ for\ Ag\ foil\ only} \quad (4.8)$$

4.5.1.2 Phase space contribution

The contribution from four body phase space i.e. ^{20}Mg +d $\rightarrow$ d+p+p+^{18}Ne has been discussed in Section 4.1.4 and the energy versus scattering angle plot was shown in Figure 4.4. Using this energy and angle information, the excitation spectrum was constructed. The excitation spectrum from the four-body reaction has larger contributions at the higher excitation energy regions. To normalize the background from phase space, this contribution was matched to the total excitation spectrum (minus the Ag foil background) in excitation energy region from 6.5 MeV to 8.5 MeV through χ^2 minimization. Figure 4.22 shows the background contributions from phase space plus Ag foil overlaid on the total excitation spectrum. Figure 4.23 shows the excitation energy spectrum, and the background for laboratory angles greater than 40 degrees. This discussion shows that

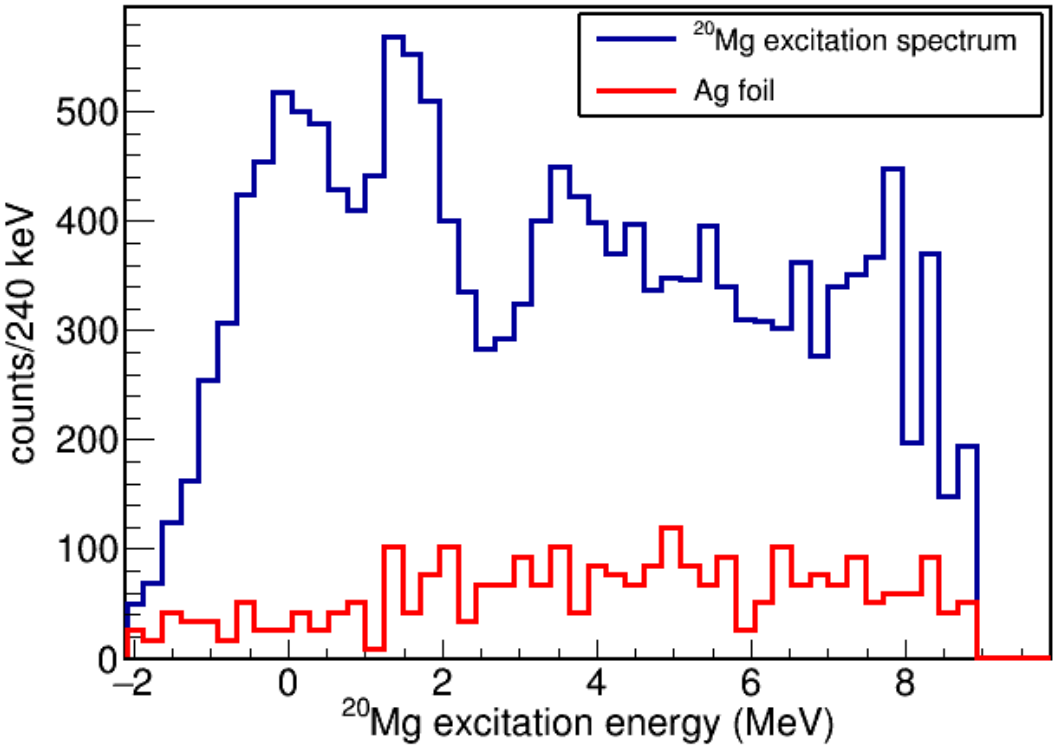

FIGURE 4.21: Excitation spectrum for ^{20}Mg (blue histogram) and background contribution from reactions on Ag foil, with all selection conditions same as used to obtained figure 4.19

the background contributions do not give rise to the newly observed state at $\sim$ 3.6 MeV.

4.5.1.3 Background subtraction and fitting

To find the peak position and width of the newly found resonance, the spectrum needs to be fitted with an appropriate function describing the resonance as well as the bound states together. The widths of the peaks of the bound states (i.e. ground state and state at $\sim$1.6 MeV) show the resolution which follows a Gaussian distribution.

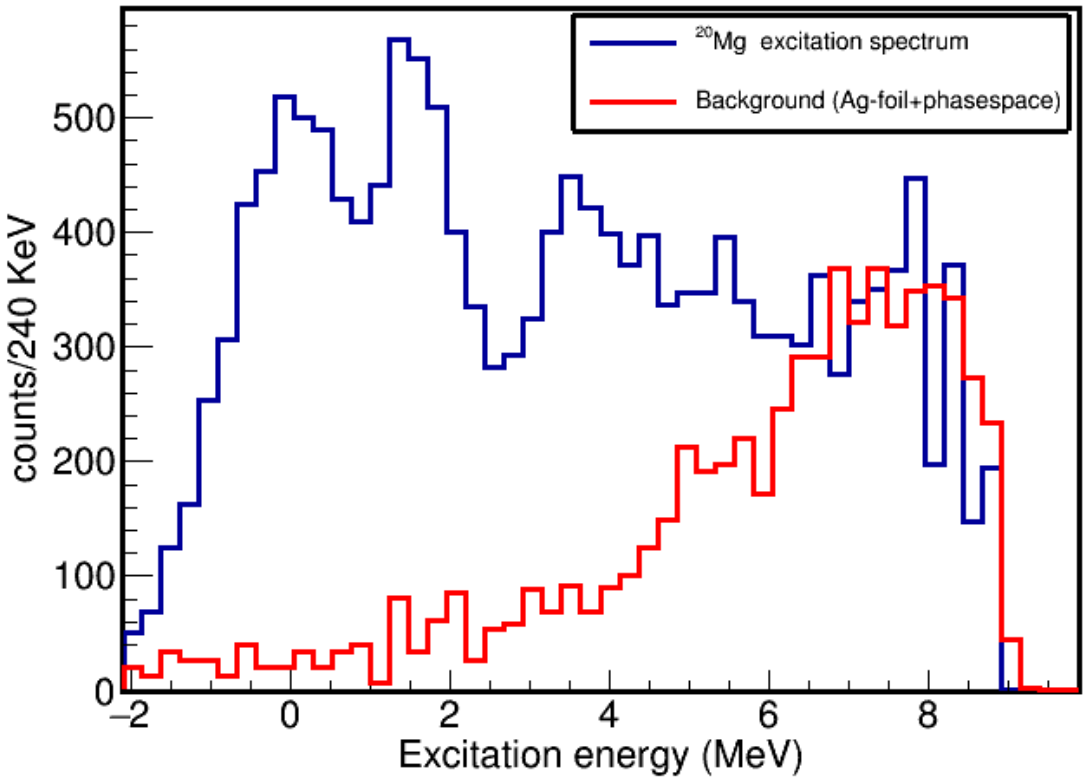

FIGURE 4.22: Excitation spectrum for ^{20}Mg (blue), and background contribution from reactions on Ag foil and four body phase space.

The states above the proton emission threshold can have large decay widths, and are represented by a Breit-Wigner distribution. Therefore, the total background subtracted excitation energy histogram was fitted with a function which is a sum of two Gaussians and a Breit-Wigner distribution with an energy-dependent width folded by the Gaussian experimental resolution. The excitation spectrum resolution is excitation energy dependent. Therefore the widths (σ) of the Gaussian functions were free parameters, but ratios of widths (σ) of the first excited state and the new state to that of the ground state were fixed using the results of Monte Carlo simulations. Figure 4.24 shows the background subtracted excitation spectrum fitted with function explained above. The extracted peak position from the fitting for the first excited state is 1.61±0.03 MeV and for the newly observed state is 3.68±0.04 MeV. As it is apparent from figure 4.24

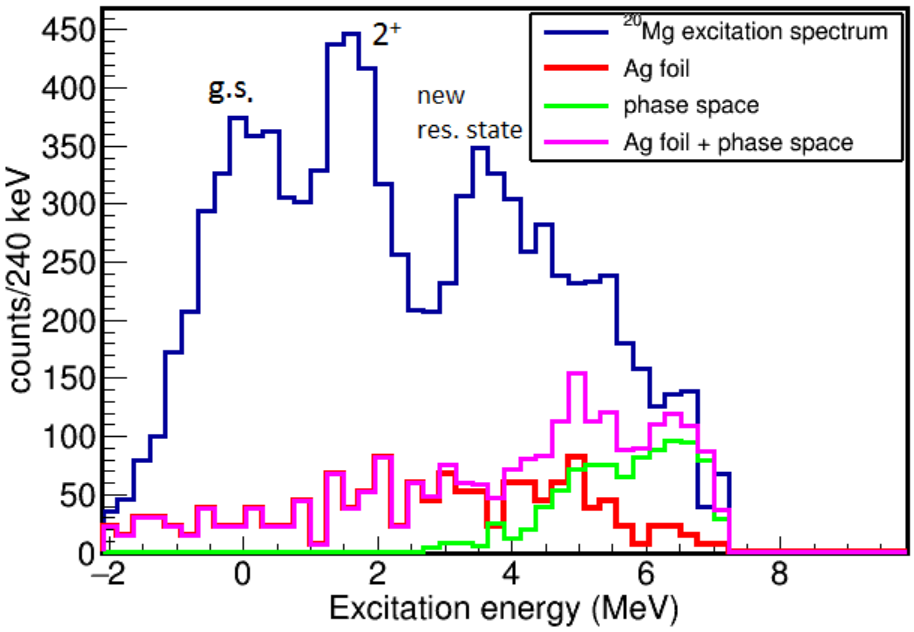

FIGURE 4.23: Excitation spectrum for ^{20}Mg (blue), individual background contributions from reactions on Ag foil, phase space and total (red), for θ_{lab} >40 degrees because excitation energy resolution is better for higher laboratory angles.

that there is unexplained excess of counts around 5.5 MeV which is not a part of 3.68 MeV state but could also be a low energy tail of a higher lying resonance. This excess could either be another new excited state or additional phase space contributions. In the present fitting of the spectrum a second new excited state was therefore not included. The width of the newly observed state was found to be 0.78±0.10 MeV (FWHM). The uncertainty in the width of the state does not reflect any systematic uncertainty, especially the uncertainty coming from any assumption about intrinsic resolution, and it thus reflects a minimum uncertainty.

4.5.2 Angular distribution

The measurement of the differential cross section is required to get the spin of the states observed in the spectrum. This section explains measurement of differential cross

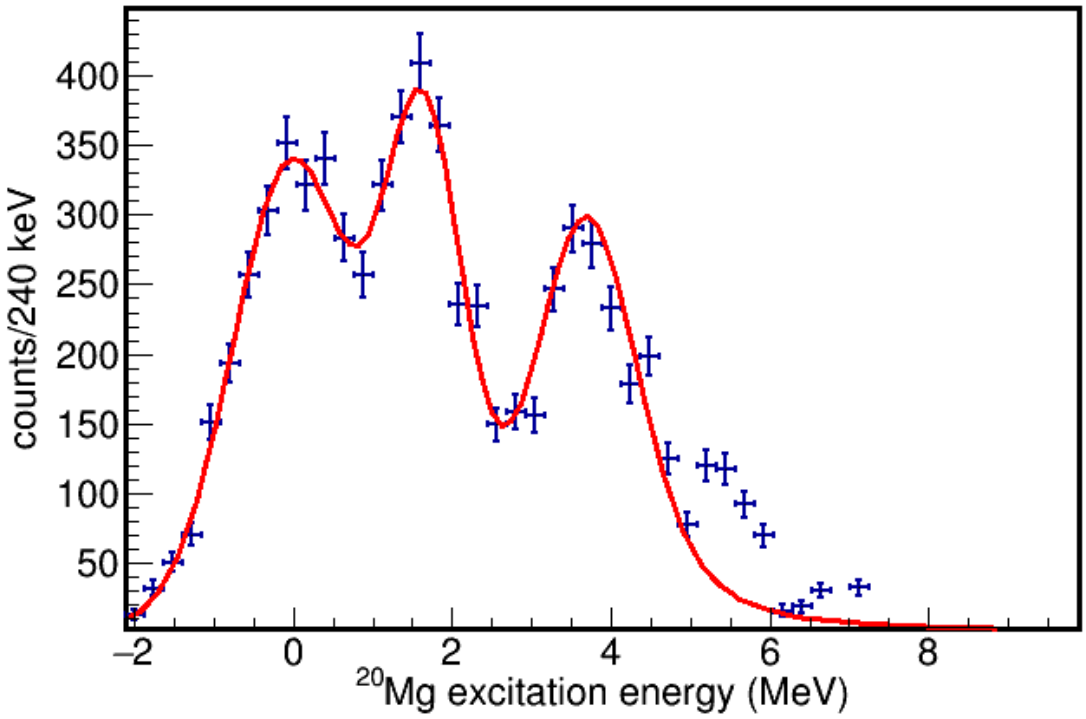

FIGURE 4.24: Background subtracted excitation spectrum fitted with a function described in section 4.5.1.3.

sections ($d\sigma/d\Omega$) for the ground state, first excited state and newly observed state at 3.68 MeV. The differential cross section can be written as

$$\frac{d\sigma}{d\Omega} = \left[\frac{N^{sc}}{N^{in}}\right] \times \left[\frac{1}{\rho t}\frac{M_t}{N_A}\frac{1}{d\Omega}\right] \tag{4.9}$$

where N^{sc} and N^{in} are the number of scattered particles and incident particles respectively. M_t, ρ and t are molar mass, density, and thickness of solid D_2 target respectively. N_A and $d\Omega$ are the Avogadro's number and solid angle respectively. Out of these various quantities M_t, ρ & N_A are constant, target thickness 't' is known at each instant and N^{in} was estimated in Section 4.2.2. To determine the differential cross sections, out of the various quantities listed in Equation 4.9, only N^{sc} and $d\Omega$ are unknown quantities at this point. The extraction of N^{sc} and $d\Omega$ for the ground state, followed by the extraction

process for first excited state and new state at 3.68 MeV, will be explained in sections to follow.

4.5.2.1 Angular distribution for ground state

get the differential cross sections for the ground state, we need to count the number of deuterons from the elastic channel in a given angular bin. To determine the number of scattered deuterons an excitation spectrum was generated for each of rings 8-13 of the YY1 detector, for which the ground state is resolved. These rings cover laboratory angles from 46.1 degrees to 53.6 degrees. We have six angular bins and counts were obtained under the 3region of the ground state peak for each angular bin. However, the area under the peak also has background contributions from Ag-foil and the Gaussian tail of the first excited state. Figure 4.25 shows the excitation spectrum for ring number 8(blue histogram) as well as estimated background from Ag-foil plus first excited state(red histogram)

The integral under the 3σ region (for blue histogram) gives total counts (N^{total}) and integral under red histogram gives background counts (N^{back}). The number of scattered deuterons is given by

$$N_d^{sc} = N^{total} - N^{back} \tag{4.10}$$

This same procedure was repeated for the other rings.

The solid angle can be written as

$$d\Omega = 2\pi \times sin(\theta_{lab}) d\theta_{lab} \tag{4.11}$$

where dθ is given by

$$d\theta_{lab} = \theta_{max} - \theta_{min} \tag{4.12}$$

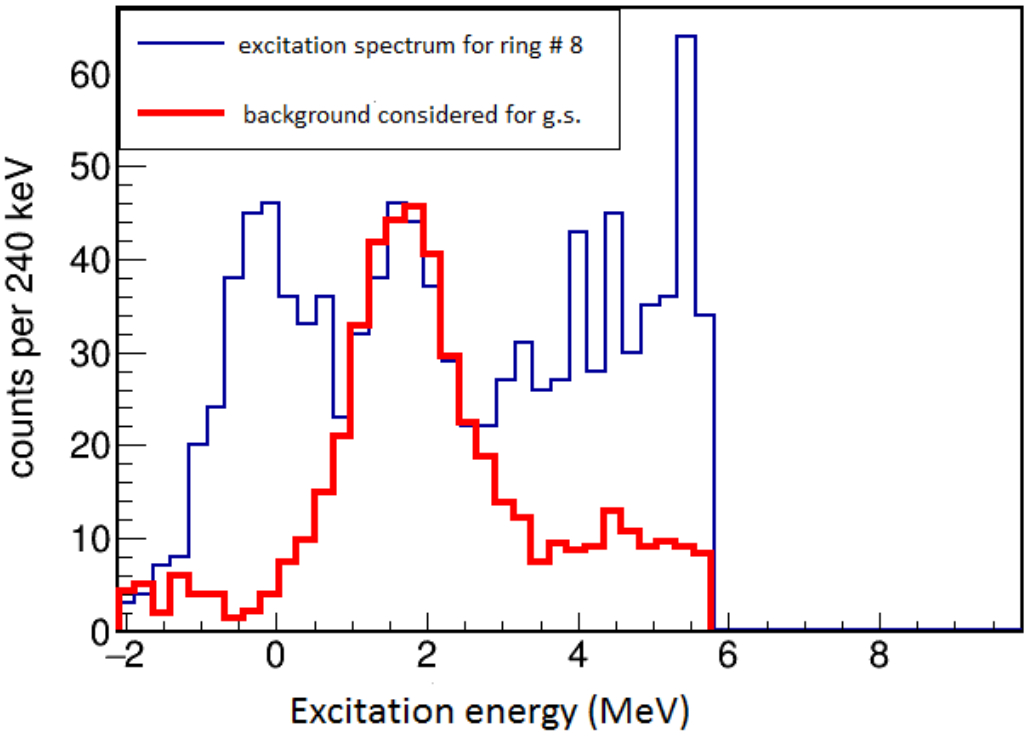

FIGURE 4.25: Excitation spectrum for ring number 8 (see text for details).

and

$$\theta_{lab} = \frac{\theta_{max} + \theta min}{2} \tag{4.13}$$

where θ_{max} and θ_{min} are the maximum and minimum laboratory angles subtended by the chosen angular bin (i.e. by the selected ring). However, we do need to take into account detection efficiency (E) so that effective solid angle will be

$$d\Omega_{eff} = 2\pi \times E \times sin(\theta_{lab}) d\theta_{lab} \tag{4.14}$$

Depending on the kinematics for a given energy state and acceptance, the detection efficiency could be same as geometric efficiency (discussed in Section 4.1.3) which is the case for ground state and first excited state. For the new resonance state at 3.68 MeV,

the total detection efficiency is different from geometric efficiency and will be discussed later. Once we have the effective solid angle and number of scattered deuterons, the differential cross sections can be written as

$$\frac{d\sigma}{d\Omega} = \left[\frac{N_d^{sc}}{\sum_i N_i^{20Mg} \times t_i}\right] \times \left[\frac{M_t}{2N_A} \times \frac{1}{\rho} \times \frac{1}{d\Omega_{eff}}\right] \times 10^{31}\text{mb/sr} \tag{4.15}$$

where

- $\rho = 0.201\times\ 10^6$ g/m^3 (Density of solid D_2 target)
- $M_t = 2\times$ 2.014 g/mol (Molar mass of D_2)
- $N_A = 6.023 \times 10^{23}$ (Avogadro's number)

and $\sum_i N_i^{20Mg} \times t_i$ is the number of incident beam counts times the target thickness summed over all the data collection time periods.

4.5.3 Uncertainty in the measurement of differential cross sections

To determine the uncertainty, we used uncertainty in the number of scattered particles, uncertainty in detection efficiency and uncertainty in the determining the target thickness. The uncertainty in the solid D_2 target thickness is taken to be 5%, reflecting uncertainty from the stopping power tables. Uncertainty in the detection efficiency is taken to be 10% pertaining to any uncertainty in the simulating the geometry and detection efficiency shows high sensitivity to detector position. These two latter uncertainties constitute the systematic uncertainty for the differential cross sections. The total uncertainty can be written as

$$\Delta\frac{d\sigma}{d\Omega} = \frac{d\sigma}{d\Omega} \times \sqrt{\left[\left(\frac{\sigma^2_{N_d^{sc}}}{(N_d^{sc})^2}\right) + \left(\frac{\sum_i \sigma^2_{t_i} \times (N_i^{20Mg})^2}{(\sum_i N_i^{20Mg} \times t_i)^2}\right) + \left(\frac{\sigma^2_{Eff}}{(E)^2}\right)\right]} \tag{4.16}$$

where

- $\sigma^2_{N_d^{sc}} = \mathrm{N}^{\mathrm{total}} + \mathrm{N}^{\mathrm{back}}$
- $\sigma^2_{t_i} = \frac{25}{10000} \times (t_i)^2$
- $\sigma^2_{Eff} = \frac{100}{10000} \times (E)^2$

4.5.4 Differential cross sections in centre-of-mass frame

The discussion above explains the measurement of differential cross sections in the laboratory frame. The angular distributions in the centre-of-mass (CM) frame of reference can be obtained as

$$\frac{d\sigma}{d\Omega}_{cm} = \frac{d\sigma}{d\Omega}_{lab} \times \frac{d\Omega_{lab}}{d\Omega_{cm}} \tag{4.17}$$

where $d\Omega_{lab}/d\Omega_{cm}$ is the Jacobian of transformation from laboratory frame to CM frame. This Jacobian is defined as

$$J_{lab \to cm} = \frac{d\Omega_{lab}}{d\Omega_{cm}} = \frac{sin(\theta_{lab}) \times d\theta_{lab}}{sin(\theta_{cm}) \times d\theta_{cm}} \tag{4.18}$$

The relationship between laboratory angles and center-of-mass angles can be obtained from the kinematics. Figure 4.26 shows the relation between CM angle and laboratory angle for the ground state. The extracted angular distribution for ground state in the CM frame is shown in Figure 4.27.

4.5.4.1 Angular distribution for the first excited state of ^{20}Mg

The process to extract the angular distribution for the first excited state is similar to that of the ground state. However, for the first excited state, laboratory angles from 46 degrees to 56 degrees have been divided into the five different angular bins where each angular bin is equal to two degrees. During the background estimation, the tails

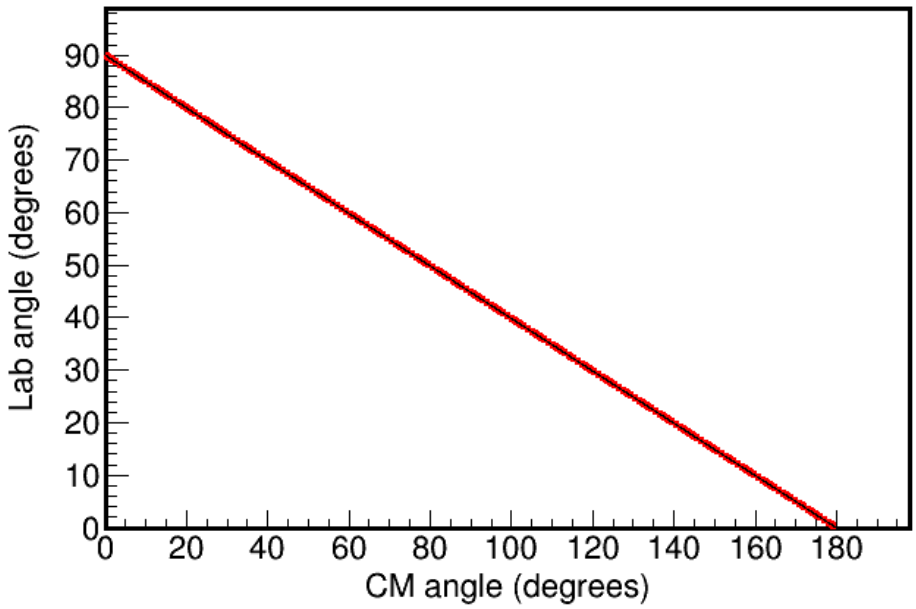

FIGURE 4.26: Relation between CM angle and laboratory angle for ground state

of the ground state and excited state at 3.68 MeV have been considered along with the contribution from the Ag-foil and four body phase space. Figure 4.28 shows the excitation spectrum (in blue) for the first angular bin (i.e. θ_{lab} from 46 to 48 degrees) and estimated background (in red). A similar process was repeated for the other angular bins. Relation of θ_{cm} and θ_{lab} is shown in Figure 4.29. The extracted angular distribution for the first excited state is shown in Figure 4.30.

4.5.4.2 Angular distribution for newly observed state

The process to extract angular distribution for the new resonance state is also similar to that of the ground state and first excited state. To determine the number of scattered deuterons, excitation spectrum was generated for each of the rings 12-14 of the YY1 detector, for which the new resonance state is resolved. During the background estimation, the tail of first excited state has been considered along with the contribution from

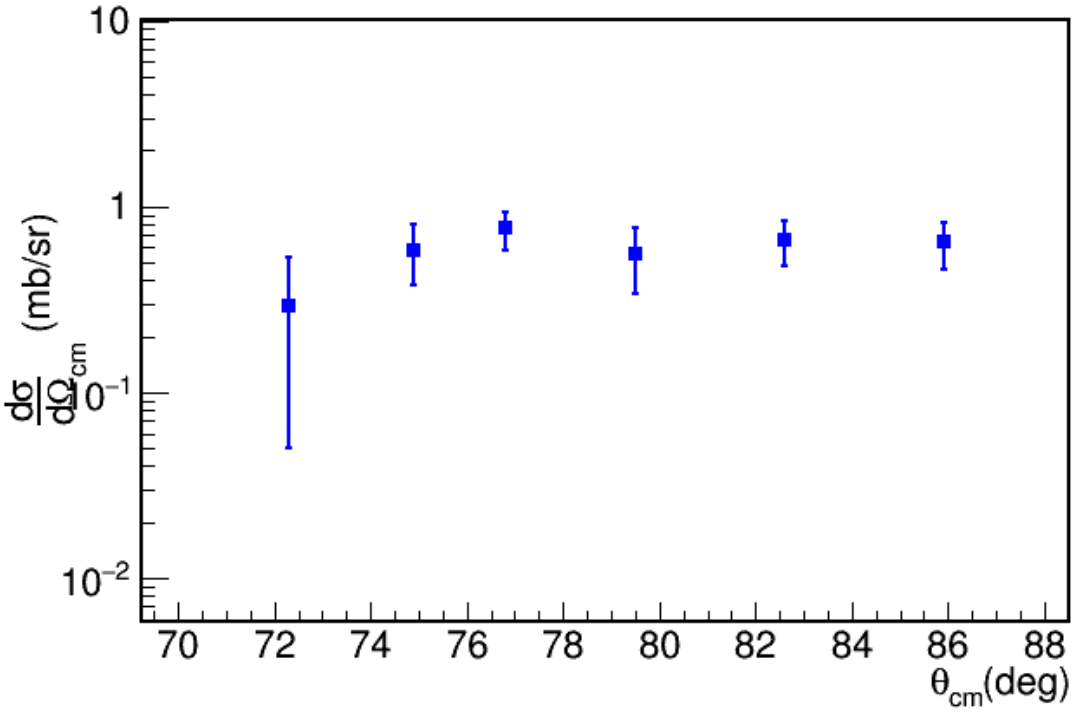

FIGURE 4.27: Angular distribution for ^{20}Mg(d, d)^{20}Mg(g.s.).

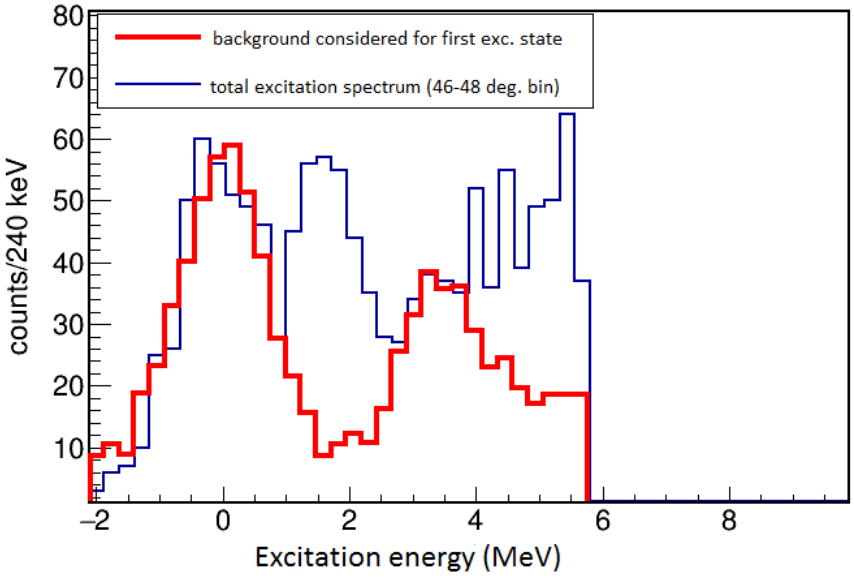

FIGURE 4.28: Excitation energy spectrum for one angular bin. See details in the text.

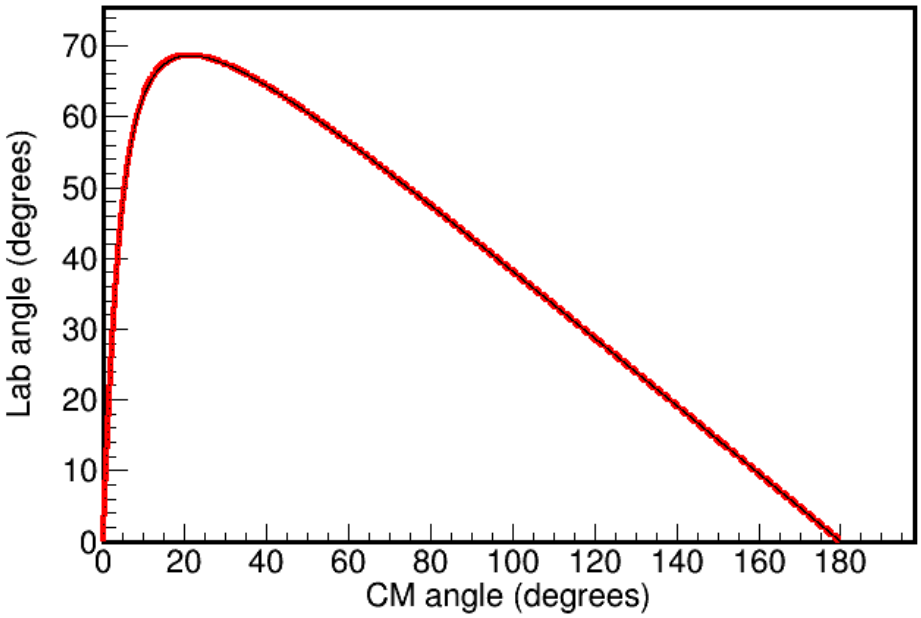

FIGURE 4.29: Relation between CM angle and laboratory angle for the first excited state

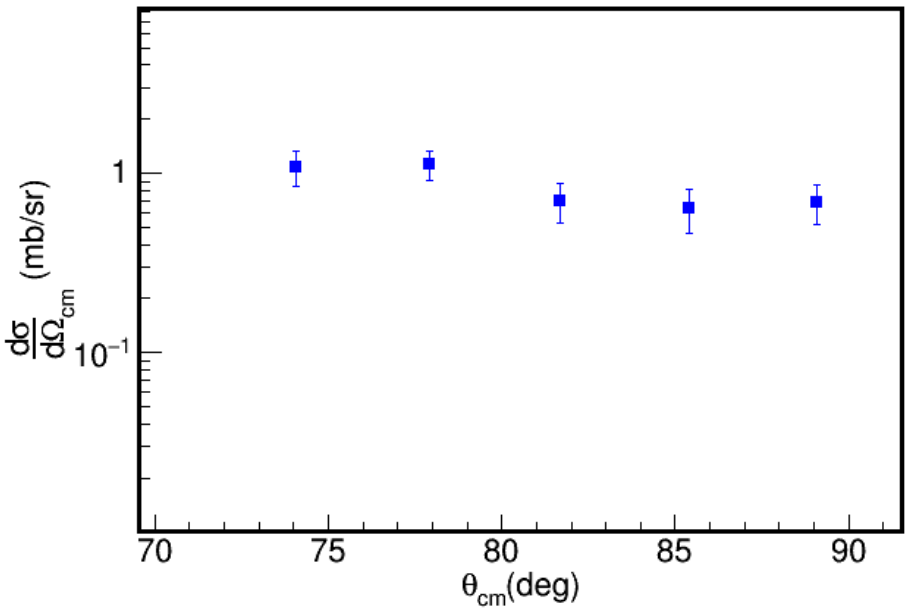

FIGURE 4.30: Angular distribution for the first excited state

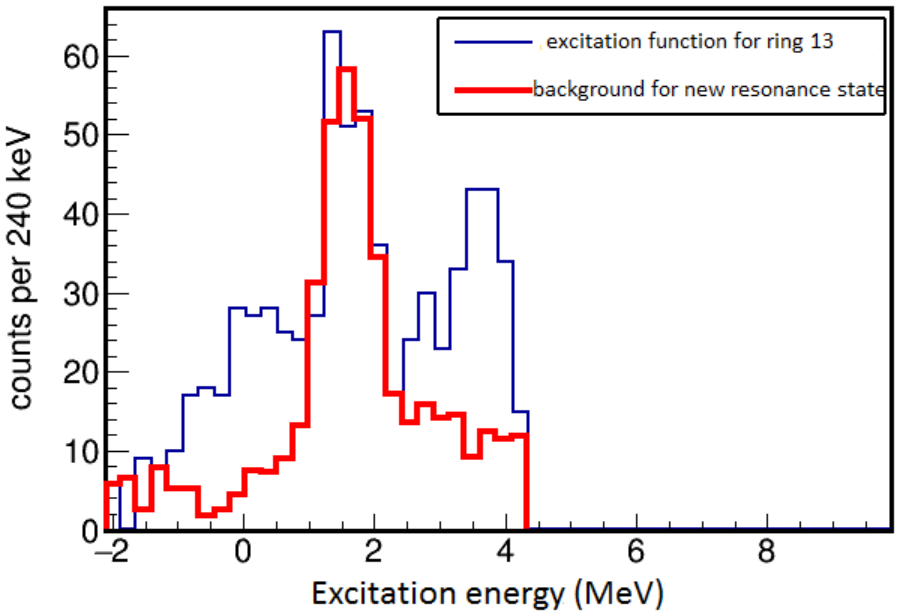

FIGURE 4.31: Excitation spectrum for one of the angular bin (ring 13).

Ag foil and four body phase space. Figure 4.31 shows the excitation spectrum (in blue) for one of the angular bins (ring 13) and estimated background (in red). The integral under the 3σ region for the blue histogram gives the total counts and the integral under the red histogram gives the background counts. The deuterons counts were obtained for other bins too through a similar process. The relationship of θ_{cm} and θ_{lab} is shown in Figure 4.32. The total efficiency for new resonance state is different than geometric efficiency due to kinematics. Therefore the total detection efficiency as a function of excitation energy was obtained for each angular bin from simulation. Figure 4.33 shows the detection efficiency as a function of excitation energy for one of the angular bin (ring 13). The extracted angular distribution for the new resonance is shown in Figure 4.34.

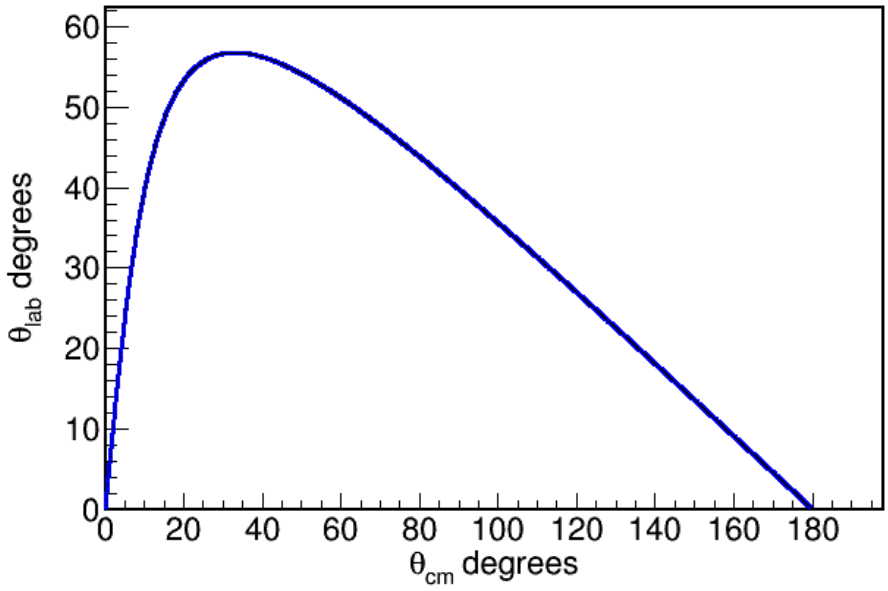

FIGURE 4.32: Relation between CM angle and laboratory angle for new resonance state.

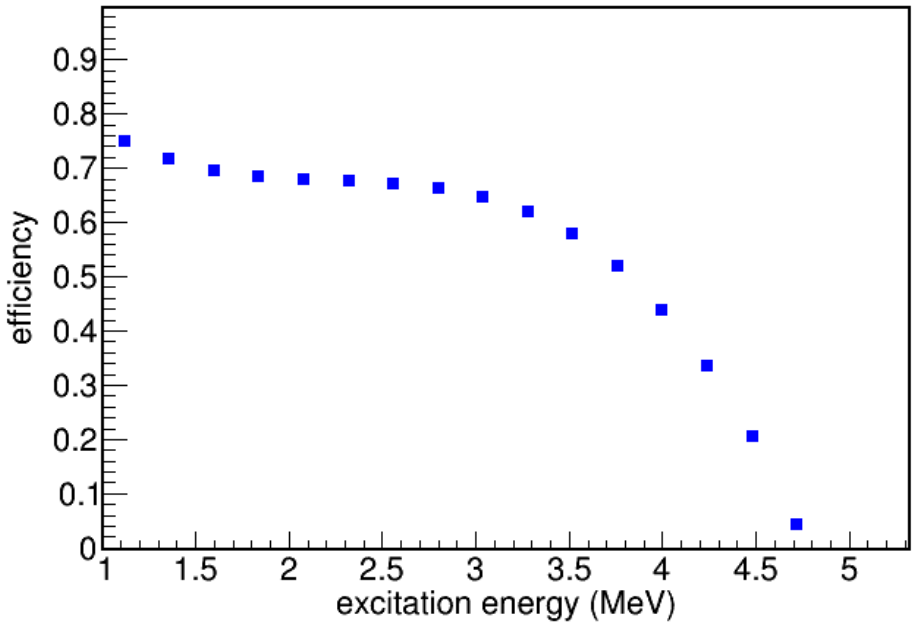

FIGURE 4.33: Detection efficiency as a function of excitation energy for one of the angular bin (ring 13).

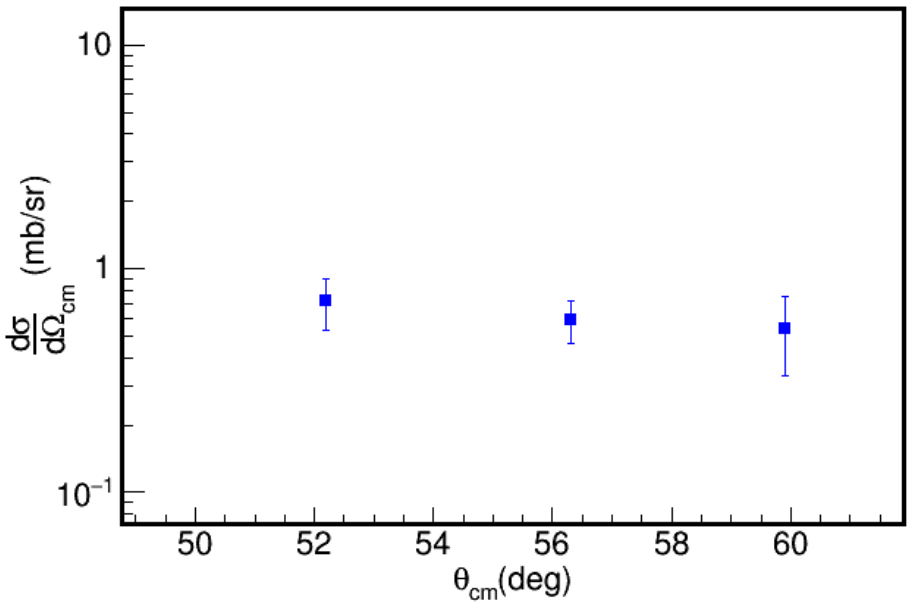

FIGURE 4.34: Angular distribution for new resonance state.

Chapter 5

Results and Discussion

This chapter describes the impact of the new resonance state observed for ^{20}Mg on the ^{18}Ne(2p, γ)^{20}Mg reaction rate, and the possible constraints it can bring on nuclear structure models and interactions. Section 5.1 presents the distorted wave Born approximation calculations for the angular distributions of the ground state and excited states. In Section 5.2, the results obtained in the present experiment are compared with various theoretical predictions of excited states in ^{20}Mg. Section 5.3 explains the significance of the new resonance state for the ^{18}Ne(2p, γ)^{20}Mg reaction rate.

5.1 Spin of the states

To get the spin of states, angular distributions were interpreted in the framework of a one-step Distorted Wave Born Approximation (DWBA) calculation using the code FRESCO (Thompson, 1998). The best fitted calculated elastic scattering angular distribution provides the optical potential parameters (Figure 5.1). These parameters were then used to calculate the inelastic scattering angular distribution for L = 2 since that is the expected multipolarity of excitation for the 1.6 MeV state. Other possibilities as

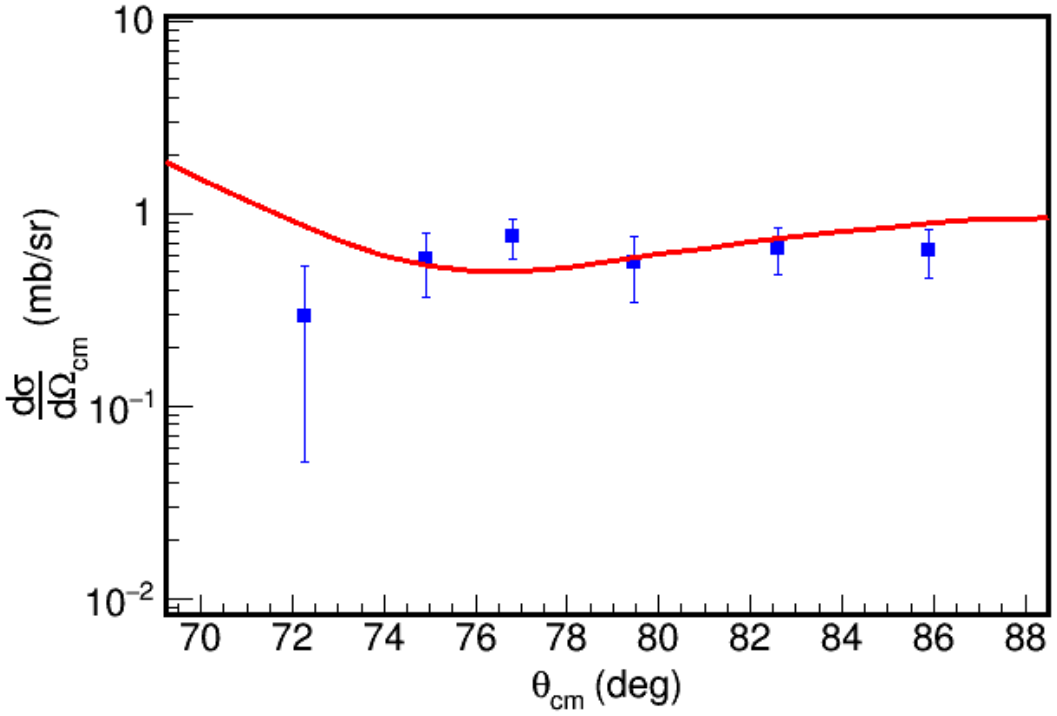

FIGURE 5.1: Elastic scattering angular distribution (blue squares). Reduced χ^2 value is 1.5. The curve shows the distorted wave Born approximation calculation.

multipolarities, L=0 or 4 has not been considered. This state has been observed via gamma ray transition (Gade et al., 2007) which rules out the possibility of L=0. This is the first excited state and no other state has been observed below this state therefore L=4 was not considered for this state. The measured angular distribution is consistent with the calculated angular distribution for L=2 (figure 5.2), reduced χ^2 square value is 0.05 for best fit normalization to data and gives this state a spin of 2^+ and is consistent with the previous assumption (Gade et al.,2007).

Similarly, the inelastic scattering angular distributions for L= 2 and 4 multipolarities of excitation were calculated for the newly observed resonance state at 3.68 MeV. However, for this state, angular distributions for both these multipolarities fits the data equally

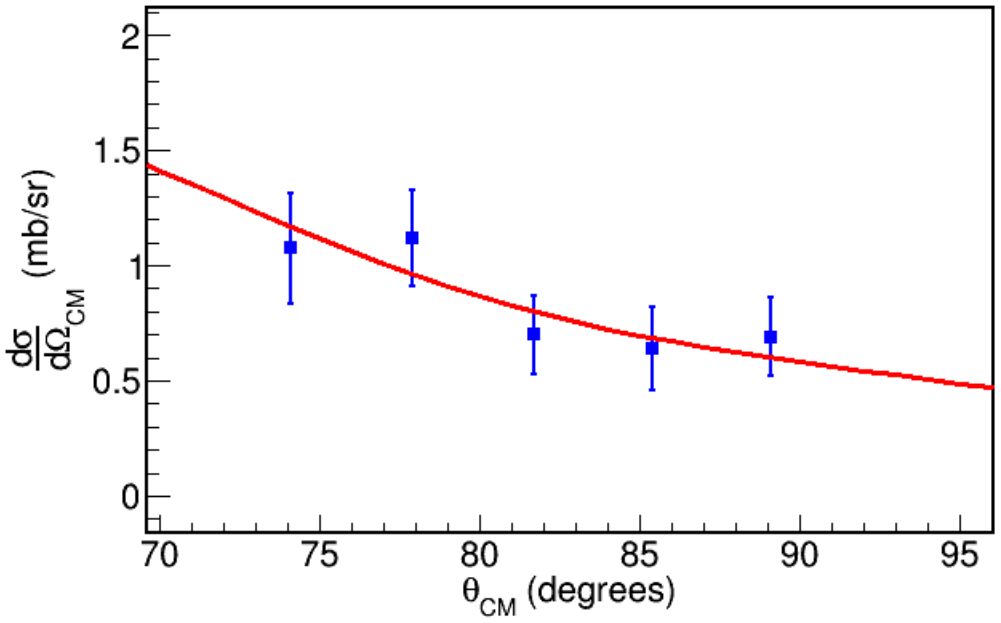

FIGURE 5.2: Angular distribution for the first excited state (blue squares). The curve is DWBA calculation for L=2 (red line).

well in the covered range of CM angles as shown in figure 5.3. The reduced χ^2 square value is 0.04 and 0.02 for L=2 and 4 respectively, for best fit normalization to the data. Therefore, our current results are not able to differentiate whether the spin of the new resonance state is either (2^+) or (4^+).

5.2 Implications for nuclear structure models and interactions

The theoretical predictions of the excited state in ^{20}Mg have been discussed in Chapter 2. Figure 5.4 shows the newly found excited state in this experiment in comparison with the three predictions.

The new observed state at 3.68 MeV is lower in energy by $\sim$ 0.8 MeV from the lowest

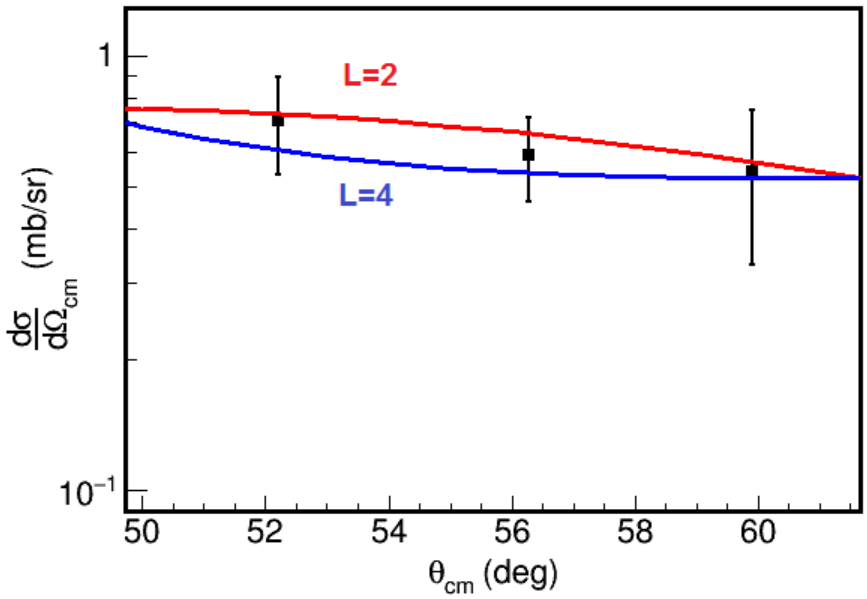

FIGURE 5.3: Angular distribution for new resonance state. The curve is DWBA calculation for L=2 (red line) and L= 4 (blue line).

predicted proton-unbound close lying 4^+ or 2^+ states by Holt et al.(2013) using chiral NN+3N interaction. For either potential spin of the new resonance state (2^+ or 4^+), the NN+3N based calculations do not predict any state near to the observed excitation energy. It has been demonstrated in the previous studies that the potentials based on NN interactions alone are inadequate to reproduce many observables even in lighter nuclei (A<10) and therefore inclusion of 3N forces is important (Navratil et al., 2007). The inclusion of 3N forces lead to two more unknown shorter-range coupling constants, generally denoted as c_D and c_E, representing the new contact terms appearing at N^2LO, i.e. next to next leading order (Gazit et al., 2009). These coupling constants are extracted through fits to existing nuclear data. In the work of Holt et al. (2013), the shorter-range 3N couplings, c_D and c_E were extracted by fits to ^{3}H binding energy and ^{4}He radius. It has been a more or less standard technique to optimize the coupling constants c_D and c_E for leading 3N forces by fits to nuclear data for A$\leq$4. Hence the difference

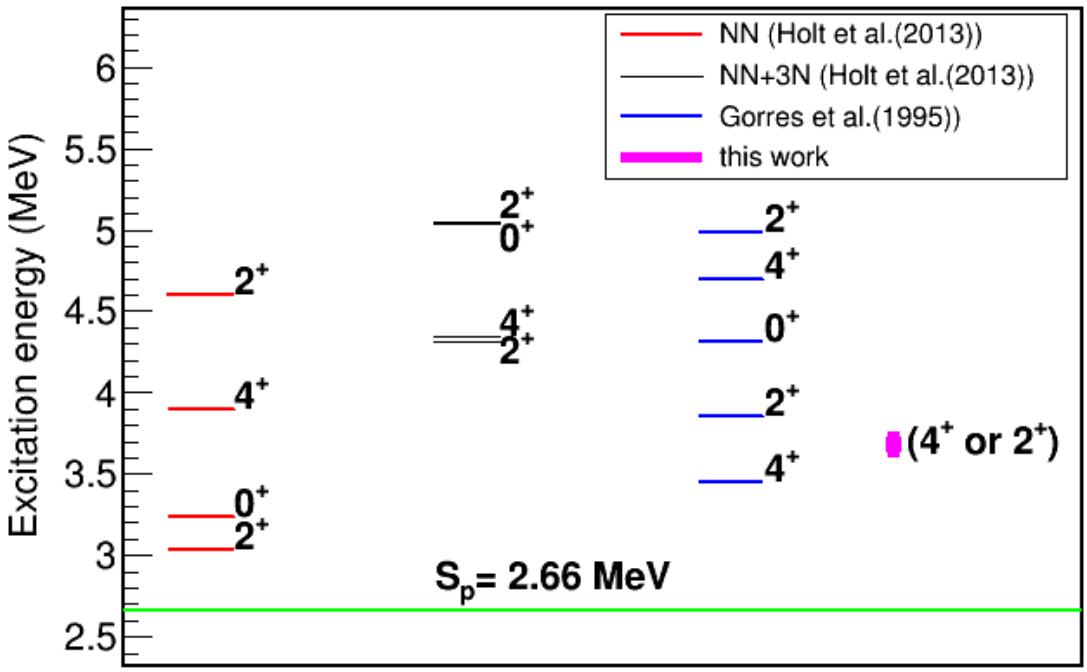

FIGURE 5.4: Comparison of the new resonance state energy to the predicted excited states in ^{20}Mg.

of ∼0.8 MeV between the experimentally observed state and 4^+ state predicted using chiral interactions and NN+3N forces could might be due to the uncertainties in the coupling constants. An alternative approach also exists where NN and 3N forces are optimized simultaneously because the long range part of 3N forces depends on lower energy constants extracted from optimization of NN forces (Ekstrom et al., 2015). It is worth mentioning here that it has been explicitly mentioned in Holt at al. (2013) that in the case of weakly bound or unbound states, an additional attractive contribution from the continuum are expected which were not included in their work. This additional attractive contribution could also shift the predicted energy levels down by few keV. The predictions with the NN interaction that show the first resonance above the proton

threshold to be at 3.03 MeV is much lower than the observed state. The measured excitation energy spectrum however does not exhibit any other resonance peak in between the 3.68 MeV state and the bound first excited state. This supports the fact that the NN interaction is not a proper description of the nuclear force. However, the failure of the prediction with the NN+3N interaction to explain the observed spectrum points to either the inadequacy of the formalism in Holt et al.(2013) and/or the proper description of the force, as described earlier. The new data obtained in this work therefore will play a vital role in constraining the model formalism and the chiral interaction. The excitation spectrum based on the mirror symmetry states in ^{20}O (Görres et al., 1995) predicts a 4^+ state as a lowest resonance at an excitation energy of 3.45 MeV. This state is 229 keV below the observed state in this experiment. The calculations based on mirror symmetry state in ^{20}O also predicts a 2^+ state at 3.86 MeV excitation energy. The observed state lies in between the 4^+ and 2^+ predicted states. We find therefore, that observed spectrum is not explained exactly by mirror symmetry consideration. The new data obtained in this work will therefore serve as a guidance to benchmark the theoretical models to explain nuclear properties at the drip line.

5.3 Impact on ^{18}Ne(2p,γ)^{20}Mg reaction rate

To calculate the total resonant reaction rate, the knowledge of excitation spectrum in the relevant energy range is required. The resonant states within the Gamow window have most significant contribution to the total reaction state. Here our discussion is for sequential two proton capture and Gamow window for second proton capture i.e. ^{19}Na(p,γ)^{20}Mg reaction is from 411.6 keV to 1143.8 keV at 1.5 GK, a typical peak temperature for X-ray bursts. The excitation energy of the new resonance state in the present work is 3.68(0.04) MeV compared to 3.451 MeV (4^+) predicted by Görres et al. (1995). To understand the impact of new resonance state on the reaction rate, both possibilities of 2^+ or 4^+ spins have been considered. Table 5.1 shows the resonance

E_x (MeV) (Görres et al.,1995)	J^π	$E_r(MeV)$	E_x (MeV) (this work)	J^π	$E_r(MeV)$
3.451	(4^+)	0.801 0.681	3.68	$(4, 2)^+$	1.02 0.9
3.857	(2^+)	1.207 1.087			
4.317	(0^+)	1.667 1.547			
4.699	(2^+)	2.049 1.929			
4.978	(4^+)	2.328 2.208			

TABLE 5.1: Excited states in ^{20}Mg and resonance energies with respect to ground state and first excited state in ^{19}Na

energies in ^{20}Mg for proton capture on ^{19}Na ground state and first excited state using excitation energy of ^{20}Mg from Görres et al. (1995) and from the present experiment.

The newly found resonance state lies within the Gamow window for $^{19}\mathrm{Na}(\mathrm{p},\gamma)^{20}\mathrm{Mg}$ reaction rate at the temperatures relevant to the X-ray bursts. Table 5.1 shows that the resonance energy in the present study is higher compared to the work of Görres et al., (1995). We calculated the resonant reaction rate for proton capture on the first two states of ^{19}Na to 3.68 MeV (4^+ or 2^+) state in ^{20}Mg and compared it to the rate estimate with the 4^+ state of Görres et al.(1995). The resonant strength is required to calculate this rate and was adopted from Görres et al.(1995). The reaction rate for proton capture in ^{19}Na states to 4^+ or 2^+ states in ^{20}Mg can be written as

$$\langle \sigma v \rangle_{19Na_{(E_i)} \rightarrow 20Mg((4,2)^+)} = \sum_i \omega\gamma_{((4,2)^+,i)} \; exp\left[-\frac{E_{((4,2)^+,i)}}{kT}\right] \tag{5.1}$$

Figure 5.5 shows this reaction rate for the present work compared to that of Görres et al. (1995). This reaction rate varies greatly with a small change in resonance energy. The rate varies less with change of spin of the resonance i.e. (4^+) or (2^+). The newly observed state leads to much lower reaction rate compared to that from the work of Görres et al. (1995) for second proton capture part (i.e. $^{19}\mathrm{Na}(\mathrm{p},\gamma)^{20}\mathrm{Mg}$ considering only one resonance in $^{20}\mathrm{Mg}$).

To calculate the total resonant reaction rate for $^{18}\mathrm{Ne}(2\mathrm{p},\gamma)^{20}\mathrm{Mg}$ reaction, other than the newly observed state at 3.68 MeV, all the other resonance energies and respective parameters were used from Table 10 of Görres et al.(1995). One should therefore note that this may still have uncertainty. Figure 5.6 shows the evaluated $^{18}\mathrm{Ne}(2\mathrm{p},\gamma)^{20}\mathrm{Mg}$ resonant reaction rate. The evaluated resonant reaction rate, which includes new resonant state from present work, is comparatively slower than the rate predicted in the work of Görres et al. (1995) for a temperature 1.5 GK and this difference is more pronounced at smaller temperatures. For comparison, the $^{18}\mathrm{Ne}(\alpha,\mathrm{p})^{21}\mathrm{Na}$ reaction rate (Matic et al. 2009) is also included in Figure 5.6. It has been found to be many orders of magnitude higher than the $^{18}\mathrm{Ne}(2\mathrm{p},\gamma)^{20}\mathrm{Mg}$ resonant reaction rate. The second proton capture part in the $^{18}\mathrm{Ne}(2\mathrm{p},\gamma)^{20}\mathrm{Mg}$ reaction rate is dictated by the newly observed $(4,\ 2)^+$ state (as it is in Gamow window) and experimental determination of this state puts the stringent constraints on the second proton capture part and hence the total resonant reaction rate. No other proton-unbound states have been observed below this state in the present study and all the states above this state will contribute only at higher temperatures. However, it is possible that there might be more resonances in the Gamow window which were not observed in current experiment. Therefore current experiment puts a lower limit on the $^{18}\mathrm{Ne}(2\mathrm{p},\gamma)^{20}\mathrm{Mg}$ reaction rate. Using current reaction rate, for $^{18}\mathrm{Ne}(2\mathrm{p},\gamma)^{20}\mathrm{Mg}$ reaction to be a viable breakout path, it has to compete with the beta decay rate of $^{18}\mathrm{Ne}$. Temperature and density conditions have been derived where $^{18}\mathrm{Ne}(2\mathrm{p},\gamma)^{20}\mathrm{Mg}$ rate is equal to beta-decay rate of $^{18}\mathrm{Ne}$ (figure 5.7). This figure shows that $^{18}\mathrm{Ne}(2\mathrm{p},\gamma)^{20}\mathrm{Mg}$ can only compete with beta decay of $^{18}\mathrm{Ne}$ at high densities. Therefore, $^{18}\mathrm{Ne}(\alpha,\mathrm{p})^{21}\mathrm{Na}$

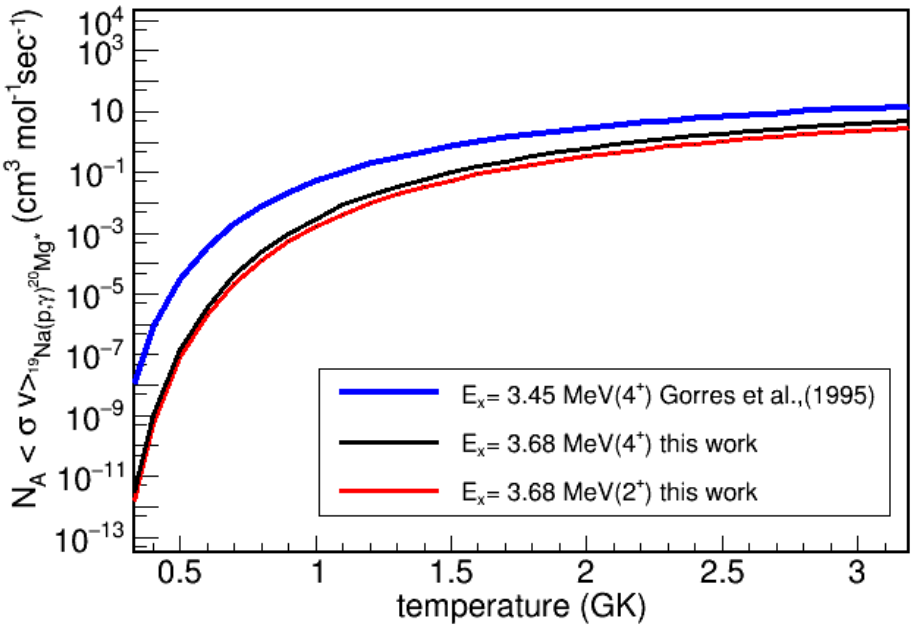

FIGURE 5.5: Comparison of proton capture rate in the first two states of ^{19}Na to $(4, 2)^+$ state of ^{20}Mg.

could be the more viable reaction to bypass the ^{18}Ne waiting point in the X-ray bursts.

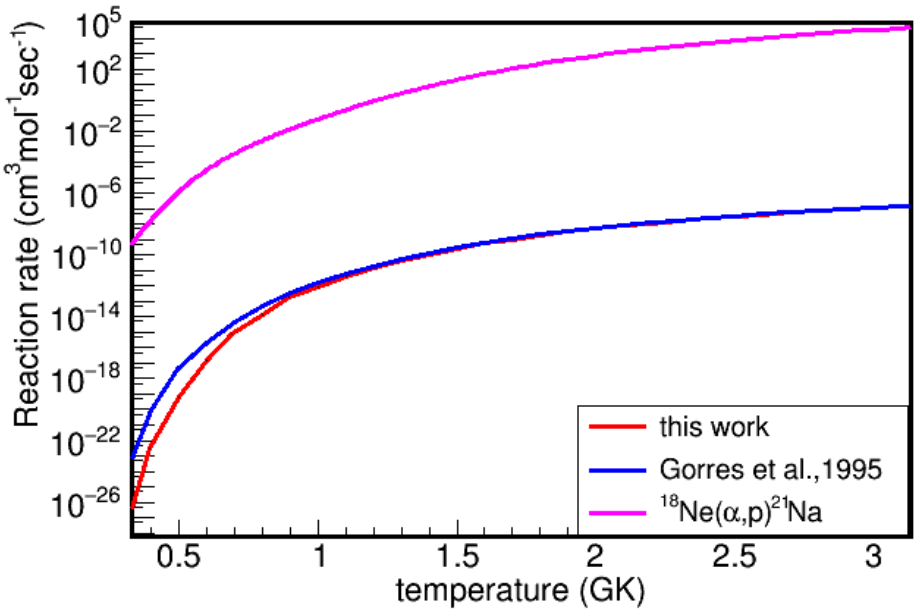

FIGURE 5.6: Total resonant reaction rate for $^{18}\mathrm{Ne}(2\mathrm{p},\gamma)^{20}\mathrm{Mg}$ reaction. For comparison, $^{18}\mathrm{Ne}(\alpha,\mathrm{p})^{21}\mathrm{Na}$ reaction rate is also shown.

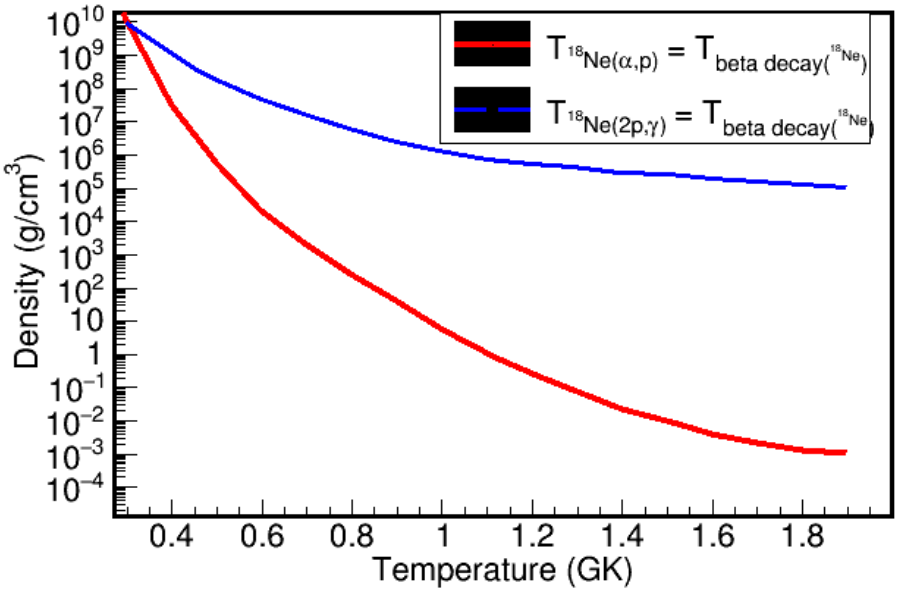

FIGURE 5.7: Temperature and density conditions where ^{18}Ne$(2p,\gamma)^{20}$Mg reaction rate is equal to beta decay rate of ^{18}Ne (blue line) and ^{18}Ne$(\alpha,p)^{21}$Na reaction rate is equal to beta decay rate of ^{18}Ne (red line).

Chapter 6

Spallation in neutron star atmospheres: a cascading destruction model

This chapter explains the method used to model the cascading destruction process (illustrated in Figure 6.1) due to spallation in the atmosphere of the accreting neutron star. The results of spallation of accreted material will be described in Section 6.2 and it's impact are summarized in Section 6.3.

6.1 Method

This study is focused on the accreted composition in the X-ray binaries and changes due to nuclear spallation reactions in the neutron star atmospheres. The kinetic energy of material free falling on a neutron star can be written as:

$$E_u = GM_\star m_u / R_\star. \tag{6.1}$$

where m_u is the mass of the accreted element , $M_\star$ is the mass, and $R_\star$ is the radius of neutron star. For a $1.4M_\odot$ neutron star with 10 km radius, the infalling material still has high kinetic energies, around 200 MeV as discussed above (assuming material is accreted vertically on to the neutron star surface). This energy translates to 56% of velocity of light, i.e. accreted protons are relativistic. Elements heavier than hydrogen and helium are thermalized due to Coulomb collisions at comparatively higher altitudes in the atmospheres. These elements then diffuse downwards and are exposed to high energy protons. The details of exposure time scales are discussed in Section 6.1.1. In Section 6.1.2, the formalism for calculating reaction rates, and details of the reaction network are discussed.

6.1.1 Elemental separation and exposure time

As defined in Bildsten et al. (1992), the electron column density needed to stop (a point where incident ion is thermalized) a particle of mass number A and atomic number Z is given by :

$$y_s = \frac{1}{\sigma_T} \frac{m_p}{6m_e} \frac{1}{\ln \Lambda} \left(\frac{v_i}{c}\right)^4 \frac{A}{Z^2}. \tag{6.2}$$

Here σ_T is Thomson cross section, m_p and m_e denote the proton and electron masses respectively, while $\ln \Lambda$ is Coulomb logarithm, and v_i is the velocity of the particle. Equation 6.2 implies that all the elements heavier than protons and ^{4}He have shorter stopping lengths (A/Z$<$ 1). As heavier elements stop at shallower depths, their downward journey is now dictated by the diffusion process. At these stopping depths, incoming protons still have high energies. The time these relatively heavy elements take to diffuse from their stopping depths to proton stopping depths is what we refer to as exposure time ($t_{\rm exposure}$) in the present study. This is the time duration for which elements are exposed to high energy protons. The accurate exposure time for each element should be calculated from diffusion process. However, in this work, we have estimated the exposure

time using diffusion estimates of Bildsten et al. (1992). Here we first define destruction time scales (destruction through spallation) (t_{dest}) as

$$t_{dest} = \frac{1}{\sigma_{dest} j_p}. \tag{6.3}$$

Here σ_{dest} is partial inelastic cross section of proton-nucleus reactions, and j_p is the proton beam current (in $cm^{-2}s^{-1}$). From Equation (1.6) of Bildsten et al. (1992) the ratio of $t_{exposure}$ to t_{dest} is given by

$$\frac{t_{exposure}}{t_{dest}} = R\sigma_{dest}\left(1 - \frac{A}{Z^2}\right) y_s(p). \tag{6.4}$$

(it should be noted that in Bildsten et al. (1992), $t_{exposure}$ was referred as residence time (t_{res})) where R was the factor obtained from diffusion calculations and R $\approx$ 5, y_s(p) is the electron column density required to stop protons. Rearranging the above equation and using Equation 6.3, $t_{exposure}$ can be written as

$$t_{exposure} = \frac{R}{j_p}\left(1 - \frac{A}{Z^2}\right) y_s(p). \tag{6.5}$$

The proton beam current j_p is given by

$$j_p = \frac{\dot{M} X_p}{m_p} \tag{6.6}$$

where $\dot{M}$ is mass accretion rate (in kg $cm^{-2}s^{-1}$)(here X_p =0.71). Using Equation 6.2 and 6.6 in Equation 6.5 and putting in all the values, we find the following expression for the exposure time

$$t_{exposure} \approx \frac{0.9}{\dot{M}}\left(1 - \frac{A}{Z^2}\right). \tag{6.7}$$

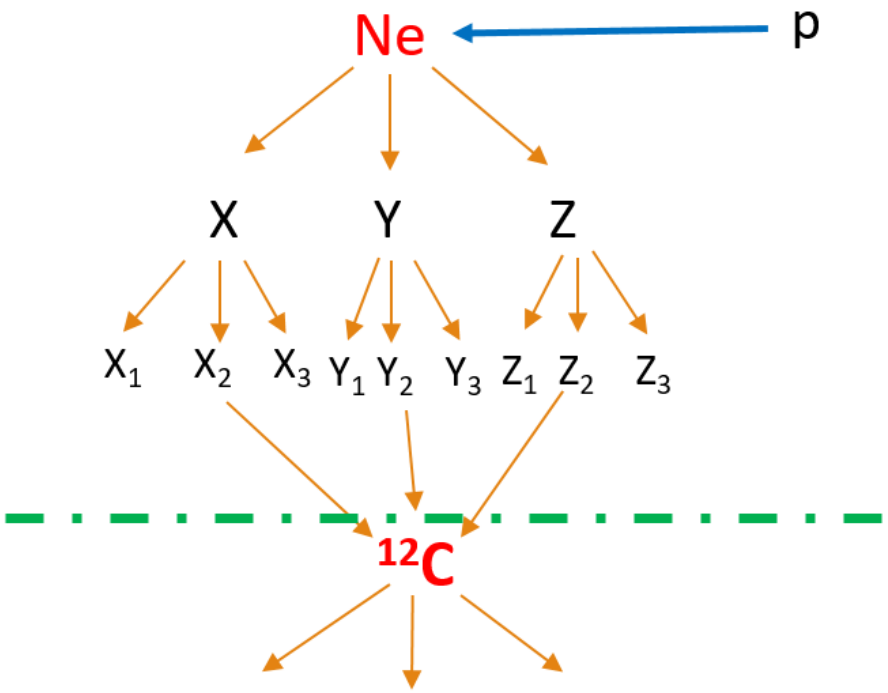

FIGURE 6.1: Schematic showing cascading destruction process. As an example,carbon has been shown to be produced via spallation of immediate higher mass elements and so on (starting from Ne). If full cascading destruction process is ignored (all process above the dotted green line), only isolated destruction of carbon will be present.

Using this expression, the calculated $t_{exposure}$ for various elements and four different mass accretion rates is shown in Figure 6.2. From Figure 6.2, there are two observations worth noting. First, for a given element the exposure time varies a lot with change in mass accretion rate . Therefore, we have performed calculations for two different exposure times corresponding to two different accretion rates i.e. $\dot{M}$ = 1kg cm^{-2} s^{-1} and $\dot{M}$ =20 kg cm^{-2}s^{-1} which corresponds to global mass transfer rates around 10^{-9} $M_{\odot}/yr$ and results for both these cases are described. Second, for a given mass accretion rate the exposure time for various elements is nearly the same. For example, in Figure 6.2 we show that the change in exposure time is very small while going from ^{12}C to ^{56}Fe. Therefore, for a given mass accretion rate we have used the same exposure time(s) for all the elements, which has been taken as the exposure time for ^{12}C.

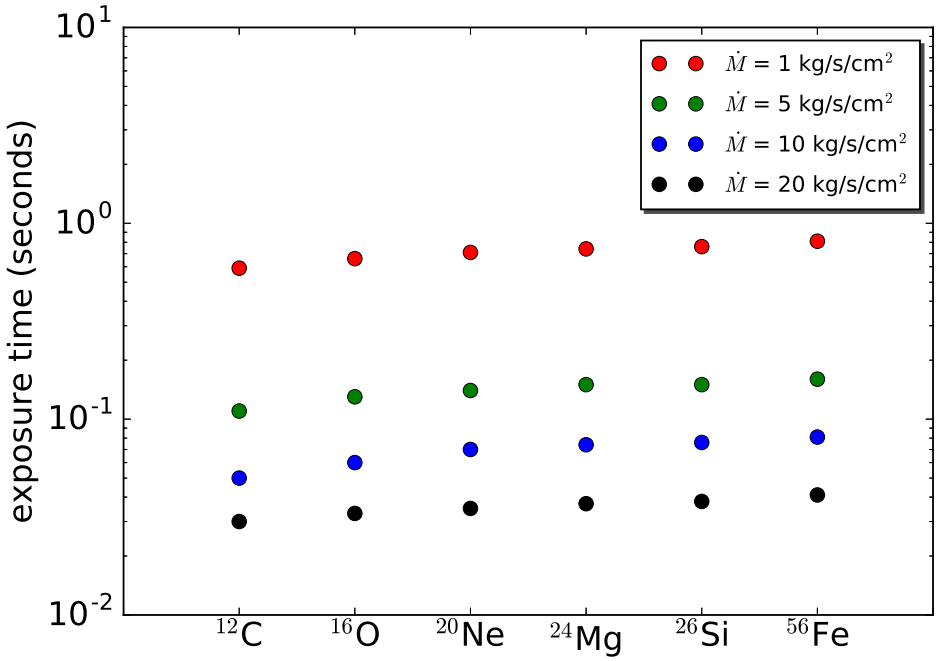

FIGURE 6.2: Expsoure time for various elements for four different mass accretion rates.

6.1.2 Reaction network and spallation reaction rates

The spallation process has been modeled using NucNet tool's single zone reaction network. The network includes total 486 isotopes from H to Fe coupled by a total of 13076 reactions. Out of these reactions, 1421 are weak reactions and rest are spallation reactions. To use the NucNet reaction network for this study, the spallation reactions were treated as decay reactions. Let's take an example of one of the proton induced spallation reactions

$$p + {}^{A}_{Z}\mathrm{X} \rightarrow p + {}^{A-2}_{Z-1}\mathrm{Y} + p + n. \tag{6.8}$$

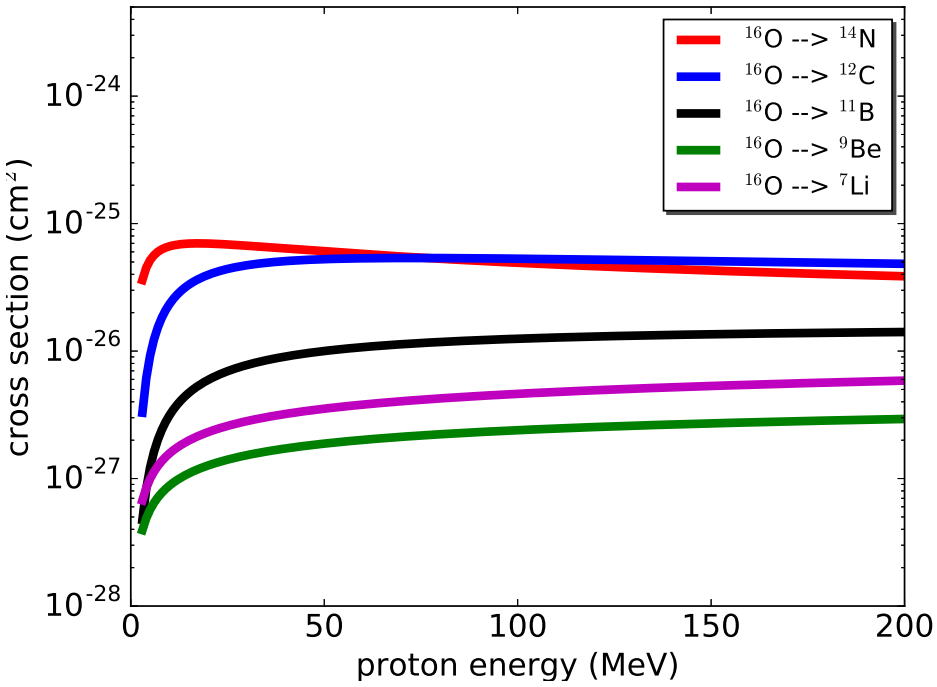

FIGURE 6.3: The partial inelastic cross sections ($\sigma(E_p)$) for production of various elements due to spallation of ^{16}O as a function of energy. These cross sections are nearly constant over the energy range 10 MeV to 200 MeV.

This can be written as a decay of particle ${}^{A}_{Z}\mathrm{X}$ by ignoring the proton in the entrance and exit channel in the above reaction i.e.

$$ {}^{A}_{Z}\mathrm{X} \rightarrow {}^{A-2}_{Z-1}\mathrm{Y} + p + n. \tag{6.9} $$

By applying this approach, it is easy to incorporate the spallation reactions in the reaction network code in a manner similar to the inclusion of beta decay rates. However, to cancel out the proton from the entrance channel a reaction should have a proton in its exit channel. Therefore, a spallation reaction can be written as a decay reaction only if the protons are present in exit channel. For this reason, the reactions without protons in the exit channel were systematically ignored for all the nuclei in this study.

The input to our spallation calculations are a list of isotopes and all reactions linking these isotopes from Fe to helium via spallation reactions (decay as a proxy) as well as beta decays and rates for these reactions. Beta decay rates were used from Nuclear Wallet Cards (J. Tuli, 2011). The spallation reaction rates were calculated using following relation (in s^{-1})

$$rate = j_p \times 10^{-27} \times \sigma(E_p), \tag{6.10}$$

where $\sigma(E_p)$ are energy dependent partial cross sections (in millibarn). The spallation cross sections $\sigma(E_p)$ in Equation 6.10 were calculated using the open source subroutines from the work of Silberberg et al.(1998).

Protons decelerate through collisions in the atmosphere. Hence they span a range of energy (E_p) with which they can induce spallation reactions. Since spallation partial cross sections are energy dependent (Equation 6.10), one expects that the spallation reaction rates are energy dependent too. However, this is not the case here as spallation cross sections are nearly constant over the energy range 10 MeV to 200 MeV. The cross sections below 10 MeV falls sharply to lower values, and a tiny fraction of protons span this energy range. Therefore we have ignored the cross sections below 10MeV. To illustrate nearly energy independent behaviour of these cross sections from 10 MeV to 200 MeV, the cross sections of ^{16}O being destroyed to ^{14}N, ^{12}C, ^{11}B, ^{9}Be and ^{7}Li are shown in Figure 6.3. These cross sections are nearly constant over almost the whole relevant energy range. For this reason, spallation reaction rates have only been considered at the fixed proton energy of $E_p = 200$ MeV. As mentioned earlier, we have examined two accretion rates in the present study and exposure times are dependent on mass accretion rate. For accretion rate $\dot{M}$ =1 kg cm^{-2}s^{-1}, the exposure time from Equation (6.7) is 0.6 seconds (using A and Z for ^{12}C) and for $\dot{M}$ =20 kgcm^{-2}s^{-1} the exposure time is 0.03 seconds (again A,Z for ^{12}C). The abundances were evolved for these two exposure times. In Equation 6.10, the reaction rate depends on j_p which is different for different

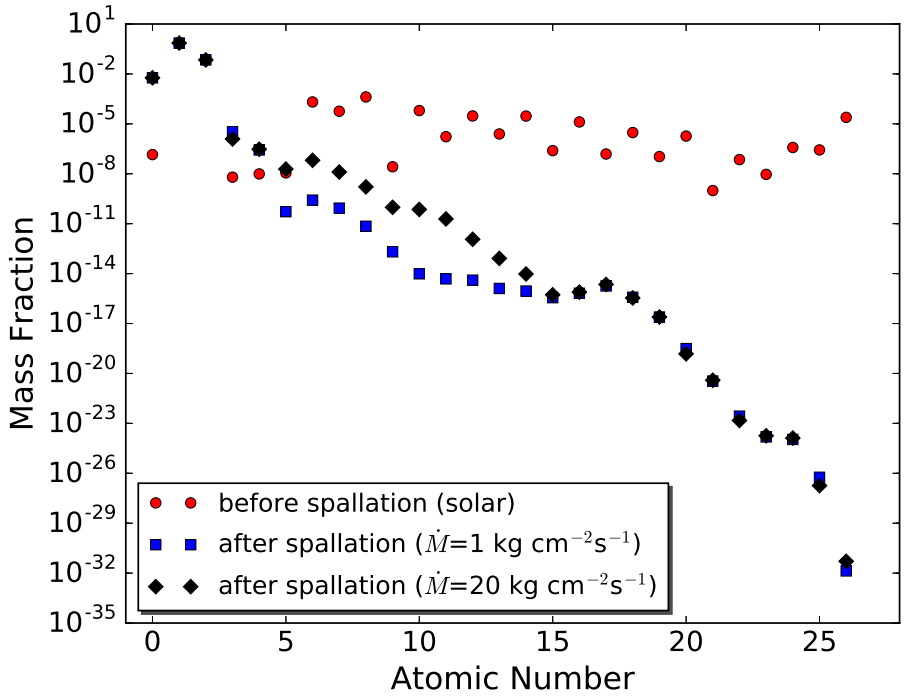

FIGURE 6.4: Accreted composition with and without spallation. Red dots show the solar composition whereas blue squares and black diamonds shows the final compositions surviving after material of solar composition goes through destruction process via spallation reactions for two different cases discussed in this study.

accretion rates, and was calculated accordingly for each accretion rate considered here. The results of the cascading destruction process are discussed in the following section.

6.2 Results and Discussion

6.2.1 Spallation reaction results

The mass fraction of elements surviving the spallation process are shown in Figure 6.4 for two different exposure times corresponding to two different accretion rates (blue squares and black diamonds). Solar mass fractions, which were used as initial abundances accreted before spallation, are also plotted for comparison (red dots).

Figure 6.4 shows that the spallation can significantly change the accreted composition from solar to sub-solar for all the elements heavier than beryllium for both the exposure times. This change is much larger for higher mass regions. However, for beryllium and lighter elements the situation is different. Destruction of these elements is smaller than their production rate because most of these elements are produced as fragment due to the destruction of heavier elements. By the time these elements are created most of them are already close to proton stopping lengths. In addition, proton induced spallation cross sections are also smaller for a smaller mass number. The major focus of this study is to see how much impact replenishment can have on final abundances of CNO elements compared to isolated destruction. Next section addresses the impact of replenishment and the final Z_{CNO} surviving the spallation.

6.2.2 Replenishment and survival of CNO elements

In Bildsten et al.(1992), destruction of individual CNO elements was considered. However, in the cascading destruction process, due to flux from the destruction of heavier elements into CNO region, the CNO abundances can be replenished. To see whether accounting for the full cascading process makes any difference compared to isolated destruction, we have explored the destruction of ^{12}C when initially only ^{12}C is present and then full cascading process has been considered. Figure 6.5 shows the time evolution of carbon for three different cases. In case one, reaction network only up to carbon has been taken into account. In this case only isolated destruction takes place i.e. carbon is being destroyed but not replenished due to spallation of elements heavier than carbon(blue line). Case two shows results for reaction network up to Neon i.e. carbon destroyed due to spallation but also replenished due to N, O, F, and Ne isotopes being destroyed to carbon directly and through spallation of other fragmentation products (red line). Case three is same as case two but with the reaction network up to Iron (green line). Figure 6.5 shows that difference in surviving carbon mass fraction is conspicuous at the

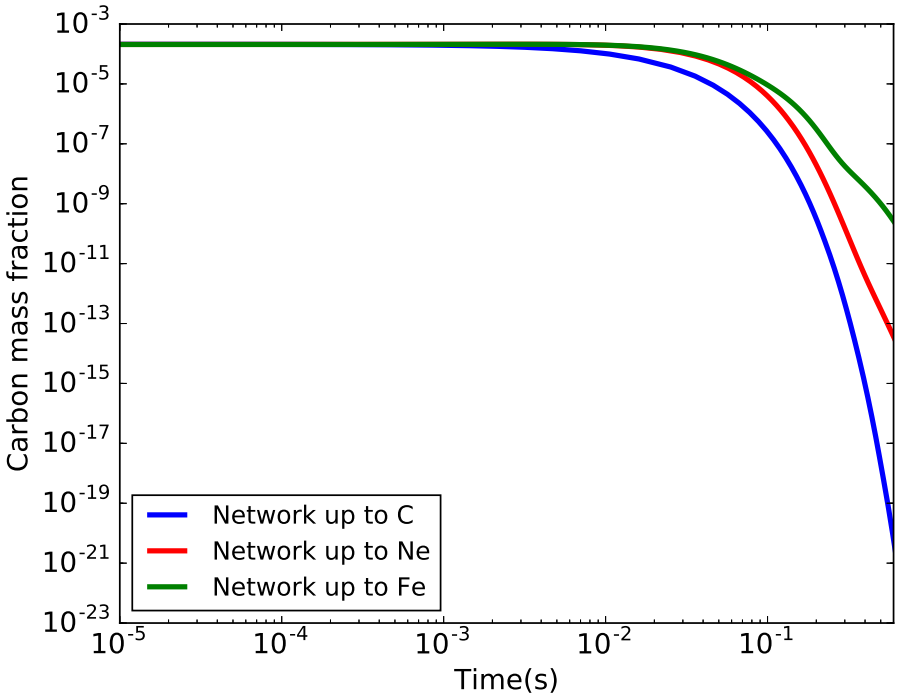

FIGURE 6.5: Time evolution of ^{12}C for three different reaction networks (for $\dot{M} = 1$kg cm^{-2}). Blue line shows carbon evolution when no spallation in mass region heavier than carbon is considered i.e isolated destruction, red line shows the carbon evolution for network upto Neon i.e cascading process from Ne to H, and green line is for network upto Fe. This picture shows that more carbon is present when extended network (or replenishment) is considered.

end of spallation. Here carbon abundance is less when there is no cascading process. These results demonstrate that the CNO elements' destruction can be overestimated if no replenishment from the destruction of the heavier mass region is considered.

To estimate the impact of spallation on Z_{CNO}, we have investigated the time evolution of Z_{CNO} for two mass accretion rates (or two exposure times) considering a full cascading destruction process. Figure 6.6 shows the time evolution of Z_{CNO}. For both the cases, Z_{CNO} falls to very small values, many orders of magnitude below the 0.1 percent of solar value. This shows that even when replenishment is considered in the cascading process, still destruction is enough to make CNO abundances negligible.

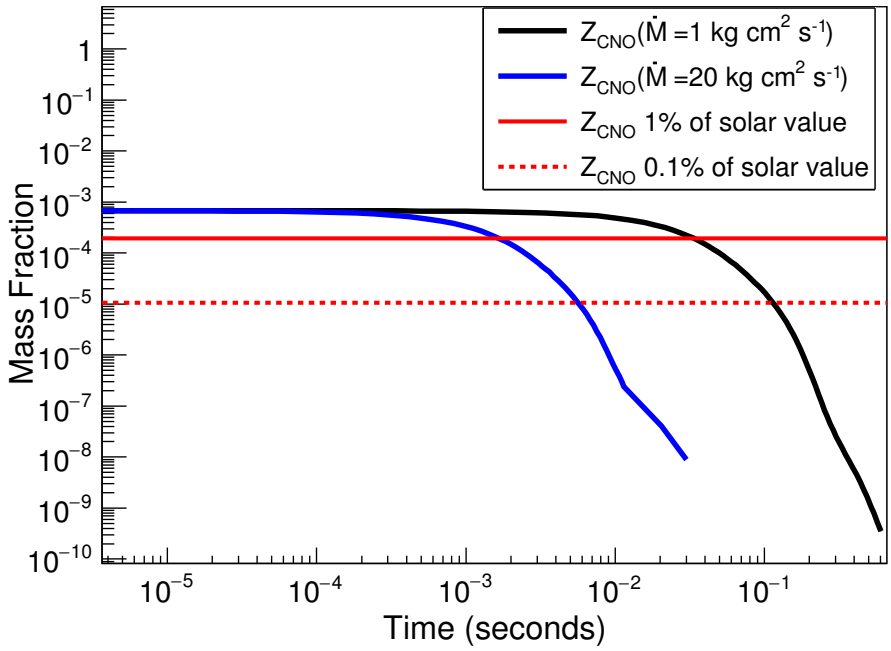

FIGURE 6.6: Time evolution of Z_{CNO} for for network upto iron for two different mass accretion rates, $\dot{M}$ =1 kgcm^{-2}s^{-1} (black line) and $\dot{M}$ =20 kgcm^{-2}s^{-1}. The vertical lines show reference scales.

6.2.3 Low CNO metallicity and burst properties

The impact of lower CNO metallicity on various burst properties have been investigated in previous studies (Cumming & Bildsten, 2000; Jose et al., 2010). In the present study, CNO metallicity is even lower, compared to previous low metal content cases. Here, we discuss the possible consequences of even lower metallicity in line with the discussion of previous works.

The time to burn hydrogen through hot CNO cycles, before the burst, depends only on CNO metallicity and initial hydrogen abundance. Therefore, time to burn all the hydorgen can be written as (Cumming & Bildsten,2000)

$$t_h \approx 22hr(\frac{0.01}{Z_{CNO}})\frac{X_p}{0.71} \tag{6.11}$$

This equation shows that as the CNO metallicity (Z_{CNO}) decreases, more time is needed to burn the hydrogen. Therefore, only for burst recurrence time less than t_h, all hydrogen will be burnt before the burst is triggered and such cases would lead to pure helium flashes. Smaller values of Z_{CNO} ensures that even for more very long recurrence times there might still be some hydrogen left and leads to mixed flashes.

The other possible impact of extremely lower Z_{CNO} values could be on the heating of accumulated layer.The heating sources for accumulating layer is hydrogen burning through hot CNOs and heat flux from deeper layers. The luminosity from deeper layers can be written as (in ergs s^{-1})(Woosley et al., 2004)

$$L_b \approx 10^{34} \times \frac{Q_b}{0.1MeV} \frac{\dot{M}}{0.1\dot{M}_{Edd}}, \tag{6.12}$$

where Q_b is energy per accreted nucleon (MeV). For one of the cases in the present study with $\dot{M} = 1$ kgcm^{-2}s^{-1} $\approx 0.01\dot{M}_{Edd}$ and assuming $Q_b = 1$ MeV, the $L_b \approx 10^{34}$ ergs s^{-1}. The hot CNO luminosity (in ergs s^{-1}) can be estimated by (Woosley et al., 2004)

$$L_{CNO} = 10^{35} \times \frac{Z_{CNO}}{0.02} \frac{\Delta M_H}{10^{21}}, \tag{6.13}$$

where ΔM_H is the mass of accumulated hydrogen layer (in grams). From the above equation (assuming $\Delta M_H = 10^{21}$g), previous studies showed that either $L_b > L_{CNO}$ (Z_{CNO} solar) or $L_b \approx L_{CNO}$ (lower metallicity case). However, the present study has $Z_{CNO} \approx 10^{-9}$ for $\dot{M} = 1$ kg cm^{-2}s^{-1} case. This value of CNO gives us $L_{CNO} \approx 10^{27}$ ergs s^{-1} i.e $L_{CNO} << L_b$. This tells that heating of the layer, as it accumulates, is dominated by the heat from the deeper layers for a remarkably lower metal content case. Therefore, models of X-ray bursts in such situation could show high sensitivity to the heat source in the deeper layers.

6.3 Summary

We have explored the spallation of accreted material in the atmospheres of a neutron star in X-ray binaries. A full cascading destruction process has been considered for the first time, and the remaining composition of accreted material after spallation has been calculated for two different mass accretion rates. We have shown that all elements above *Be* are destroyed to minuscule values for two different accretion rates considered in this study. Our primary focus was to understand the impact of replenishment of CNO elements due to the destruction of heavier elements in a cascading destruction process. The replenishment effect in a cascading destruction process on the surviving mass fractions has been compared to non-cascading (or isolated) destruction. We demonstrated that the destruction of CNO elements could be overestimated if no replenishment is considered. However, this replenishment is very small and CNO elements are still destroyed to negligible values.

The burst properties are related to CNO metallicity in an intricate manner and should be studied through the multizone calculations with proper ignition conditions. No such attempt has been made in the present study, and we have restricted ourselves to analytical expressions to investigate the impact of Z_{CNO} on X-ray bursts. Using simple analytical expressions, we have shown that if spallation reduces the Z_{CNO} values, it could change the ignition conditions for X-ray bursts.

Here one must be cautious that this whole spallation episode has been discussed only in one particular stopping scenario i.e. incident ions are stopped through collisional deceleration. There are alternative stopping scenarios (for example collision-less shock) and it is necessary to consider those as well.

Bibliography

1. A. Cumming and L. Bildsten, "Carbon Flashes in the Heavy-Element Ocean on Accreting Neutron Stars," *Ap. J.*, vol. 559, pp. L127-L130, 2001.

2. A. Cumming and L. Bildsten, "Rotational Evolution during Type I X-Ray Bursts," *Ap. J.*, vol. 554, pp. 453-474, 2000.

3. A. Ekström, G. R. Jansen, K. A. Wendt, G. Hagen, T. Papenbrock, B. D. Carlsson, C. Forssn, M. Hjorth-Jensen, P. Navrtil, and W. Nazarewicz, "Accurate nuclear radii and binding energies from a chiral interaction," *Phys. Rev. C*, vol. 91, no. 5, p. 051301, 2015.

4. A. Gade, P. Adrich, D. Bazin, M. D. Bowen et al."Spectroscopy of ^{20}Mg: The isobaric mass multiplet equation for the 2^+ states of the $A = 20$, $T = 2$ quintet and distant mirror nuclei," *Phys. Rev. C*, vol 76, no. 2, p. 024317, 2007.

5. A. Heger, A. Cumming, D.K. Galloway and S. E. Woosley,"Models of Type I X-Ray Bursts from GS 1826-24: A Probe of rp-Process Hydrogen Burning", *Ap. J.*, Volume 671, no. 2, pp. L141-L144, 2007.

6. A. Heger, A. Cumming and S. E. Woosley, "Millihertz Quasi-Periodic Oscillations from Marginally Stable Nuclear Burning on an Accreting Neutron Star,", *Ap.J.*, vol. 665, pp. 1311-1320, 2007.

7. A. Matic, A. M. van den Berg, M. N. Harakeh, and H. J. Wörtche, and G. P. A. Berg et al., "High-precision (p,t) reaction measurement to determine ^{18}Ne$(\alpha,p)^{21}$Na reaction rates," *Phys. Rev. C*, vol. 80, no.5, pp. 055804, 2009.

8. A. Simon, A. Spyrou, T. Rauscher et al.,"Systematic study of (p,γ) reactions on Ni isotopes", *Phys. Rev. C*, vol. 87, no. 5, p. 055802, 2013.

9. C. Iliadis (2010) "Nuclear Physics of Stars", *Wiley:VCH*

10. C. J. Horowitz, O. L. Caballero, and D. K. Berry, "Thermal conductivity and phase separation of the crust of accreting neutron stars," *Phys. Rev. E*, vol. 79, no. 2, p. 026103, 2009.

11. C. W. Cook, W. A. Fowler, C. C. Lauritsen, and T. Lauritsen, "B^{12}, C^{12}, and the Red Giants," *Phys. Rev.*, vol. 107. pp. 508-512, 1957.

12. D. Gazit, S. Quaglioni and P. Navrátil,"Three-Nucleon Low-Energy Constants from the Consistency of Interactions and Currents in Chiral Effective Field Theory," *Phys. Rev. Lett.*, vol. 103, no. 10, p. 102502, 2009.

13. E. F. Brown & A. Cumming, "Mapping crustal heating with the cooling lightcurves of quasi-persistent transients," *Ap. J.*, vol. 698, pp. 10201032, 2009.

14. E. Kuulkers, J. J. M. in t Zand, M. H. van Kerkwijk et al., "A half-a-day long thermonuclear X-ray burst from KS 1731260," *A & A*, Vol. 382, no.2, pp. 503-512, 2002.

15. F. Käppeler, R. Gallino, S. Bisterzo, and W. Aoki,"The *s* process: Nuclear physics, stellar models, and observations," *Rev. Mod. Phys.*, vol.83, no. 1, pp. 157-193 , 2011.

16. F. Ozel and P.Freire, "Masses, Radii, and the Equation of State of Neutron Stars," *Annu. Rev. of Astron. and Astroph.,* , vol. 54, pp. 401-440, 2016.

17. G. C. Ball, L. Buchmann, B. Davids, R. Kanungo, C. Ruiz and C E. Svensson, "Physics with reaccelerated radioactive beams at TRIUMF-ISAC," *Journal of Physics G: Nuclear and Particle Physics*, vol. 38, no. 2, pp. 024003, 2011.

18. G. Sheffer, 2013 (private communication).

19. H. Schatz, A. Aprahamian, J. Grres, M. Wiescher, T. Rauscher, J.F. Rembges, F.-K. Thielemann, B. Pfeiffer, P. Mller, K.-L. Kratz, H. Herndl, B.A. Brown and H. Rebel, "rp-process nucleosynthesis at extreme temperature and density conditions," *Physics Reports*, Volume 294, pp. 167-263, Issue 4, 1998.

20. H. Schatz, A. Aprahamian, V. Barnard, L. Bildsten, A. Cumming, M. Ouellette, T.Rauscher, F.-K.Thielemann, and M. Wiescher, "End Point of the *rp* Process on Accreting Neutron Stars", *Phys. Rev. Lett.*, vol. 86, no. 16, pp. 3471-3474, 2001.

21. H. Schatz, K.E. Rehm, "X-ray binaries," *Nuclear Physics A*, Vol. 777, pp. 601-622, 2006.

22. H. Schatz, L. Bildsten and A. Cumming, "The Rapid Proton Process Ashes from Stable Nuclear Burning on an Accreting Neutron Star," *Ap. J.*, Vol. 524, no. 2, pp. 1014-1029, 1999.

23. H. Schatz, L. Bildsten, A. Cumming & M. Ouellette, "Nuclear physics in normal X-ray bursts and superbursts,",*Nuc. Phys. A*, vol. A718, pp. 247c-254c, 2003.

24. I. J. Thompson, "Coupled reaction channels calculations in nuclear physics," *Comput. Phys. Rep.*, vol. 7, no. 4, pp. 167-212, 1988.

25. J. D. Holt, J. Menndez, and A. Schwenk, "Three-Body Forces and Proton-Rich Nuclei," *Phys. Rev. Lett.*, vol. 110, p. 022502, 2013.

26. J. Görres, M. Wiescher and F.-K., Thielemann, "Bridging the waiting points: The role of two-proton capture reactions in the rp process," *Phys. Rev. C*, vol. 51, no. 1, pp. 392-400, 1995.

27. J. Jose, F. Moreno, A. Parikh, and C.Iliadis, "Hydrodynamic Models of type I X-ray bursts: Metallicity effects," *Ap. J.* , vol. 189, pp. 204-239, 2010.

28. J. J. M. in t Zand1, L. Keek2 and Y. Cavecchi, "Relativistic outflow from two thermonuclear shell flashes on neutron stars," *A & A*, vol. 568, p. A69, 2014.

29. J. M. Blatt, V. F. Weisskopf, "Theoretical Nuclear Physics" (New York : Wiley), 1952.

30. J. M. D'Auria, "A review of radioactive beam facilities in the world," *Nuclear Instruments and Methods in Physics Research Section B: Beam Interactions with Materials and Atoms*, vol. 99, no. 1-4, pp. 330-334, 1995.

31. J. Stevens, E. F. Brown, A. Cumming, R. Cyburt and H. Schatz, "Carbon Synthesis in Steady-State Hydrogen and Helium Burning On Accreting Neutron Stars," *Ap. J.*, vol 791, p. 106, 2014.

32. J. R. Letaw, R. Silberberg and C. H. Tsao, "Proton-nucleus total inelastic cross sections - an empirical formula for E greater than 10 MeV,", *Ap. J. (Supp. Series)*, vol. 53, pp. 271-275, 1983.

33. K. Nomoto, F.-K. Thielemann, and S. Miyaji,"The triple alpha reaction at low temperatures in accreting white dwarfs and neutron stars," *A & A*, vol. 149, pp. 239-245, 1985.

34. K.H. Langanke, M. Wiescher, W.A. Fowler, and J.Gorres,"A new estimate of the ^{19}Ne(p, γ) ^{20}Na and ^{15}O(α, γ)^{19}Ne reaction rates at stellar energies," *Ap. J.*, vol. 301, p. 629, 1986.

35. L. Bildsten, E. E. Salpeter, and A. Wasserman, "The fate of accreted CNO elements in neutron star atmospheres: X-ray bursts and gamma-ray lines,",*ApJ.*, vol. 384, pp. 143-176, 1992.

36. L. Bildten, 1997, "Thermonuclear Burning on Rapidly Accreting Neutron Stars", arXiv:astro-ph/9709094 .

37. L. R. Gasques, A. V. Afanasjev, E. F. Aguilera, M. Beard, L. C. Chamon, P. Ring, M. Wiescher, and D. G. Yakovlev, "Nuclear fusion in dense matter: Reaction rate and carbon burning," *Phys. Rev. C*, vol. 72, p. 025806, 2005.

38. M. Arnould and S. Goriely, "The p-process of stellar nucleosynthesis: astrophysics and nuclear physics status," *Physics Reports*, vol. 384, no. 1-2, pp. 1-84, 2003.

39. M. Arnould, S. Goriely, K. Takahashi, "The r-process of stellar nucleosynthesis: Astrophysics and nuclear physics achievements and mysteries," *Physics Reports*, Volume 450, no. 46, pp. 97-213, 2007.

40. M. E. Burbidge, G.R. Burbidge, William A. Fowler and F. Hoyle, " Synthesis of the Elements in Stars," *Reviews of Modern Physics*, vol. 29, pp. 547-650, 1957.

41. M. Wiescher, J. Görres, H. Schatz, "TOPICAL REVIEW: Break-out reactions from the CNO cycles," *Journal of Physics G: Nuclear and Particle Physics*, Vol. 25, no. 6, pp. R133-R161, 1999.

42. M. Wiescher, J. Görres, E. Uberseder, G. Imbriani, and M. Pignatari, "The Cold and Hot CNO Cycles,", *Annual Review of Nuclear and Particle Science* vol. 60, pp. 381-404, 2010.

43. M. Y. Fujimoto,T. Hanaawd, S. Miyaji, "Shell flashes on accreting neutron stars and X-ray bursts", "Ap.J.", vol. 246, pp. 267-278, 1981.

44. M. Zamfir, A. Cumming, and D. K. Galloway,"Constraints on neutron star mass and radius GS 182624 from sub-Eddington X-ray bursts",*ApJ*, vol 746, p.69, 2012.

45. P. Navratil, "Local three-nucleon interaction from chiral effective field theory", *Few-Body Syst.*, vol. 41, pp. 117-140, 2007.

46. P. R. Fortier, "Development of a low-pressure ionization chamber for rare isotope experiments at IRIS,"*M. Sc. Thesis, Saint Mary's University, Halifax, N.S.*, 2013.

47. R. H. Cyburt, A. M. Amthor, A. Heger, E. Johnson, L. Keek, Z. Meisel, H. Schatz and K. Smith,"Dependence of X-ray bursts models on nuclear reaction rates,", *Ap. J.*, vol. 830, no, 2, p. 189, 2016.

48. R. H. Cyburt, B. D. Fields, K. A. Olive, and T.-H.Yeh, "Big bang nucleosynthesis: Present status," *Rev. Mod. Phys.*, vol. 88, no. 1, p. 015004, 2016.

49. R. Kanungo, "IRIS: The ISAC charged particle reaction spectroscopy facility for reaccelerated high-energy ISOL beams", *Hyperfine Interactions*, vol. 225, no. 1, pp 235240 , 2014.

50. R. K. Wallace & S. E. Woosley,"Explosive hydrogen burning," *Ap.J. (Supp. Series.)*, vol. 45, p. 389-420, 1981.

51. R. Machleidt and D. R. Entem, "Chiral effective field theory and nuclear forces," *Physics Reports*, vol. 503, no. 1, pp. 1-75, 2011.

52. R. Silberberg, C. H. Tsao, and A. F. Barghouty, "Updated Partial Cross Sections of Proton-Nucleus Reaction", *Ap. J.*, vol. 501, pp. 911-919, 1998.

53. S. E. Woosley, A. Heger, A. Cumming, R. D. Hoffman, J. Pruet, T. Rauscher, J. L. Fisker, H. Schatz, B. A. Brown, and M. Wiescher, "Models for Type I X-Ray Bursts with Improved Nuclear Physics," *Ap. J.(Supp. Series)*, vol. 151, pp. 75-102, 2004.

54. S. L. Shapiro, E. E. Salpeter, "Accretion onto neutron stars under adiabatic shock conditions," *Ap. J.*, vol. 198,p. 671-682, 1975.

55. S. Weinberg, "Nuclear forces from chiral Lagrangians," *Physics Letters B*, vol. 251, no. 2, pp. 288-292, 1990.

56. S. Weinberg, "Effective chiral Lagrangians for nucleon-pion interactions and nuclear forces," *Nucl. Phys.*, vol. B363, pp. 3-18, 1991.

57. W. A. Fowler, G. R. Caughlan & B. A. Zimmerman,"Thermonuclear Reaction Rates,"*ARA & A*, vol 5, p. 525, 1967.

58. W. H. G. Lewin, J. van Paradijs, and R. E. Taam, "X-Ray Bursts," *Space Sci. Rev.*, vol. 62, no. 2-3 ,pp. 223-389, 1993.